REPORT DOCUMENTATION PAGE

Form Approved
OMB No. 0704-0188

Public reporting burden for this collection of information is estimated to average 1 hour per response, including the time for reviewing instructions, searching data sources, gathering and maintaining the data needed, and completing and reviewing the collection of information. Send comments regarding this burden estimate or any other aspect of this collection of information, including suggestions for reducing this burden to Washington Headquarters Service, Directorate for Information Operations and Reports, 1215 Jefferson Davis Highway, Suite 1204, Arlington, VA 22202-4302, and to the Office of Management and Budget, Paperwork Reduction Project (0704-0188) Washington, DC 20503.
PLEASE DO NOT RETURN YOUR FORM TO THE ABOVE ADDRESS.

1. REPORT DATE *(DD-MM-YYYY)*	2. REPORT TYPE	3. DATES COVERED *(From - To)*
07/17/2012	Annual Progress/Status	05/2011-05/2012

4. TITLE AND SUBTITLE
Strongly Interacting Fermi Gases in Two Dimensions

5a. CONTRACT NUMBER
NA

5b. GRANT NUMBER
N00014-10-1-0843

5c. PROGRAM ELEMENT NUMBER

6. AUTHOR(S)
Zwierlein, Martin W

5d. PROJECT NUMBER

5e. TASK NUMBER

5f. WORK UNIT NUMBER

7. PERFORMING ORGANIZATION NAME(S) AND ADDRESS(ES)
Massachusetts Institute of Technology
77 Massachusetts Avenue
Cambridge, MA 02139

8. PERFORMING ORGANIZATION REPORT NUMBER

9. SPONSORING/MONITORING AGENCY NAME(S) AND ADDRESS(ES)
Office of Naval Research
875 North Randolph Street
Arlington, VA 22203-1995

10. SPONSOR/MONITOR'S ACRONYM(S)
ONR BD025

11. SPONSORING/MONITORING AGENCY REPORT NUMBER

12. DISTRIBUTION AVAILABILITY STATEMENT
Approved for Public Release; distribution is unlimited.

13. SUPPLEMENTARY NOTES

14. ABSTRACT
In this project we aim to directly realize a model system of strongly correlated electrons moving in two dimensions using ultracold fermionic atoms stored in a sheet of light. The goal is to create high-temperature superfluids in two dimensions, to establish interferometry and magnetometry with these systems, and to study the phase diagram of two-dimensional Fermi gases with arbitrary interactions and spin imbalance. Fast rotation will mimic high magnetic fields and allow the approach to the Quantum Hall regime. The system shares traits with High-Tc materials, where super currents flow between stacks of weakly connected two dimensional planes. This year has seen rather spectacular progress: We could study the evolution of fermion pairing from three to two dimensions; determine the equation of state of strongly interacting Fermi gases across the superfluid transition; produce mixtures of sodium and fermionic potassium for the study of impurities in lower dimensions; and create and study spin-orbit coupling in a degenerate Fermi gas.

15. SUBJECT TERMS
Ultracold Atoms, Fermi Gases, Strong Interactions, Lower Dimensions, Strongly Correlated Materials, Quantum Simulators, Superconductivity

16. SECURITY CLASSIFICATION OF:			17. LIMITATION OF ABSTRACT	18. NUMBER OF PAGES	19a. NAME OF RESPONSIBLE PERSON
a. REPORT	b. ABSTRACT	c. THIS PAGE	SAR		19b. TELEPONE NUMBER (*Include area code)*
UU	UU				

Young Investigator Program – Office of Naval Research
Martin W. Zwierlein, MIT

Progress 06/2011-05/2012

Overview

In this project we aim to directly realize a model system of strongly correlated electrons moving in two dimensions using ultracold fermionic atoms stored in a sheet of light. The goal is to create high-temperature superfluids in two dimensions, to establish interferometry and magnetometry with these systems, and to study the phase diagram of two-dimensional Fermi gases with arbitrary interactions and spin imbalance. Fast rotation will mimic high magnetic fields and allow the approach to the Quantum Hall regime. The system shares traits with High-T_c materials, where super currents flow between stacks of weakly connected two dimensional planes. This year has seen rather spectacular progress: We could study the evolution of fermion pairing from three to two dimensions; determine the equation of state of strongly interacting Fermi gases across the superfluid transition; produce mixtures of sodium and fermionic potassium for the study of impurities in lower dimensions; and create and study spin-orbit coupling in a degenerate Fermi gas.

1. Evolution of Fermion Pairing from Three to Two Dimensions

Ariel T. Sommer, Lawrence W. Cheuk, Mark Jen-Hao Ku, Waseem S. Bakr, Martin W. Zwierlein

Phys. Rev. Lett. 108, 045302 (2012)
Highlighted as a Viewpoint in Physics 5, 10 (2012) by Mohit Randeria

Interacting fermions in coupled two-dimensional (2D) layers present unique physical phenomena and are central to the description of unconventional superconductivity in high-transition-temperature cuprates and layered organic conductors. Reduced dimensionality enhances the effect of fluctuations, while interlayer coupling can stabilize superconductivity and even amplify the transition temperature. A fermionic superfluid loaded into a periodic potential should form stacks of two-dimensional superfluids with tunable interlayer coupling, a key ingredient of the model proposed by Anderson to explain high transition temperatures observed in the cuprates. For deep potentials in the regime of uncoupled 2D layers, increasing the temperature of the gas is expected to destroy superfluidity through the Berezinskii-Kosterlitz-Thouless mechanism, while more exotic multi-plane vortex loop excitations are predicted for a 3D-anisotropic BCS superfluid near the critical point.

In this work, we studied fermion pairing across the crossover from 3D to 2D in a periodic potential of increasing depth. We follow the evolution of fermion pairing in the dimensional crossover from 3D to 2D as a strongly interacting Fermi gas of ^{6}Li atoms becomes confined to a stack of two-dimensional layers formed by a one-dimensional optical lattice. Decreasing the dimensionality leads to the opening of a gap in radiofrequency spectra,

even on the BCS-side of a Feshbach resonance. With increasing lattice depth, the measured binding energy E_B of fermion pairs increases in surprising agreement with mean-field theory for the BEC-BCS crossover in two dimensions.

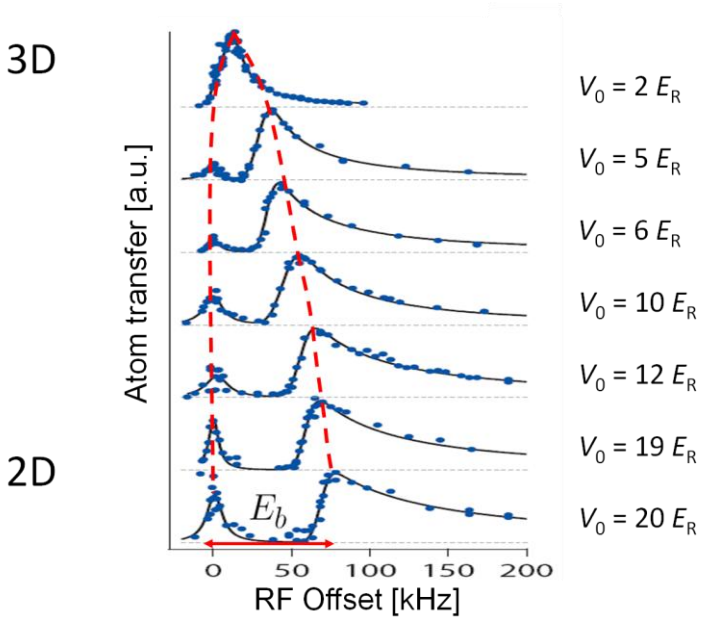

Figure 1 Figure 1 Evolution of Fermion Pairing from Three to Two Dimensions. Radio-Frequency Spectra show the opening of a pairing gap as the Fermi Gas is more and more confined to two dimensions. V0 denotes the strength of the optical lattice used to confine the gas, in units of the recoil energy ER of a 6Li atom in the lattice.

2. Revealing the Superfluid Lambda Transition in the Universal Thermodynamics of a Unitary Fermi Gas

Mark J. H. Ku, Ariel T. Sommer, Lawrence W. Cheuk, Martin W. Zwierlein
Science **335**, 563 (2012)
Highlighted in a Science Perspective by Wilhelm Zwerger

Fermi gases, collections of fermions such as neutrons and electrons, are found throughout nature, from solids to neutron stars. Interacting Fermi gases can form a superfluid or, for charged fermions, a superconductor. We have directly observed the superfluid phase transition in a strongly interacting Fermi gas via high-precision measurements of the local compressibility, density and pressure. Our data completely determine the universal thermodynamics of these gases without any fit or external thermometer. The onset of superfluidity is observed in the compressibility, the chemical potential, the entropy, and the heat capacity, which displays a characteristic lambda-like feature at the critical temperature of 16.7% of the Fermi temperature. Scaled to the density of electrons in a metal, this form of superfluidity would occur far above room temperature. Our measurements provide a benchmark for many-body theories on strongly

interacting fermions, relevant for problems ranging from high-temperature superconductivity to the equation of state of neutron stars.

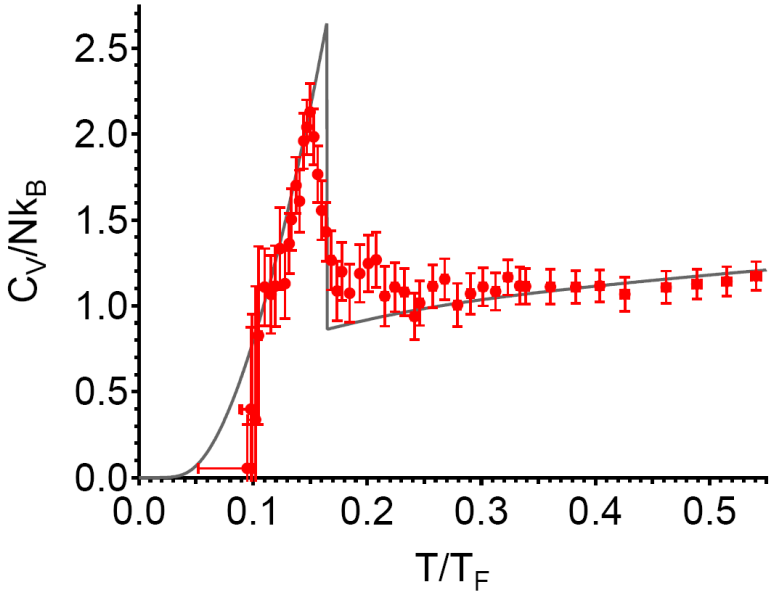

Figure 2 Observation of the Superfluid Lambda Transition in a trongly interacting Fermi Gas. Shown is the specific heat of the gas, directly obtained from the density profiles of a trapped gas.

3. Feynman diagrams versus Feynman quantum emulator

K. Van Houcke, F. Werner, E. Kozik, N. Prokofev, B. Svistunov, M. Ku, A. Sommer, L. W. Cheuk, A. Schirotzek, M. W. Zwierlein

Feynman diagrams versus Fermi-gas Feynman emulator

Nature Physics **8**, 366 (2012)

Precise understanding of strongly interacting fermions, from electrons in modern materials to nuclear matter, presents a major goal in modern physics. However, the theoretical description of interacting Fermi systems is usually plagued by the intricate quantum statistics at play. Here we present a cross-validation between a new theoretical approach, Bold Diagrammatic Monte Carlo (BDMC), and precision experiments on ultra-cold atoms. Specifically, we compute and measure with unprecedented accuracy the normal-state equation of state of the unitary gas, a prototypical example of a strongly correlated fermionic system. Excellent agreement demonstrates that a series of Feynman diagrams can be controllably resummed in a non-perturbative regime using BDMC. This opens the door to the solution of some of the most challenging problems across many areas of physics.

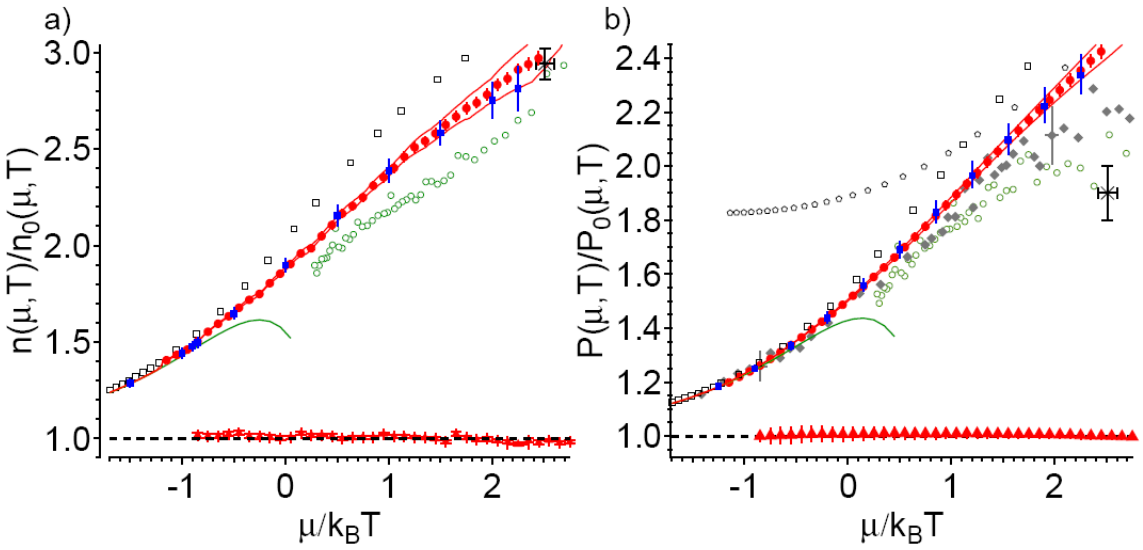

Figure 3 Equation of State of a Unitary Fermi Gas. a) Density and b) pressure as a function of the ratio of the chemical potential to the temperature. Density and pressure are normalized by the respective quantities of a non-interacting Fermi gas at the same ratio μ/k_BT.

4. Quantum degenerate Bose-Fermi mixture of chemically different atomic species with widely tunable interactions

Jee Woo Park, Cheng-Hsun Wu, Ibon Santiago, Tobias G. Tiecke, Peyman Ahmadi, Martin W. Zwierlein

Phys. Rev. A 85, 051602(R) (2012)

We have created a quantum degenerate Bose-Fermi mixture of ^{23}Na and ^{40}K with widely tunable interactions via broad interspecies Feshbach resonances. Twenty Feshbach resonances between ^{23}Na and ^{40}K were identified. The large and negative triplet background scattering length between ^{23}Na and ^{40}K causes a sharp enhancement of the fermion density in the presence of a Bose condensate. As explained via the asymptotic bound-state model (ABM), this strong background scattering leads to a series of wide Feshbach resonances observed at low magnetic fields. Our work opens up the prospect to create chemically stable, fermionic ground state molecules of ^{23}Na-^{40}K where strong, long-range dipolar interactions will set the dominant energy scale.

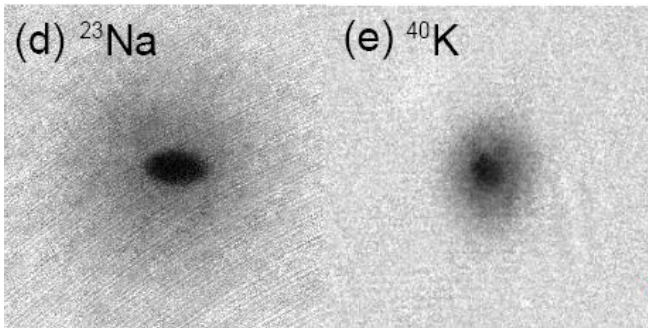

Figure 4 Strongly interacting degenerate Bose-Fermi mixture of ^{23}Na and ^{40}K. The fermion cloud (to the right) displays an untypical “bimodality” due to the strong interactions with the sodium condensate.

5. Spin-Injection Spectroscopy of a Spin-Orbit Coupled Fermi Gas

Lawrence W. Cheuk, Ariel T. Sommer, Zoran Hadzibabic, Tarik Yefsah, Waseem S. Bakr, Martin W. Zwierlein

Phys. Rev. Lett., in print, preprint arXiv: 1205.3483 (2012)

The coupling of the spin of electrons to their motional state lies at the heart of recently discovered topological phases of matter. Here we create and detect spin-orbit coupling in an atomic Fermi gas, a highly controllable form of quantum degenerate matter. We reveal the spin-orbit gap via spin-injection spectroscopy, which characterizes the energy-momentum dispersion and spin composition of the quantum states. For energies within the spin-orbit gap, the system acts as a spin diode. To fully inhibit transport, we open an additional spin gap, thereby creating a spin-orbit coupled lattice whose spinful band structure we probe. In the presence of s-wave interactions, such systems should display induced p-wave pairing, topological superfluidity, and Majorana edge states.

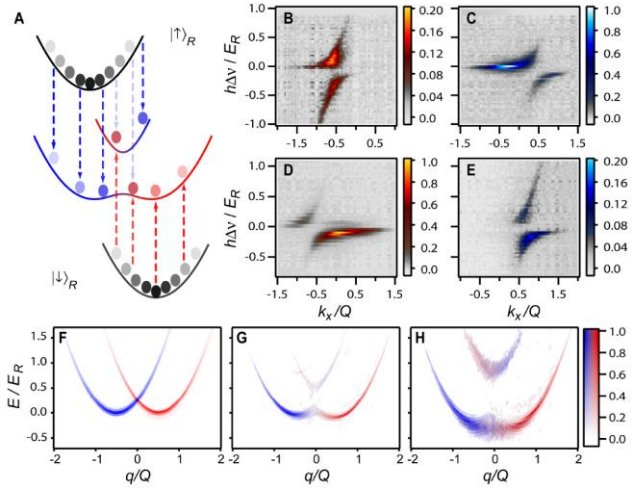

Figure 5 Spin-Injection Spectroscopy of a Spin-Orbit Coupled Fermi Gas. (A) A radiofrequency pulse transfers atoms from the reservoir states $|\uparrow\rangle_R$ and $|\downarrow\rangle_R$ (shown in black) into the spin-orbit coupled system (shown in red and blue). Transfer occurs when the RF photon energy equals the energy difference between the reservoir state and the spin-orbit coupled state at quasi-momentum

q. (B,C,D and E) Transfer as a function of RF frequency and detuning $h\Delta\nu$ and quasi-momentum q. (B and C) Spin-resolved $|\uparrow\rangle$ and $|\downarrow\rangle$ spectra, respectively, when transferring out of $|\uparrow\rangle_R$. (D and E) Spin-resolved $|\uparrow\rangle$ and $|\downarrow\rangle$ spectra, respectively, when transferring out of $|\downarrow\rangle_R$. (F, G and H) The reconstructed spinful dispersions of a spin-orbit coupled Fermi gas for various strengths of Raman coupling.

6. Ultracold Fermionic Feshbach Molecules of $^{23}Na^{40}K$

Cheng-Hsun Wu, Jee Woo Park, Peyman Ahmadi, Sebastian Will, Martin W. Zwierlein.
Phys. Rev. Lett., in print, preprint arXiv:1206.5023 (2012).

We report on the formation of ultracold fermionic Feshbach molecules of $^{23}Na^{40}K$, the first fermionic molecule that is chemically stable in its ground state. The lifetime of the nearly degenerate molecular gas exceeds 100 ms in the vicinity of the Feshbach resonance. The measured dependence of the molecular binding energy on the magnetic field demonstrates the open-channel character of the molecules over a wide field range and implies significant singlet admixture. This will enable efficient transfer into the singlet vibrational ground state, resulting in a stable molecular Fermi gas with strong dipolar interactions.

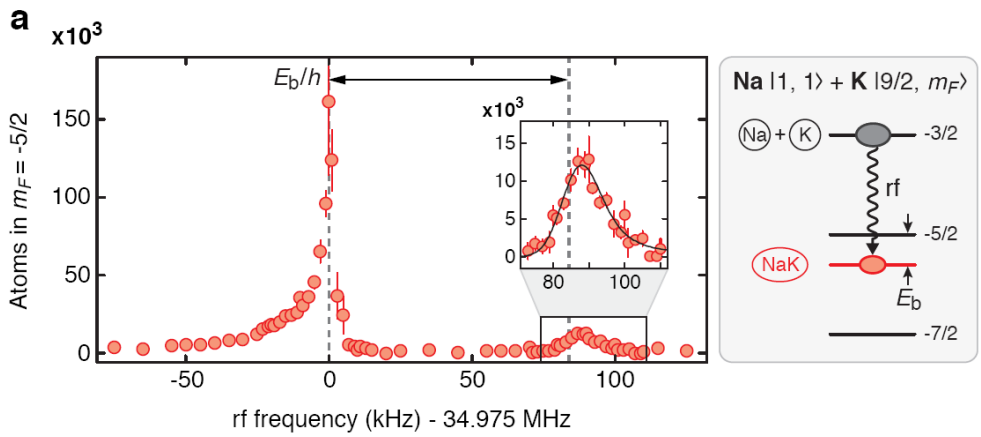

Figure 6 Radiofrequency association of ultracold Feshbach molecules of NaK. Starting with a mixture of sodium atoms in hyperfine state $|1,1\rangle_{Na}$ and potassium atoms in hyperfine state $|9/2,-3/2\rangle_K$, rf spectroscopy near the $|9/2,-3/2\rangle_K$ to $|9/2,-5/2\rangle_K$ hyperfine transition reveals free ^{40}K atoms repulsively interacting with the ^{23}Na bath (near zero rf offset), as well as associated molecules (near 85 kHz rf offset). A fit to the molecular association spectrum yields a binding energy of $E_b = h$ x 84(6) kHz. The magnetic field corresponding to the atomic transition at 34.975 MHz was 129.4 G.

Publications

Journal Articles

1. Ariel T. Sommer, Lawrence W. Cheuk, Mark Jen-Hao Ku, Waseem S. Bakr, Martin W. Zwierlein.
   Evolution of Fermion Pairing from Three to Two Dimensions.
   Phys. Rev. Lett. **108**, 045302 (2012)

2. Mark J. H. Ku, Ariel T. Sommer, Lawrence W. Cheuk, Martin W. Zwierlein.
   Revealing the Superfluid Lambda Transition in the Universal Thermodynamics of a Unitary Fermi Gas.
   Science **335**, 563 (2012)
   Highlighted in a Science Perspective by Wilhelm Zwerger

3. K. Van Houcke, F. Werner, E. Kozik, N. Prokofev, B. Svistunov, M. Ku, A. Sommer, L. W. Cheuk, A. Schirotzek, M. W. Zwierlein.
   Feynman diagrams versus Fermi-gas Feynman emulator.
   Nature Physics **8**, 366 (2012)

4. Jee Woo Park, Cheng-Hsun Wu, Ibon Santiago, Tobias G. Tiecke, Peyman Ahmadi, Martin W. Zwierlein.
   Quantum degenerate Bose-Fermi mixture of chemically different atomic species with widely tunable interactions.
   Phys. Rev. A **85**, 051602(R) (2012)

5. Lawrence W. Cheuk, Ariel T. Sommer, Zoran Hadzibabic, Tarik Yefsah, Waseem S. Bakr, Martin W. Zwierlein.
   Spin-Injection Spectroscopy of a Spin-Orbit Coupled Fermi Gas.
   Phys. Rev. Lett., in print, preprint arXiv: 1205.3483 (2012)

6. Cheng-Hsun Wu, Jee Woo Park, Peyman Ahmadi, Sebastian Will, Martin W. Zwierlein.
   Ultracold Fermionic Feshbach Molecules of $^{23}Na^{40}K$.
   Phys. Rev. Lett., in print, preprint arXiv:1206.5023 (2012).

Book chapters

7. M. Randeria, W. Zwerger, and M. Zwierlein.
   The BEC-BCS Crossover and the Unitary Fermi Gas.
   Lecture Notes in Physics, Volume 836, edited by Wilhelm Zwerger, Springer, Berlin 2012

Invited Talks at Conferences

1. *Universal Thermodynamics across the Superfluid Transition in a Strongly Interacting Fermi Gas.*
   Workshop on Frontiers in Ultracold Fermi Gases, Trieste, Italy, 6/8/2011
2. *Universal Thermodynamics and Spin Transport in Strongly Interacting Fermi Gases.*
   Multiflavour strongly correlated quantum gases, Hamburg, Germany, 6/24/2011
3. *Universal Thermodynamics and Spin Transport in Strongly Interacting Fermi Gases.*
   International Conference on Quantum Technologies, Moscow, Russia, 7/14/2011
4. *Universal Thermodynamics and Spin Transport in Strongly Interacting Fermi Gases.*
   Non-standard superfluids and insulators, Trieste, Italy, 7/20/2011
5. *Universal Thermodynamics and Spin Transport in Strongly Interacting Fermi Gases.*
   Quantum phenomena in graphene, other low-dimensional materials, and optical lattices, Erice, Italy, 8/4/2011
6. *Universal Thermodynamics and Spin Transport in Strongly Interacting Fermi Gases.*
   Strongly Correlated Electron Systems (SCES 2011), Cambridge, UK, 9/2/2011
7. *Universal Thermodynamics and Spin Transport in Strongly Interacting Fermi Gases.*
   Frontiers in Quantum Gases (BEC2011). San Feliu, Spain, 9/13/2011
8. *Universal Thermodynamics and Spin Transport in Strongly Interacting Fermi Gases.*
   Cecam/Pauli-Center workshop "Modeling Materials With Cold Gases Through Simulations", Zurich, Switzerland, 11/10/2011
9. *Strongly Interacting Fermi Gases: Thermodynamics, Spin Transport, Dimensional Crossover.*
   NewSpin 2 workshop "Winter school and workshop on spin physics and topological effects in cold atoms, condensed matter, and beyond", College Station, TX, 12/16/2011
10. *Strongly Interacting Fermi Gases: Thermodynamics, Spin Transport, Dimensional Crossover.*
    Aspen Winter Conference 2012 "New Directions in Ultracold Atoms", Aspen, CO, 1/9/2012
11. *Fermions in Flatland and Ultracold Fermionic Feshbach Molecules of* $^{23}Na^{40}K$.

ITAMP workshop: Research Frontiers in Ultracold Atoms and Molecules, Cambridge, MA, 4/24/2012

12. *Universal Thermodynamics Across the Superfluid Transition in a Strongly Interacting Fermi Gas.*
    The Extreme Matter Physics of Nuclei: From Universal Properties to Neutron-Rich Extremes, Darmstadt, Germany, 4/30/2012
13. *Spin Transport in Strongly Interacting Fermi Gases & Evolution of Fermion Pairing from 3D to 2D.*
    Low-dimensional quantum gases out of Equilibrium, Minneapolis, MN, 5/11/2012
14. *Strongly Interacting Fermi Gases: Thermodynamics, Lower Dimensions and Novel Phases.*
    International Conference on Frontiers of Cold Atoms and Related Topics, Hong Kong, China, 5/16/2012
15. *Evolution of Fermion Pairing from Three to Two Dimensions.*
    DAMOP 2012, Anaheim, CA, 6/6/2012
16. *Strongly Interacting Fermi Gases: Thermodynamics, Spin Transport and Lower Dimensions.*
    Nonequilibrium phenomena in ultracold atoms and strongly interacting photons, Princeton, NJ, 6/11/2012
17. *Strongly Interacting Fermi Gases: Thermodynamics, Spin Transport, Dimensional Crossover*.
    ICAP 2012, Paris, France, 07/23/2012

Invited Talks at Colloquia and Seminars

1. *A Little Big Bang: Ultracold Fermi Gases at the Quantum Limit.*
   Physics Colloquium, Colby College, Colby College, ME, 10/27/2011
2. *A Little Big Bang: Ultracold Fermi Gases at the Quantum Limit.*
   Physics Colloquium, University of Massachusetts, Boston, Boston, MA, 10/29/2011
3. *A Little Big Bang: Ultracold Fermi Gases at the Quantum Limit.*
   Physics Colloquium, Boston College, Boston, MA, 11/2/2011
4. *A Little Big Bang: Ultracold Fermi Gases with Strong Interactions.*
   Physics Colloquium, Yale University, New Haven, CT, 12/5/2011
5. *A Little Big Bang: Strong Interactions in Ultracold Fermi Gases.*
   Physics Colloquium, Georgetown University, Washington, D.C., 3/20/2012
6. *A Little Big Bang: Strong Interactions in Ultracold Fermi Gases.*
   Physics Colloquium, JILA and University of Colorado, Boulder, CO, 4/11/2012
7. *A Little Big Bang: Strong Interactions in Ultracold Fermi Gases.*
   Los Alamos National Laboratory Physics Colloquium, Los Alamos, NM, 7/9/2012

Contributed Talks by Group Members at Conferences

1. H4.00002: Revealing the superfluid phase transition in strongly interacting Fermi gases in a precision measurement of the equation of state.
   DAMOP 2011, Atlanta, Georgia, 6/15/2011
2. N5.00001 : Universal Spin Transport in Strongly Interacting Fermi Gases.
   DAMOP 2011, Atlanta, Georgia, 6/16/2011
3. P1.00007: Many body effects in a widely tunable Bose-Fermi mixture.
   DAMOP 2011, Atlanta, Georgia, 6/16/2011
4. P1.00003: Triply degenerate quantum mixture of 41K, 40K and 6Li.
   DAMOP 2011, Atlanta, Georgia, 6/16/2011
5. Universal Thermodynamics across the Superfluid Transition in a Strongly Interacting Fermi Gas.
   19th Particles & Nuclei International Conference (PANIC 2011), Cambridge, MA, 7/24/2011
6. Universal Spin Transport in a Strongly Interacting Fermi Gas.
   19th Particles & Nuclei International Conference (PANIC 2011), Cambridge, MA, 7/24/2011
7. B1.00004 : Quantum *degenerate Bose-Fermi mixture of chemically different atomic species with widely tunable interactions.*
   Presented by: J. W. Park, Authors: Jee Woo Park, Cheng-Hsun Wu, Ibon Santiago, Tobias Tiecke, Peyman Ahmadi, Martin Zwierlein
   March Meeting 2012, Boston, MA, 2/27/2012
8. *L4.00010 : Feynman diagrams versus Feynman quantum emulator.*
   Presented by: K. Van Houcke, Authors: Kris Van Houcke, Felix Werner, Evgeny Kozik, Nikolay Prokof'ev, Boris Svistunov, Mark Ku, Ariel Sommer, Lawrence Cheuk, Andre Schirotzek, Martin Zwierlein
   March Meeting 2012, Boston, MA, 2/28/2012
9. *W4.00001 : Revealing the Superfluid Lambda Transition in the Universal Thermodynamics of a Unitary Fermi Gas.*
   Presented by: M. Ku, Authors: Mark Ku, Ariel Sommer, Lawrence Cheuk, Martin Zwierlein
   March Meeting 2012, Boston, MA, 3/1/2012
10. *Y4.00002 : Fermion Pairing in a One-Dimension Optical Lattice.*
    Presented by: A. Sommer, Authors: Ariel Sommer, Lawrence Cheuk, Mark Ku, Waseem Bakr, Martin Zwierlein
    March Meeting 2012, Boston, MA, 3/2/2012
11. *G5.00003 : Quantum degenerate Bose-Fermi mixture of chemically different atomic species with widely tunable interactions.*
    Presented by: J. W. Park, Authors: Jee Woo Park, Cheng-Hsun Wu, Peyman Ahmadi, Sebastian Will, Martin Zwierlein
    DAMOP 2012, Anaheim, CA, 6/6/2012

12. *H2.00004 : Ultracold Feshbach Moleules of NaK.*
    Presented by: C.-H. Wu, Authors: Cheng-Hsun Wu, Jee Woo Park, Peyman Ahmadi, Sebastian Will, Martin Zwierlein
    DAMOP 2012, Anaheim, CA, 6/6/2012
13. *G2.00008 : Raman coupling in a Fermi gas of ^{6}Li atoms.*
    Presented by: L. Cheuk, Authors: Lawrence Cheuk, Mark Ku, Ariel Sommer, Tarik Yefsah, Waseem Bakr, Martin Zwierlein
    DAMOP 2012, Anaheim, CA, 6/6/2012
14. *N2.00009 : Strongly interacting fermions in a 1D optical lattice.*
    Presented by: A. Sommer, Authors: Ariel Sommer, Lawrence Cheuk, Mark Ku, Tarik Yefsah, Waseem Bakr, Martin Zwierlein
    DAMOP 2012, Anaheim, CA, 6/6/2012
15. *M2.00002 : Revealing the Superfluid Lambda Transition in the Universal Thermodynamics of a Unitary Fermi Gas.*
    Presented by: M. Ku, Authors: Mark Ku, Ariel Sommer, Lawrence Cheuk, Tarik Yefsah, Waseem Bakr, Martin Zwierlein
    DAMOP 2012, Anaheim, CA, 6/6/2012

Honors and Awards

Martin Zwierlein:

- Promotion to Associate Professor with Tenure, 07/01/2012
- Silverman Family Career Development Chair, 2011 – current

A. Sommer received the Martin Deutsch Prize for Excellence in Experimental Physics from the MIT Physics Department

Vinay Ramasesh wins Malcolm Cotton Brown Award from MIT physics (06/2012)

Mark Ku wins Harvey Fellowship (03/2012) and DARPA OLE best paper award (12/2011)

arXiv:1205.3483v1 [cond-mat.quant-gas] 15 May 2012

Spin-Injection Spectroscopy of a Spin-Orbit Coupled Fermi Gas

Lawrence W. Cheuk,[1] Ariel T. Sommer,[1] Zoran Hadzibabic,[1,2]
Tarik Yefsah,[1] Waseem S. Bakr,[1] and Martin W. Zwierlein[1]

[1] *Department of Physics, MIT-Harvard Center for Ultracold Atoms, and Research Laboratory of Electronics, MIT, Cambridge, Massachusetts 02139, USA*
[2] *Cavendish Laboratory, University of Cambridge, J. J. Thomson Avenue, Cambridge CB3 0HE, United Kingdom*

The coupling of the spin of electrons to their motional state lies at the heart of recently discovered topological phases of matter [1–3]. Here we create and detect spin-orbit coupling in an atomic Fermi gas, a highly controllable form of quantum degenerate matter [4, 5]. We reveal the spin-orbit gap [6] via spin-injection spectroscopy, which characterizes the energy-momentum dispersion and spin composition of the quantum states. For energies within the spin-orbit gap, the system acts as a spin diode. To fully inhibit transport, we open an additional spin gap, thereby creating a spin-orbit coupled lattice [7] whose spinful band structure we probe. In the presence of s-wave interactions, such systems should display induced p-wave pairing [8], topological superfluidity [9], and Majorana edge states [10].

Spin-orbit coupling is responsible for a variety of phenomena, from the fine structure of atomic spectra to the spin Hall effect, topological edge states, and the predicted phenomenon of topological superconductivity [3, 11]. In electronic systems, spin-orbit coupling arises from the relativistic transformation of electric fields into magnetic fields in a moving reference frame. In the reference frame of an electron moving with wavevector $\mathbf{k}$ in an electric field, the motional magnetic field couples to the electron spin through the magnetic dipole interaction. This spin-orbit coupling phenomenon is responsible for lifting the degeneracy of spin states in the excited orbitals of atoms and solid-state materials such as zinc-blende structures [12]. In a two-dimensional semiconductor heterostructure, the electric field can arise from structure or bulk inversion asymmetry [13], leading to magnetic fields of the form $\mathbf{B}^{(R)} = \alpha(-k_y, k_x, 0)$ or $\mathbf{B}^{(D)} = \beta(k_y, k_x, 0)$. The resulting spin-orbit coupling terms in the Hamiltonian are known as the Rashba [14] and Dresselhaus [12] contributions, respectively. Including a possible momentum-independent Zeeman field $\mathbf{B}^{(Z)} = (0, B_y^{(Z)}, B_z^{(Z)})$, the Hamiltonian of the electron takes the form:

$$\mathcal{H} = \frac{\hbar^2 k^2}{2m} - \frac{g\mu_B}{\hbar}\mathbf{S}\cdot(\mathbf{B}^{(D)} + \mathbf{B}^{(R)} + \mathbf{B}^{(Z)}), \qquad (1)$$

where g is the electron g-factor, μ_B is the Bohr magneton and $\mathbf{S}$ is the electron spin.

The energy-momentum dispersion and the associated spin texture of the Hamiltonian in Eq. (1) are shown in Figure 1A for $B_y^{(Z)} = 0$ and $\alpha = \beta$. In the absence of a perpendicular Zeeman field $B_z^{(Z)}$, the spectrum consists of free particle parabolas for the two spin states that are shifted relative to each other in k-space owing to the spin-orbit interaction. For a finite field $B_z^{(Z)}$, a gap opens in the spectrum. This gap, known as the spin-orbit gap, has been recently observed in one-dimensional quantum wires [6, 15]. The two energy bands are spinful in the sense that the spin of an atom is locked to its momentum. Similar band structures have been used to explain the anomalous quantum Hall effect and predict a saturation of the Hall conductivity for Fermi energies in the gap region [16].

In this work, we engineer the Hamiltonian in Eq. (1) with equal Rashba and Dresselhaus strengths in an optically trapped, degenerate gas of fermionic lithium atoms via Raman dressing of atomic hyperfine states [17, 18]. Raman fields have previously been used to generate spin-orbit coupling and gauge fields in pioneering work on Bose-Einstein condensates [19–21], and recently spin-orbit coupling in Fermi gases [22]. Here, we directly measure the spin-orbit band structure of Eq. (1), as well as the rich band structure of a spin-orbit coupled lattice. For this, we introduce spin-injection spectroscopy, which is capable of completely characterizing the quantum states of spin-orbit coupled fermions, including the energy-momentum dispersion and the associated spin-texture. By tracing the evolution of quantum states in the Brillouin zone, this method is able to directly measure topological invariants, such as the Chern number in a two-dimensional system [3, 11, 23].

In order to directly reveal the single-particle eigenstates of the spin-orbit coupled system, we reduce the interactions in our Fermi gas to a negligible strength. This is convenient for studying topological insulators, whose behavior is mostly governed by single-particle physics. On the other hand, a single-component spin-orbit coupled Fermi gas is expected to develop effective p-wave interactions mediated by s-wave interactions [8], either in the presence of an s-wave Feshbach resonance, or in the presence of flat bands as realized below. This can lead to BCS pairing in a p-wave channel, and in a two-dimensional system with pure Rashba coupling, to $p_x + ip_y$ pairing and chiral superfluidity [8, 9].

We generate spin-orbit coupling using a pair of laser beams that connect two atomic hyperfine levels, labeled $|\uparrow\rangle$ and $|\downarrow\rangle$, via a two-photon Raman transition (Fig. 1B,C). The Raman process imparts momentum

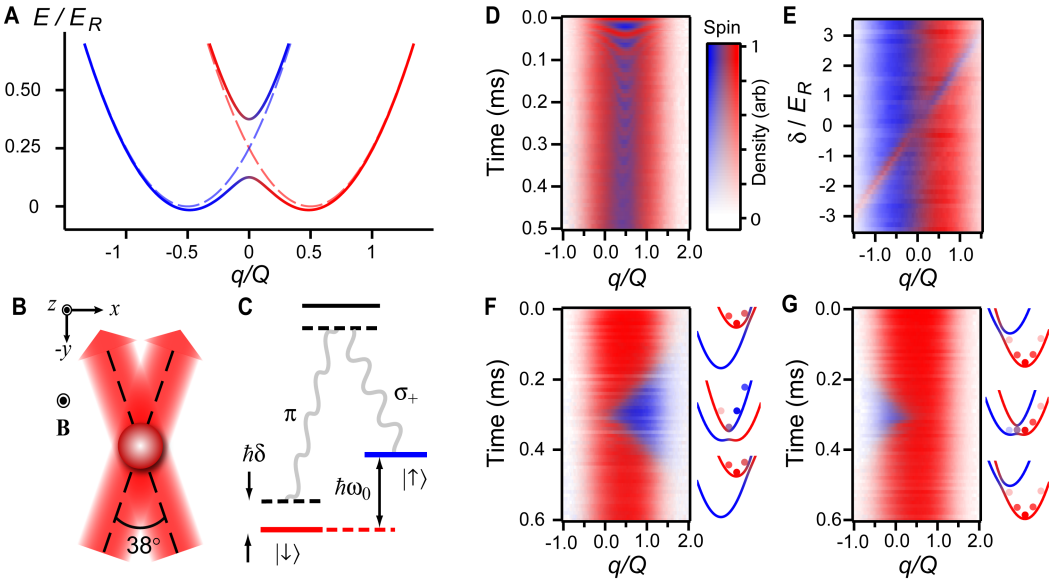

FIG. 1. Realization of spin-orbit coupling in an atomic Fermi gas. (A) Energy bands as a function of quasi-momentum q for Raman coupling strength of $\hbar\Omega_R = 0.25E_R$ and $\hbar\delta = 0$. The spin composition of the states is indicated by the color. Dashed lines show energy bands for $\hbar\Omega_R = 0E_R$ and $\hbar\delta = 0E_R$. (B) Geometry of the Raman beams: A pair of Raman beams at $\pm 19^\circ$ relative to the $\hat{y}$ axis couples states $|\downarrow, k_x = q\rangle$ and $|\uparrow, k_x = q + Q\rangle$. A bias magnetic field $\mathbf{B}$ in the $\hat{z}$ direction provides the quantization axis. (C) The hyperfine interaction splits $|\uparrow\rangle$ and $|\downarrow\rangle$ by $\hbar\omega_0$, and the relevant polarization components are π and σ_+. $\hbar\delta$ is the two-photon detuning. (D) Momentum-dependent Rabi oscillations in the spin texture after sudden switch-on of the Raman beams. Here $\hbar\Omega_R = 0.78(2)E_R$ and the detuning $\hbar\delta = -0.25(1)E_R$. (E) A π-pulse for the resonant momentum-class of atoms is applied at different two-photon detunings $\hbar\delta$. The Raman strength is $\hbar\Omega_R = 0.035(5)E_R$ in order to retain momentum selectivity. (F and G): Adiabatic loading and unloading of atoms into the upper (lower) band at coupling strength of $\hbar\Omega_R = 0.53(5)E_R$. The Raman beams are turned on with $\delta = \mp 8.5\Omega_R$, and the detuning is swept linearly to $\delta = 0$ and back at a rate of $|\dot{\delta}| = 0.27(5)\Omega_R^2$. This loads atoms into the upper (lower) band, as indicated by the diagrams on the right. The spin texture follows the instantaneous value of δ, indicating adiabaticity.

$\hbar Q\hat{x}$ to an atom while changing its spin from $|\downarrow\rangle$ to $|\uparrow\rangle$, and momentum $-\hbar Q\hat{x}$ while changing the spin from $|\uparrow\rangle$ to $|\downarrow\rangle$. Defining a quasimomentum $q = k_x - \frac{Q}{2}$ for spin $|\downarrow\rangle$ and $q = k_x + \frac{Q}{2}$ for spin $|\uparrow\rangle$, one obtains the Hamiltonian of the form given in Eq. (1) [19]. In this mapping, $B_z^{(Z)} = \hbar\Omega_R/g\mu_B$, where Ω_R is the two-photon Rabi frequency, $B_y^{(Z)} = \hbar\delta/g\mu_B$, where δ is the two-photon detuning, and $\alpha = \beta = \frac{\hbar^2 Q}{2mg\mu_B}$ (see Supplemental Material).

When the spin-orbit gap is opened suddenly, an atom prepared in the state $|\downarrow, k_x = q - Q/2\rangle$ oscillates between $|\downarrow, k_x = q - Q/2\rangle$ and $|\uparrow, k_x = q + Q/2\rangle$ with a momentum dependent frequency $\Delta(q)/h$, where $\Delta(q)$ is the energy difference between the bands at quasimomentum q. Such Rabi oscillations correspond to Larmor precession of the pseudo-spin in the effective magnetic field $\mathbf{B}^{(\mathrm{SO})} = \mathbf{B}^{(\mathrm{D})} + \mathbf{B}^{(\mathrm{R})} + \mathbf{B}^{(Z)}$. We have observed these oscillations by starting with atoms in $|\downarrow\rangle$, pulsing on the Raman field for a variable duration τ, and imaging the atoms spin-selectively after time-of-flight expansion from the trap. Time-of-flight maps momentum to real space, allowing direct momentum resolution of the spin populations. As a function of pulse duration, we observe oscillations of the pseudospin polarization with momentum-dependent frequencies (Fig. 1D). Our Fermi gas occupies a large range of momentum states with near-unity occupation. Therefore, each image at a given pulse duration τ contains information for a large range of momenta q. The observation of momentum-dependent oscillations demonstrates the presence of a spin-orbit gap, and shows that the atomic system is coherent over many cycles. To highlight the momentum selectivity of this process, we prepare an equal mixture of atoms in states $|\uparrow\rangle$ and $|\downarrow\rangle$ and pulse on the Raman fields for a time $t = \pi/\Omega_R$ for different two-photon detunings δ. This inverts the spin for atoms with momentum q where $\Delta(q)$ is minimal. Since the minimum of $\Delta(q)$ varies linearly with δ due to the Doppler shift $\propto k_x Q$, the momentum q at which the spin is inverted depends linearly on δ (Fig. 1E).

Instead of pulsing on the Raman field and projecting the initial state into a superposition of states in the two bands, one can introduce the spin-orbit gap adiabatically with respect to band populations. This is achieved by starting with a spin-polarized Fermi gas and sweeping the two-photon detuning δ from an initial value δ_i to a final detuning δ_f. The magnitude of the initial detuning $|\delta_i|$ is much larger than the two-photon recoil energy $E_R = \hbar^2 Q^2/2m$, so that the effective Zeeman field is almost entirely parallel with the spins. Depending on the

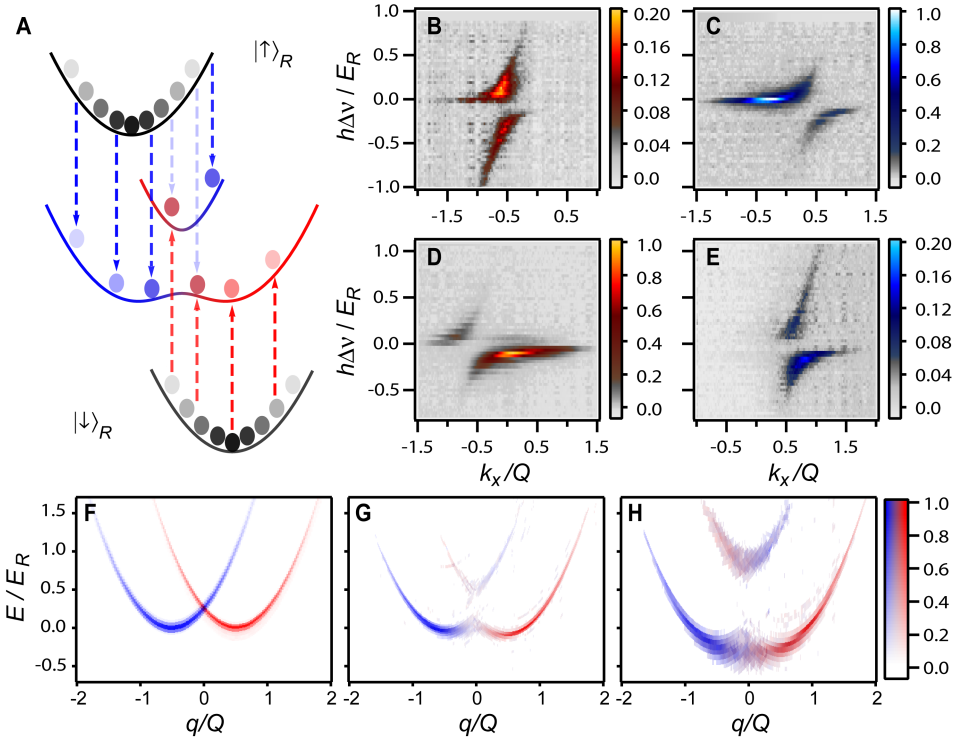

FIG. 2. Spin–injection spectroscopy of a spin-orbit coupled Fermi gas. (A) A radiofrequency (RF) pulse transfers atoms from the reservoir states (shown in black) $|\uparrow\rangle_R$ and $|\downarrow\rangle_R$ into the spin-orbit coupled system (shown in red and blue). Transfer occurs when the RF photon energy equals the energy difference between the reservoir state and the spin-orbit coupled state at quasi-momentum q. (B,C,D and E) Transfer as a function of RF frequency detuning $h\Delta\nu$ and quasi momentum q at Raman coupling strength of $\hbar\Omega_R = 0.43(5)E_R$ and $\hbar\delta = 0.00(3)E_R$. Note that starting with reservoir $|\downarrow\rangle_R$ ($|\uparrow\rangle_R$), transfer to state $|\uparrow\rangle$ ($|\downarrow\rangle$) is entirely due to spin-orbit coupling. Hence the signal is generally much weaker than that for state $|\downarrow\rangle$ ($|\uparrow\rangle$) except right in the gap, where their ratio approaches 50%/50%. (B and C) Spin-resolved $|\downarrow\rangle$ and $|\uparrow\rangle$ spectra, respectively, when transferring out of $|\uparrow\rangle_R$. (D and E) Spin-resolved $|\downarrow\rangle$ and $|\uparrow\rangle$ spectra, respectively, when transferring out of $|\downarrow\rangle_R$. (F,G and H) The reconstructed spinful dispersions for $\hbar\delta = 0.00(3)E_R$ and $\hbar\Omega_R = 0E_R$, $\hbar\Omega_R = 0.43(5)E_R$ and $\hbar\Omega_R = 0.9(1)E_R$, respectively.

direction of the sweep, this loads atoms into either the upper or the lower dressed band. We interrupt the sweep at various times, and image the spin-momentum distribution. This reveals that the spin texture follows the effective Zeeman field. The process is reversible, as we verify by sweeping the detuning back to δ_i and restoring full spin-polarization. (Fig. 1F and G).

Having demonstrated the ability to engineer spin-orbit coupling in a Fermi gas, we introduce a general approach to measure the complete eigenstates and energies of fermions at each quasi-momentum q and thus resolve the band structure and associated spin texture of spin-orbit coupled atomic systems. Our approach yields equivalent information to spin and angle-resolved photoemission spectroscopy (spin-ARPES), a powerful technique recently developed in condensed matter physics [24]. Spin-ARPES is particularly useful for studying magnetic and quantum spin Hall materials; it has been used, for example, to directly measure topological quantum numbers in the $Bi_{1-x}Sb_x$ series, revealing the presence of topological order and chiral properties [25].

Our spectroscopic technique uses radiofrequency (RF) spin-injection of atoms from a free Fermi gas into an empty spin-orbit coupled system using photons of a known energy (Fig. 2A). After injection, the momentum and spin of the injected atoms are analyzed using time of flight [26] combined with spin-resolved detection. Atoms are initially loaded into one of two free "reservoir" atomic states $|\downarrow\rangle_R$ and $|\uparrow\rangle_R$ which can be coupled to the states $|\downarrow\rangle$ and $|\uparrow\rangle$, respectively, via the RF spin-injection field, without changing the quasimomentum. The injection occurs when the frequency of the RF pulse matches the energy difference between the spin-orbit coupled bands and the initial reservoir state (see Fig. 2A). Spin-injection from $|\downarrow\rangle_R$ ($|\uparrow\rangle_R$) populates mostly the region of the spin-orbit coupled bands with a strong admixture of $|\downarrow\rangle$ ($|\uparrow\rangle$) states. Thus, the use of two reservoir states allows us to measure both the $|\downarrow\rangle$-rich and the $|\uparrow\rangle$-rich parts of the spin-orbit coupled bands. Following the injection process, the Raman beams are switched off, and the atoms are simultaneously released from the trap. After a sufficiently long time of free expansion, the density distribution gives access to the momentum distribution, which we measure using state-selective absorption imaging. By counting

the number of atoms of a given spin and momentum as a function of injection energy, we determine the dispersion of the spin-orbit coupled bands along with their spin texture.

The topological characteristics of the bands, which are encoded in the eigenstates, can be extracted from the spin and momentum composition. For our spin-orbit system with $\delta = 0$, the spin of the eigenstates is confined to the y-z plane on the Bloch sphere because the effective magnetic field has no $\hat{x}$ component. More general couplings may not restrict the spin to a great circle on the Bloch sphere, in which case at least two spin components must be measured for a complete characterization of the bands. This can be achieved by rotating the different spin components onto the measurement basis with an RF pulse.

Applying spin-injection spectroscopy, we have measured the band structure of the equal-part Rashba-Dresselhaus Hamiltonian at $\delta = 0$ for several Ω_R. Figure 2B, C, D and E show spin- and momentum- resolved spin-injection spectra obtained with atoms starting in the $|\uparrow\rangle_R$ reservoir (top row) and starting in the $|\downarrow\rangle_R$ reservoir (bottom row), for the case $\hbar\Omega_R = 0.43(5)E_R$ and $\delta = 0$. The $(q,\uparrow) \leftrightarrow (-q,\downarrow)$ symmetry of the system can be seen in the spectra in Fig. 2. The energy at each quasimomentum is found by adding the energy injected into the system by the RF pulse to the initial kinetic energy of the free particle in the reservoir. Figure 2F, G and H show the dispersion and spin texture of the bands obtained from the data. As Ω_R is increased, we observe the opening of a spin-orbit gap at $q = 0$. The spin composition of the bands evolves from purely $|\uparrow\rangle$ or $|\downarrow\rangle$ away from the spin-orbit gap to a mixture of the two spin states in the vicinity of the spin-orbit gap, where the spin states are resonantly coupled.

The dispersion investigated above is the simplest possible for a spin-orbit coupled system and arises naturally in some condensed matter systems. A Fermi gas with this dispersion has an interesting spinful semi-metallic behavior when the Fermi energy lies within the spin-orbit gap. When the Fermi energy is outside the spin-orbit gap, there is a four-fold degeneracy of states at the Fermi surface. Inside the gap, however, the degeneracy is halved. Furthermore, propagation of spin up particles at the Fermi energy can only occur in the positive q direction, while spin down fermions can only propagate in the opposite way. Particles are thus protected from back-scattering in the absence of magnetic impurities that would rotate their spin. Such a spinful semimetal can be used to build spin-current diodes, since the material permits flow of polarized spin-currents in one direction only.

An even richer band structure involving multiple spinful bands separated by fully insulating gaps can arise in the presence of a periodic lattice potential. This has been realized for Bose-Einstein condensates by adding RF coupling between the Raman-coupled states $|\uparrow\rangle$ and $|\downarrow\rangle$ [7]. Using a similar method, we create a spinful lattice for ultracold fermions, and use spin-injection spectroscopy to probe the resulting spinful band structure. The combined Raman/RF coupling scheme is shown in Fig. 3A. The Raman field couples the states $|\downarrow, k_x = q\rangle$ and $|\uparrow, k_x = q + Q\rangle$ with strength Ω_R, whereas the RF field couples the states $|\downarrow, k_x = q\rangle$ and $|\uparrow, k_x = q\rangle$ with strength Ω_{RF}. As a result, the set of coupled states for a given quasimomentum q, shown in the repeated Brillouin scheme in Fig. 3B, is $|\sigma, k_x = q + nQ\rangle$ for integer n and $\sigma = \uparrow, \downarrow$. The lowest four bands are degenerate at the band center $q = 0$ when $\Omega_R = \Omega_{RF} = 0$. The Raman field splits the degeneracy between the first and fourth band, leaving the other two degenerate. The remaining degeneracy, which is a Dirac point, is removed with the addition of the RF field. Thus, when the system is filled up to the top of the second band, it is an insulator. Furthermore, when Ω_{RF} is large enough, a band gap also opens between the first and second bands.

Fig. 3D and E show the spin-injection spectra, measured with fermions initially in reservoir state $|\downarrow\rangle_R$, which is sufficient to reconstruct the full band structure given the $(q,\uparrow) \leftrightarrow (-q,\downarrow)$ symmetry of the Hamiltonian. The transitions between the reservoir and the spin-orbit coupled bands for $\hbar\Omega_R = 0.40(5)E_R$ and $\hbar\Omega_{RF} = 0.28(2)E_R$ are shown in Fig. 3C. The experimental spectra (Fig. 3D and E) for the same parameters are compared to the corresponding theoretically calculated spectra, shown in Fig. 3F and G. We focus on the features of the $|\downarrow\rangle$ channel of the spectrum, which is stronger because of the better spin-composition overlap with the reservoir state. The spectrum exhibits four prominent features separated by three energy gaps, labeled Δ_1, Δ_2 and Δ_3 in Fig. 3F and 3G. The gaps giving rise to these features are shown on the band structure in Fig. 3C. The gap Δ_1 is opened by the spin-orbit coupling, while Δ_2 is opened by a direct RF coupling and Δ_3 is opened by a second order process that involves both the RF and Raman fields, explaining its smallness. We have explored the Raman/RF system for a range of coupling strengths as shown in the spectra in Fig. 4B and 4C. The corresponding band structures are shown in Fig 4A. With a careful choice of the Raman/RF coupling strengths, spinful flat bands are realized, where interactions should play a dominant role [27].

To illustrate how the energy bands along with the corresponding eigenstates can be extracted, we reconstruct the energy bands along with the spin texture for $\hbar\Omega_R = 0.93(7)E_R$ and $\hbar\Omega_{RF} = 0.28(2)E_R$, as shown in Fig. 4D. The energies of the bands are obtained from the resonant frequencies in the spin-injection spectra, while the spin composition is extracted from the relative weights of the signal in the two spin channels (see Supplemental Material). In general, the eigenvector $\left|\psi^{(n)}(q)\right\rangle$ for the nth energy band at a given quasi-momentum q, can be expanded in terms of free space eigenstates as

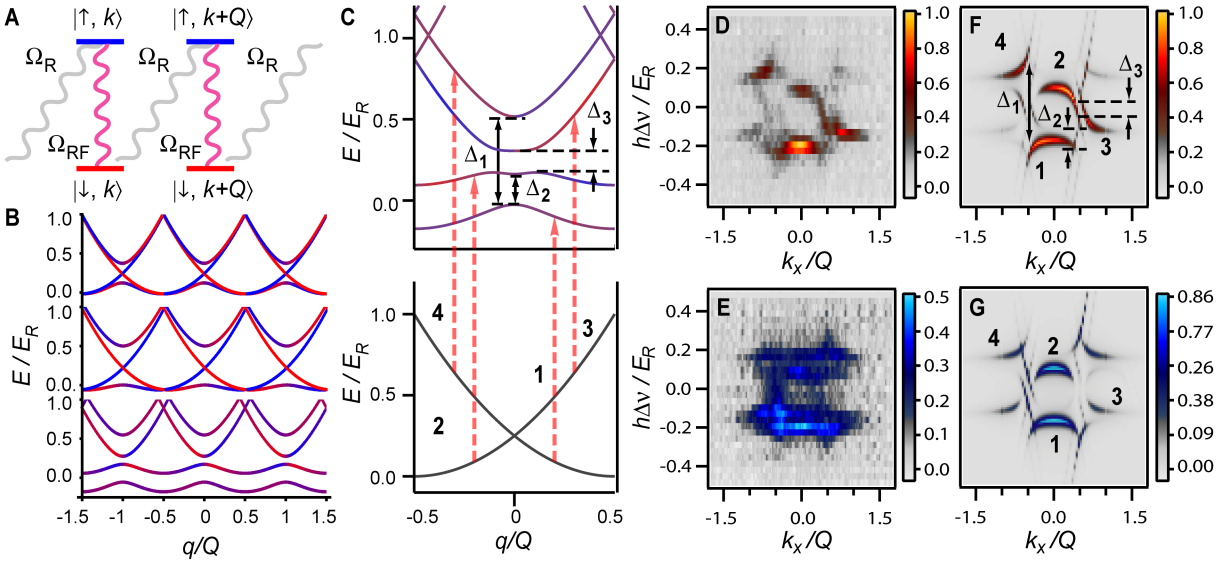

FIG. 3. Creating and probing a spin-orbit coupled lattice. (A) The addition of a radiofrequency field allows momentum transfer of any multiple of Q. The combined Raman-RF system produces a spinful lattice band structure. (B) The band structure of the Raman-RF system in the repeated zone scheme. The topmost band structure corresponds to $\hbar\Omega_{RF} = 0$ and $\hbar\Omega_R = 0.25E_R$, which has a band crossing at quasi-momentum $q = 0$. The middle band structure corresponds to a larger Raman coupling of $\hbar\Omega_R = 0.5E_R$ with $\hbar\Omega_{RF} = 0$. In the bottom-most band structure, $\hbar\Omega_R = 0.5E_R$ while $\hbar\Omega_{RF}$ is increased to $0.25E_R$. (C) Spin injection from free particle bands to spinful lattice bands, starting from $|\downarrow\rangle_R$. Transitions near zero RF detuning ($h\Delta\nu \sim 0$) that give rise to dominant spectral features are identified. (D and E) Experimental spectrum of the Raman-RF system with $\hbar\Omega_R = 0.40(5)E_R$ and $\hbar\Omega_{RF} = 0.28(2)E_R$ in the spin $|\downarrow\rangle$ and spin $|\uparrow\rangle$ channels, measured after injection from reservoir $|\downarrow\rangle_R$. The dominant features span many Brillouin zones, corresponding to projection of lattice states onto free particle states after time-of-flight. (F and G) The theoretical spectra corresponding to D and E, respectively. The features corresponding to the gaps and transitions identified in C are labeled.

$|\psi_n(q)\rangle = \sum_{m,\sigma} c_\sigma^{(n)}(k_x = q + mQ)\,|\sigma, k_x = q + mQ\rangle$. In spin-injection spectroscopy, the projection of the lattice wavefunctions onto free particle states allows us to not only extract the average spin, but also the magnitude of the coefficients $c_\sigma^{(n)}(k_x)$. From the projection coefficients $c_\sigma^{(n)}(k_x)$, one can define the spin $\vec{S}(k_x)$ (see Supplemental materials). In Fig. 4E, F and G, we show the extracted value of $S_y(k_x)$ and $|S_z(k_x)|$ for the bottommost band when $\hbar\Omega_R = 0.93(7)E_R$ and $\hbar\Omega_{RF} = 0.28(2)E_R$. For more general spin-orbit Hamiltonians involving σ_x, one can extract the phase between all three components of $\vec{S}(k_x)$ with additional RF pulses, and fully characterize the eigenstate for the corresponding quasimomentum q. The topology of the band, encoded in the evolution of its eigenstates across the Brillouin zone, can thus be measured.

In summary, we have created and directly probed a spin-orbit gap in a Fermi gas of ultracold atoms and realized a fully gapped band structure allowing for spinful flat bands. We introduced spin-injection spectroscopy to characterize the spin-textured energy-momentum dispersion. Such measurements would reveal the non-trivial topology of the bands in systems with more general spin-orbit couplings [28], opening a path to probing topological insulators with ultracold atoms. Recently developed high numerical aperture imaging techniques can be used for microscopic patterning of lower dimensional Fermi gases into heterostructures with regions characterized by different topological numbers separated by sharp interfaces [29, 30]. In such systems, spatially resolved spin-injection spectroscopy can directly reveal topologically protected edge states such as Majorana fermions, which have been proposed for topological quantum computation[10, 31, 32].

This work was supported by the NSF, a grant from the Army Research Office with funding from the DARPA OLE program, ARO-MURI on Atomtronics, AFOSR-MURI, ONR YIP, DARPA YFA, an AFOSR PECASE, and the David and Lucile Packard Foundation. Z. H. acknowledges funding from EPSRC under Grant No. EP/I010580/1.

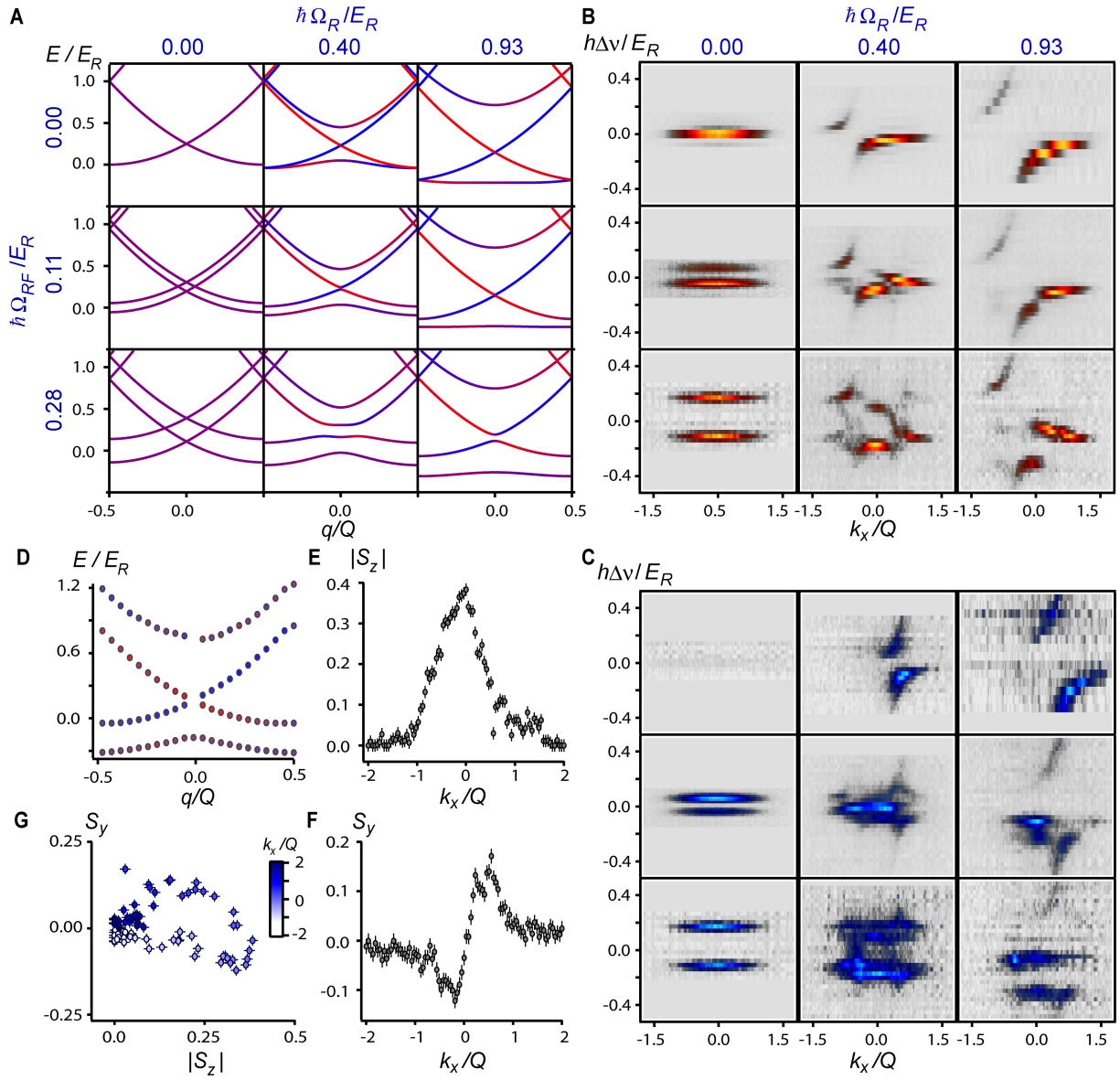

FIG. 4. Evolution of spin-textured energy bands of a spin-orbit coupled lattice. (A) Theoretical band structures for various combinations of Ω_R and Ω_{RF}. The first band becomes flat while remaining spinful for $\hbar\Omega_R = 0.93E_R$ and $\hbar\Omega_{RF} = 0.11E_R$ and $0.28E_R$. (B and C) The corresponding experimental Raman-RF spin-injection spectra for injection from $|\downarrow\rangle_R$ for channels $|\downarrow\rangle$ and $|\uparrow\rangle$, respectively. The color map used is the same as Fig. 2B and 2E after rescaling to the maximum intensity (which for 4C is 20% of 4E), except for the top left panel in (C), which is scaled to the maximum intensity of the corresponding panel in (B). Possible interaction effects between $|\uparrow\rangle$ with $|\downarrow\rangle_R$ (see Fig. S2) makes only the dominant features resolvable in $|\uparrow\rangle$, while finer features are visible in $|\downarrow\rangle$. (D) Experimentally reconstructed band structure for $\hbar\Omega_R = 0.93(7)E_R$ and $\hbar\Omega_{RF} = 0.28(2)$. The spin texture is indicated by the color of the points. (E,F and G) Experimentally measured spin components S_y and $|S_z|$ as a function of momentum k_x for the lattice wavefunctions corresponding to the bottommost band in D.

SUPPLEMENTAL MATERIALS

System preparation and Raman setup

Fermionic ^{6}Li in the hyperfine state $|F = 3/2, m_F = 3/2\rangle$ is sympathetically cooled to degeneracy by ^{23}Na atoms in a magnetic trap. The atoms are transferred to a nearly spherical crossed optical dipole trap with mean trapping frequency ~ 150 Hz. Depending on the measurement, the atoms are then transferred into one of the lowest four hyperfine states in the ground state manifold via radiofrequency (RF) sweeps. The four lowest hyperfine states are states $|\downarrow\rangle_R$, $|\downarrow\rangle$, $|\uparrow\rangle$, $|\uparrow\rangle_R$ in the text. Subsequently, the magnetic field is ramped to $\mathbf{B} = B_0\hat{z}$, with $B_0 = 11.6$ G. The geometry of the Raman beams is shown in Fig. 1B. The two beams, detuned by 3.96 GHz to the blue of the D_1 line, generate a moving lattice with lattice wavevector $Q = 2\pi \times (1.0\mu\text{m})^{-1}$ and corresponding recoil energy of $E_R = \frac{\hbar^2 Q^2}{2m} = h \times 32(1)$ kHz. The calibration of the recoil energy E_R is performed using the data in Fig. 1E and relies only on the relation of Q to the traveled distance for a given time-of-flight. To couple states $|\uparrow\rangle$ and $|\downarrow\rangle$, the frequency difference between the two beams is set near the hyperfine splitting of $\omega_0 = 2\pi\times$ 207.7 MHz. For the one-photon detuning that we use, $\Omega_R/\Gamma_{sc} \approx 240$, where Γ_{sc} is the scattering rate. Note that one-body losses from single-photon scattering events do not perturb the measured spin-injection spectra, as they affect all energy states equally and only reduce the number of atoms in each momentum state.

Experimental procedure

In the presence of the Raman beams, a differential Stark shift between $|\uparrow\rangle$ and $|\downarrow\rangle$ can alter the resonant two-photon frequency. The frequency corresponding to $\delta = 0$ is calibrated using RF spectroscopy on the $|\uparrow\rangle$ to $|\downarrow\rangle$ transition in the presence of the Raman beams with a large two-photon detuning $\delta \approx 2\pi\times1$ MHz. The resonant frequencies for $|\downarrow\rangle_R \to |\downarrow\rangle$ and $|\uparrow\rangle_R \to |\uparrow\rangle$ are calibrated similarly. The differential Stark shift for the largest Raman coupling strength is measured to be 4 kHz for $|\uparrow\rangle \to |\downarrow\rangle$, and < 1 kHz for the $|\downarrow\rangle_R \to |\downarrow\rangle$ and $|\uparrow\rangle_R \to |\uparrow\rangle$ transitions. For spin-injection spectroscopy, the injection process uses a RF field that couples the states $|\downarrow\rangle_R\,(|\uparrow\rangle_R)$ and $|\uparrow\rangle\,(|\downarrow\rangle_R)$. All spectra are taken with a RF injection pulse duration of 0.5 ms, and an injection field strength corresponding to a maximum transfer fraction < 0.30. The experimental frequency resolution for spin-injection is 3 kHz $\approx 0.1E_R$, while the momentum resolution is estimated to be $0.05Q$, limited by expansion time and imaging resolution. For all measurements, state-selective absorption images are taken after time-of-flight of 4 ms. As the atoms are released, the bias magnetic field is ramped to 300 G, where the resonant imaging frequencies for different hyperfine states are well-resolved, allowing spin-selective absorption imaging. To obtain the spectra shown in Fig. 1 and 2, the time-of-flight images for each spin state are first integrated along $\hat{y}$, orthogonal to the spin-orbit direction. For a given quasi-momentum q, the integrated one-dimensional density profiles from the two spin channels are then combined to produce the final spectrum. As an example, we show in Fig. S1 the time-of-flight images and the corresponding integrated density profiles, at a specific detuning δ/E_R for the spectrum in Fig. 1E.

Hamiltonian for Raman-coupled system

The spin of an atom is coupled to its momentum using a pair of laser beams near a Raman transition. Using the rotating wave approximation, the Raman beams generate a spinor potential

$$V(\vec{r}) = \frac{\hbar\Omega_R}{2}(\sigma_x \cos Qx - \sigma_y \sin Qx) + \frac{\delta}{2}\sigma_z, \qquad (2)$$

where Ω_R is the two-photon Rabi frequency. After a local pseudo-spin rotation about the z axis with angle Qx, the Hamiltonian becomes [19]

$$\mathcal{H} = \frac{\hbar^2\mathbf{k}^2}{2m} + \frac{\hbar^2 Q}{2m}\sigma_z q + \frac{\hbar\Omega_R}{2}\sigma_x + \frac{\delta}{2}\sigma_z + \frac{E_R}{4}, \qquad (3)$$

where q is the quasi-momentum defined in the text. Following a global pseudo-spin rotation $\sigma_z \to \sigma_y$, $\sigma_y \to \sigma_x$ and $\sigma_x \to \sigma_z$, the Hamiltonian becomes

$$\mathcal{H} = \frac{\hbar^2\mathbf{k}^2}{2m} + \frac{\hbar^2 Q}{2m}\sigma_y q + \frac{\hbar\Omega_R}{2}\sigma_z + \frac{\delta}{2}\sigma_y + \frac{E_R}{4}, \qquad (4)$$

which up to a constant has the same Rashba-Dresselhaus form as Eq. (1), with $\alpha = \beta = \frac{\hbar^2 Q}{2mg\mu_B}$, $B_y^{(Z)} = \hbar\delta/g\mu_B$ and $B_z^{(Z)} = \hbar\Omega_R/g\mu_B$. In this convention, the bare hyperfine states, labeled $|\uparrow\rangle$ and $|\downarrow\rangle$ are eigenstates of σ_y.

Reconstructing the spinful dispersion for the Raman-coupled system

For the equal Rashba-Dresselhaus system, the two channels in a spectrum from reservoir $|\sigma\rangle_R$ are first relabeled by quasi-momentum q. The ratio of the transferred atoms in each channel at a given q directly measures the q-dependent spin composition. The dispersion is then reconstructed by adding the free particle dispersion $\epsilon^0(q) = (q \mp Q/2)^2/2m$ to the spectrum corresponding to injection from $|\uparrow\rangle_R\,(|\downarrow\rangle_R)$. The result is shown in Fig. 2F,G and H, where the color denotes the spin texture and the strength of the color is weighed by the total number of atoms at a given q.

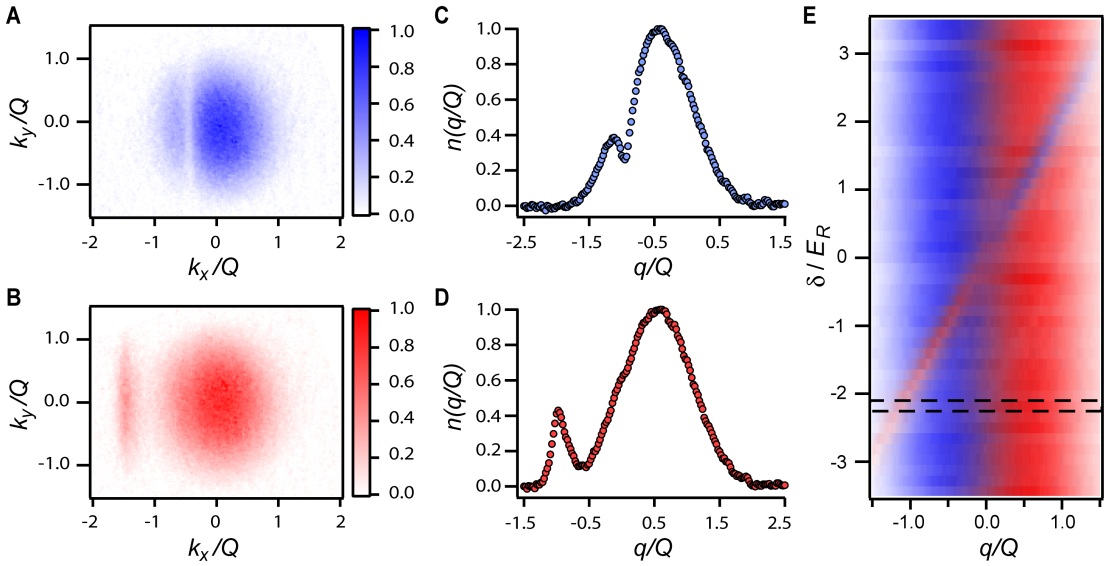

FIG. S1. Example of converting time-of-flight images to a spinful spectrum. Here, we show the conversion process for the spectrum in Fig. 1E for a specific detuning $\hbar\delta = -1.88E_R$. (A and B) Time-of-flight images rescaled in terms of the recoil momentum Q in the $|\uparrow\rangle$ and $|\downarrow\rangle$ channels, respectively. (C and D) The time-of-flight images in A and B are integrated along the k_y direction to produce 1-dimensional densities $n(q/Q)$. The conversion to quasi-momentum q involves adding a spin channel dependent momentum offset. (E) Combining C and D for every quasi-momentum q produces a slice in the final spectrum. In the figure, this is the region bounded by the two dashed lines. Repeating the same procedure for other detunings yields the full spectrum.

Hamiltonian for the Raman/RF system

Raman dressing creates a spin-orbit gap in momentum space. Adding radiofrequency (RF) coupling with zero momentum transfer creates a lattice potential with true band gaps [7]. The RF drive is applied at the same frequency as the Raman frequency, with coupling strength Ω_{RF}. An atom can now receive an arbitrary number of units of the recoil momentum $\hbar Q$ by interacting alternately with the Raman field and the RF field (see Figure 3(A)). When the two spin states are coupled at different momenta using Raman lasers, and additionally at the same momentum using RF, the Hamiltonian becomes

$$\mathcal{H} = \frac{\hbar^2 k^2}{2m} + \frac{\hbar\Omega_R}{2}(\sigma_x \cos Qx - \sigma_y \sin Qx) + \frac{\hbar\Omega_{RF}}{2}\sigma_x + \frac{\delta}{2}\sigma_z. \tag{5}$$

Since the Hamiltonian has discrete translational symmetry along $\hat{x}$, its eigenstates can be expanded in plane waves as

$$|\psi_n(k_x)\rangle = \sum_{j,\sigma=\uparrow,\downarrow} c_\sigma^{(n)}(k_x) \left|\sigma, k_x = \tilde{k}_x + jQ\right\rangle, \tag{6}$$

where $\tilde{k}_x$ is the quasi-momentum given by to k_x restricted to the first Brillouin zone, and n is the band index.

Spin-injection spectrum for the Raman/RF system

Starting from reservoir $\sigma = \uparrow, \downarrow$, the injected population in band n with quasi-momentum $\tilde{k}_x$ at a given RF frequency ω, $P_{I,\sigma}(\omega, n, m, \tilde{k}_x)$, is given by

$$P_{I,\sigma}(\omega, n, l, \tilde{k}_x) \propto \Omega_{I,\sigma}^2 \sum_j n_\sigma(\tilde{k}_x + lQ)|c_\sigma^{(n)}(\tilde{k}_x + jQ)|^2 \times \mathcal{L}((\hbar\omega + \epsilon_l^0(\tilde{k}_x + jQ)) - (\hbar\omega_0 + \epsilon_n(\tilde{k}_x))),$$

where $\Omega_{I,\sigma}$ is the RF strength coupling the reservoir state to $|\sigma\rangle$, $n_\sigma(k)$ is the trap-averaged momentum distribution for reservoir state $|\sigma\rangle_R$, $\epsilon_l^0(k) = \frac{\hbar^2(k+lQ)^2}{2m}$ is the free particle dispersion of the lth non-interacting band, $\epsilon_n(k)$ is the dispersion for the nth band, ω_0 is the hyperfine frequency difference between $|\uparrow\rangle$ and $|\downarrow\rangle$, and $\mathcal{L}(x)$ is the RF lineshape. After injection, the atoms are released from the trap. After sufficient time-of-flight, the momentum distribution is given by the real space atomic density profile, which for the spin σ' channel is

$$P_{\mathrm{TOF},\sigma',\sigma}(\omega, k_x) = \sum_{n,l} P_{I,\sigma}(\omega, n, l, \tilde{k}_x)|c_{\sigma'}^{(n)}(k_x)|^2. \tag{8}$$

The theoretical spectra in Fig. 3F and G are obtained using Eq. (8) and coefficients $c_\sigma^{(n)}(k_x)$ found by numerically diagonalizing the Hamiltonian in Eq. (5). The experimental and theoretical spectra for Fig. 4 are shown in Fig. S2.

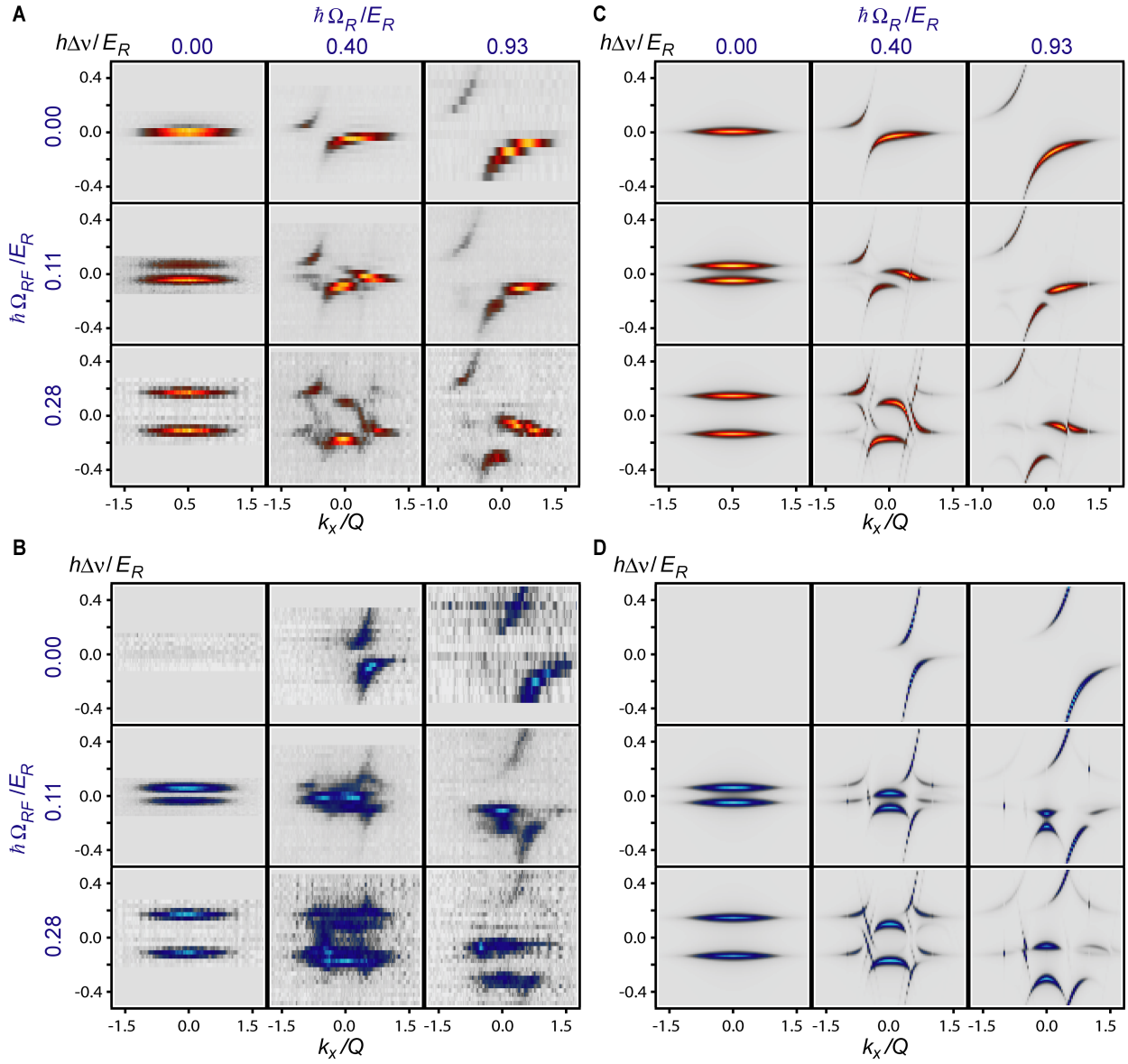

FIG. S2. Experimental and theoretical Spin-injection spectra of Raman/RF system for different Raman/RF strengths. (A and B) The experimental Raman/RF spin-injection spectra for injection from $|\downarrow\rangle_R$ for channels $|\downarrow\rangle$ and $|\uparrow\rangle$, respectively. The color map used is the same as Fig. 2B and 2E after rescaling to the maximum intensity (which for 4C is 20% of 4E), except for the top left panel in (B), which is scaled to the maximum intensity of the corresponding panel in (A). (C and D) Theoretical spectra corresponding to B and C. We do not take into account finite imaging resolution, which affects the sharpness along the momentum axis k_x/Q. Scattering due to residual interactions between hyperfine states can also lead to blurring of momenta along k_x/Q, and will be most pronounced for the spectra in B, as state $|\uparrow\rangle$ scatters more strongly with $|\downarrow\rangle_R$ (scattering length $\sim -450a_0$) than $|\downarrow\rangle$ does with $|\downarrow\rangle_R$ (scattering length $\sim -2a_0$ with typical initial $1/k_F \sim 3000a_0$ before TOF).

Reconstructing the spinful band structure for the Raman/RF System

We first describe a general procedure to reconstruct the band structure for any spinful lattice from spin-injection spectra. One performs spin-injection spectroscopy with reservoir states that are filled up to a Fermi momentum smaller than half the recoil momentum, $k_F < Q/2$. One then selects a prominent feature on the spectrum and finds the resonant transfer frequencies as a function of k_x, over one Brillouin zone. A mask centered on the resonant frequencies and repeated over all k_x with period Q is then created. With the mask for a specific feature applied, the spin channel σ' for the spectrum starting from $|\sigma\rangle_R$ has

transfer intensity given by

$$I_{\sigma',\sigma}(n,l,k_x) \propto \sum_j n_\sigma(\tilde{k}_x+lQ)|c_\sigma^{(n)}(\tilde{k}_x+jQ)|^2|c_{\sigma'}^{(n)}(k_x)|^2. \tag{9}$$

Here, the Fermi momentum k_F is less than half the recoil momentum $Q/2$ and therefore only the $l=0$ contributes. Defining $\mathcal{N}_\sigma(n,l,\tilde{k}_x)=\sum_{j,\sigma'} I_{\sigma',\sigma}(n,l,\tilde{k}_x+jQ)$, one obtains

$$|c_{\sigma'}^{(n)}(k_x)|^2 = \frac{I_{\sigma',\sigma}(n,l,k_x)}{\mathcal{N}_\sigma(n,l,\tilde{k}_x)}. \tag{10}$$

Defining $\vec{S}(k_x)=\frac{1}{2}\mathbf{c}^{(n)}(k_x)^\dagger\sigma\mathbf{c}^{(n)}(k_x)$, where $\mathbf{c}^{(n)}(k_x)=(c_\uparrow^{(n)}(k_x),c_\downarrow^{(n)}(k_x))^T$, allows to measure $S_z(k_x)$. With additional RF pulses, one can measure $S_x(k_x)$ and $S_y(k_x)$. After the bands that coupled strongly to $|\sigma,k\rangle, k<Q$ are measured, one iterates the process with a larger Fermi sea to obtain other bands.

In the text, we demonstrate extraction of band structure and spin texture in a spin-orbit coupled lattice. The initial Fermi sea has $k_F > Q$, therefore spectral features corresponding to transitions out of different non-interacting reservoir bands can all appear near zero RF detuning. One can however identify spectral features corresponding to different transitions and apply the above procedure. In addition, since the Raman/RF system is set to $\delta=0$, one can invoke the additional symmetry of the band structure about $q=0$, meaning that it is sufficient to fit a certain spectral feature over half of a Brillouin zone. Due to a larger signal in the $|\downarrow\rangle$ channel, features in this channel were used to create the mask.

In order to be consistent with the earlier convention for the Rashba-Dresselhaus system, we apply a global spin rotation such that $S_y(k_x)$ corresponds to $\frac{1}{2}\left(|c_\uparrow^{(n)}(k_x)|^2-|c_\downarrow^{(n)}(k_x)|^2\right)$. The experimentally measured $S_y(k_x)$ for the lowest band for $\hbar\Omega_R=0.93(7)E_R$ and $\hbar\Omega_{RF}=0.28(2)E_R$ is shown in Fig. 4F. Since the Hamiltonian only has components in the pseudospin $\hat{y}$ and $\hat{z}$ direction, one can also extract $|S_z(k_x)|=\sqrt{\frac{1}{4}-S_y(k_x)^2}$, as shown in Fig. 4E.

[1] M. König, *et al*. Quantum Spin Hall Insulator State in HgTe Quantum Wells. *Science* **318**, 766 (2007).

[2] D. Hsieh, *et al*. A topological dirac insulator in a quantum spin hall phase. *Rev. Mod. Phys.* **82**, 3045 (2010).

[3] M. Z. Hasan, C. L. Kane. *Colloquium*: Topological insulators. *Rev. Mod. Phys.* **82**, 3045 (2010).

[4] M. Inguscio, W. Ketterle, C. Salomon, eds., *Ultracold Fermi gases, Proceedings of the International School of Physics Enrico Fermi, Course CLXIV, Varenna, 20-30 June 2006* (IOS Press, Amsterdam, 2008).

[5] I. Bloch, J. Dalibard, W. Zwerger. Many-body physics with ultracold gases. *Rev. Mod. Phys.* **80**, 885 (2008).

[6] C. H. L. Quay, *et al*. Observation of a one-dimensional spin-orbit gap in a quantum wire. *Nat. Phys.* **6**, 336 (2010).

[7] K. Jiménez-García, *et al*. The Peierls substitution in an engineered lattice potential. *arXiv:1201.6630v1 [cond-mat.quant-gas]* (2012).

[8] R. A. Williams, *et al*. Synthetic partial waves in ultracold atomic collisions. *Science* **335**, 314 (2012).

[9] C. Zhang, S. Tewari, R. M. Lutchyn, S. Das Sarma. p_x+ip_y superfluid from s-wave interactions of fermionic cold atoms. *Phys. Rev. Lett.* **101**, 160401 (2008).

[10] M. Sato, Y. Takahashi, S. Fujimoto. Non-abelian topological order in s-wave superfluids of ultracold fermionic atoms. *Phys. Rev. Lett.* **103**, 020401 (2009).

[11] X.-L. Qi, S.-C. Zhang. Topological insulators and superconductors. *Rev. Mod. Phys.* **83**, 1057 (2011).

[12] G. Dresselhaus. Spin-orbit coupling effects in zinc blende structures. *Phys. Rev.* **100**, 580 (1955).

[13] R. Winkler, *Spin-Orbit Coupling Effects in Two-Dimensional Electron and Hole Systems*, vol. 191 of *Springer Tracts in Modern Physics* (Springer, Berlin, 2003).

[14] Y. A. Bychkov, E. I. Rashba. Oscillatory effects and the magnetic susceptibility of carriers in inversion layers. *J. Phys. C* **17**, 6039 (1984).

[15] S. Nadj-Perge, *et al*. Spectroscopy of spin-orbit quantum bits in indium antimonide nanowires. *Phys. Rev. Lett.* **108**, 166801 (2012).

[16] D. Xiao, M.-C. Chang, Q. Niu. Berry phase effects on electronic properties. *Rev. Mod. Phys.* **82**, 1959 (2010).

[17] X.-J. Liu, M. F. Borunda, X. Liu, J. Sinova. Effect of induced spin-orbit coupling for atoms via laser fields. *Phys. Rev. Lett.* **102**, 046402 (2009).

[18] J. Dalibard, F. Gerbier, G. Juzeliūnas, P. Öhberg. *Colloquium*: Artificial gauge potentials for neutral atoms. *Rev. Mod. Phys.* **83**, 1523 (2011).

[19] Y.-J. Lin, Jiménez-García, I. B. Spielman. Spin-orbit-coupled Bose-Einstein condensates. *Nature* **471**, 83 (2011).

[20] Y.-J. Lin, R. L. Compton, Jiménez-García, J. V. Porto, I. B. Spielman. Synthetic magnetic fields for ultracold neutral atoms. *Nature* **462**, 628 (2009).

[21] M. Aidelsburger, *et al*. Experimental realization of strong effective magnetic fields in an optical lattice. *Phys. Rev. Lett.* **107**, 255301 (2011).

[22] P. Wang, *et al*. Spin-Orbit Coupled Degenerate Fermi Gases. *arXiv:1204.1887v1 [cond-mat.quant-gas]* (2012).

[23] E. Zhao, N. Bray-Ali, C. J. Williams, I. B. Spielman, I. I. Satija. Chern numbers hiding in time-of-flight images. *Phys. Rev. A* **84**, 063629 (2011).

[24] M. Hoesch, *et al*. Spin-polarized fermi surface mapping. *Journal of Electron Spectroscopy and Related Phenomena* **124**, 263 (2002).

[25] D. Hsieh, *et al*. Observation of unconventional quantum spin textures in topological insulators. *Science* **323**, 919 (2009).

[26] J. T. Stewart, J. P. Gaebler, D. S. Jin. Using photoemission spectroscopy to probe a strongly interacting Fermi gas. *Nature* **454**, 744 (2008).

[27] K. Sun, Z. Gu, H. Katsura, S. Das Sarma. Nearly flatbands with nontrivial topology. *Phys. Rev. Lett.* **106**, 236803 (2011).

[28] J. D. Sau, R. Sensarma, S. Powell, I. B. Spielman,

S. Das Sarma. Chiral rashba spin textures in ultracold fermi gases. *Phys. Rev. B* **83**, 140510 (2011).

[29] W. S. Bakr, *et al*. Probing the Superfluid-to-Mott Insulator Transition at the Single-Atom Level. *Science* **329**, 547 (2010).

[30] J. Sherson, *et al*. Single-atom-resolved fluorescence imaging of an atomic Mott insulator. *Nature* **467**, 68 (2010).

[31] S. Tewari, S. Das Sarma, C. Nayak, C. Zhang, P. Zoller. Quantum computation using vortices and Majorana zero modes of a $p_x + ip_y$ superfluid of fermionic cold atoms. *Phys. Rev. Lett.* **98**, 010506 (2007).

[32] L. Jiang, *et al*. Majorana fermions in equilibrium and in driven cold-atom quantum wires. *Phys. Rev. Lett.* **106**, 220402 (2011).

will slow down their spin rates with time after the RLDP. However, they cannot explain the apparent difference in spin distributions between AXMSPs and radio MSPs, because radio MSPs, which have weak surface magnetic field strengths, could not spin down by the required amount even in a Hubble time. The true age of a pulsar (*23*) is given by $t = P/((n-1)\dot{P})[1-(P_0/P)^{n-1}]$. Assuming an evolution with a braking index $n = 3$ and $B = 1.0\times 10^8$ G, the time scale t is larger than 10 Gy, using $P_0 = \langle P\rangle_{\mathrm{AXMSP}} = 3.3$ ms and $P(t) = \langle P\rangle_{\mathrm{MSP}} = 5.5$ ms. To make things worse, one has to add the main-sequence lifetime of the LMXB donor star, which is typically 3 to 12 Gy, thereby reaching unrealistic large total ages. Although the statistics of AXMSPs still has its basis in small numbers and care must be taken for both detection biases (such as eclipsing effects of radio MSPs) and comparison between various subpopulations (*8*), it is evident from both observations and theoretical work that the RLDP effect presented here plays an important role for the spin distribution of MSPs.

The RLDP effect may also help explain a few other puzzles, for example, why characteristic (or spin-down) ages of radio MSPs often largely exceed cooling age determinations of their white dwarf companions (*24*). It has been suggested that standard cooling models of white dwarfs may not be correct (*25*–*27*), particularly for low-mass helium white dwarfs. These white dwarfs avoid hydrogen shell flashes at early stages and retain thick hydrogen envelopes, at the bottom of which residual hydrogen burning can continue for several billion years after their formation, keeping the white dwarfs relatively hot (~10^4 K) and thereby appearing much younger than they actually are. However, it is well known that the characteristic age is not a trustworthy measure of true age (*28*), and the RLDP effect exacerbates this discrepancy even further. In the model calculation presented in Fig. 1, it was assumed that $B = 1.0\times 10^8$ G and $\varphi = 1.0$. However, P_0 and τ_0 depend strongly on both B and φ. This is shown in Fig. 2, where I have calculated the RLDP effect for different choices of B and φ by using the same stellar donor model [i.e., same $\dot{M}(t)$ profile] as before. The use of other LMXB donor star masses, metallicities, and initial orbital periods would lead to other $\dot{M}(t)$ profiles (*16*, *17*) and hence different evolutionary tracks. The conclusion is that recycled MSPs can basically be born with any characteristic age. Thus, we are left with the cooling age of the white dwarf companion as the sole reliable, although still not accurate, measure as an age indicator.

A final puzzle is why no sub-millisecond pulsars have been found among the 216 radio MSPs detected in total so far. Although modern observational techniques are sensitive enough to pick up sub-millisecond radio pulsations, the fastest spinning known radio MSP, J1748−2446ad (*29*), has a spin frequency of only 716 Hz, corresponding to a spin period of 1.4 ms. This spin rate is far from the expected minimum equilibrium spin period (*8*) and the physical mass shedding limit of about 1500 Hz. It has been suggested that gravitational wave radiation during the accretion phase halts the spin period above a certain level (*30*, *31*). The RLDP effect presented here is a promising candidate for an alternative mechanism, in case a sub-millisecond AXMSP is detected (*8*).

References and Notes

1. M. A. Alpar, A. F. Cheng, M. A. Ruderman, J. Shaham, *Nature* **300**, 728 (1982).
2. D. Bhattacharya, E. P. J. van den Heuvel, *Phys. Rep.* **203**, 1 (1991).
3. L. Bildsten *et al.*, *Astrophys. J. Suppl. Ser.* **113**, 367 (1997).
4. R. Wijnands, M. van der Klis, *Nature* **394**, 344 (1998).
5. J. W. T. Hessels *et al.*, *AIP Conf. Proc.* **1068**, 130 (2008).
6. The Roche lobe of a binary star is the innermost equipotential surface passing through the first Lagrangian point, L1. If a star fills its Roche lobe, the unbalanced pressure at L1 will cause mass transfer to the other star (*2*).
7. A. M. Archibald *et al.*, *Science* **324**, 1411 (2009); 10.1126/science.1172740.
8. Materials and methods are available as supporting material on *Science* Online.
9. F. K. Lamb, C. J. Pethick, D. A. Pines, *Astrophys. J.* **184**, 271 (1973).
10. P. Ghosh, F. K. Lamb, *NATO Sci. Ser.* **377**, 487 (1992).
11. J. Frank, A. King, D. J. Raine, *Accretion Power in Astrophysics* (Cambridge Univ. Press, Cambridge, 2002).
12. A. F. Illarionov, R. A. Sunyaev, *Astron. Astrophys.* **39**, 185 (1975).
13. M. Ruderman, J. Shaham, M. Tavani, *Astrophys. J.* **336**, 507 (1989).
14. R. F. Webbink, S. Rappaport, G. J. Savonije, *Astrophys. J.* **270**, 678 (1983).
15. S. Rappaport, Ph. Podsiadlowski, P. C. Joss, R. Di Stefano, Z. Han, *Mon. Not. R. Astron. Soc.* **273**, 731 (1995).
16. T. M. Tauris, G. J. Savonije, *Astron. Astrophys.* **350**, 928 (1999).
17. Ph. Podsiadlowski, S. Rappaport, E. D. Pfahl, *Astrophys. J.* **565**, 1107 (2002).
18. The magnetospheric coupling parameter, $0.5 < \varphi < 1.4$ is a numerical factor of order unity depending on the accretion flow, the disk model, and the magnetic inclination angle of the pulsar (*10*, *11*, *32*–*34*).
19. S. L. Shapiro, S. A. Teukolsky, *Black Holes, White Dwarfs, and Neutron Stars: The Physics of Compact Objects* (Wiley-Interscience, New York, 1983).
20. S. A. Rappaport, J. M. Fregeau, H. C. Spruit, *Astrophys. J.* **606**, 436 (2004).
21. L. Burderi *et al.*, *Astrophys. J.* **560**, L71 (2001).
22. This "turn-off problem" has previously been debated elsewhere (*13*, *33*, *35*).
23. R. N. Manchester, J. H. Taylor, *Pulsars* (Freeman, San Francisco, CA, 1977).
24. D. R. Lorimer, A. G. Lyne, L. Festin, L. Nicastro, *Nature* **376**, 393 (1995).
25. F. Alberts, G. J. Savonije, E. P. J. van den Heuvel, O. R. Pols, *Nature* **380**, 676 (1996).
26. L. A. Nelson, E. Dubeau, K. A. MacCannell, *Astrophys. J.* **616**, 1124 (2004).
27. M. H. van Kerkwijk, C. G. Bassa, B. A. Jacoby, P. G. Jonker, in *Binary Radio Pulsars*, F. A. Rasio, I. H. Stairs, Eds. [Astronomical Society of the Pacific (ASP) Conference Series, San Francisco, CA, 2005], vol. 328, pp. 357–370.
28. This is the case if the pulsar spin period, P, is close to its initial spin period, P_0.
29. J. W. T. Hessels *et al.*, *Science* **311**, 1901 (2006).
30. L. Bildsten, *Astrophys. J.* **501**, L89 (1998).
31. D. Chakrabarty *et al.*, *Nature* **424**, 42 (2003).
32. Y.-M. Wang, *Astrophys. J.* **475**, L135 (1997).
33. F. Lamb, W. Yu, in *Binary Radio Pulsars*, F. A. Rasio, I. H. Stairs, Eds. (ASP Conference Series, San Francisco, CA, 2005), vol. 328, pp. 299–310.
34. C. R. D'Angelo, H. C. Spruit, *Mon. Not. R. Astron. Soc.* **406**, 1208 (2010).
35. M. Ruderman, J. Shaham, M. Tavani, D. Eichler, *Astrophys. J.* **343**, 292 (1989).
36. A. Patruno, *Astrophys. J.* **722**, 909 (2010).
37. I. S. Shklovskii, *Sov. Astron.* **13**, 562 (1970).

Acknowledgments: I gratefully thank N. Langer and M. Kramer for discussions and funding and without whom these results would not be possible and R. Eatough for helpful comments on the SOM. This work was partly supported by the Cluster of Excellence proposal EXC 1076, "The nature of forces and matter," at the University of Bonn. Radio pulsar data has been obtained from the *ATNF Pulsar Catalogue* (www.atnf.csiro.au/research/pulsar/psrcat/).

Supporting Online Material

www.sciencemag.org/cgi/content/full/335/6068/561/DC1
Materials and Methods
SOM Text
Figs. S1 and S2
References (*38*–*54*)

8 November 2011; accepted 6 January 2012
10.1126/science.1216355

Revealing the Superfluid Lambda Transition in the Universal Thermodynamics of a Unitary Fermi Gas

Mark J. H. Ku, Ariel T. Sommer, Lawrence W. Cheuk, Martin W. Zwierlein*

Fermi gases, collections of fermions such as neutrons and electrons, are found throughout nature, from solids to neutron stars. Interacting Fermi gases can form a superfluid or, for charged fermions, a superconductor. We have observed the superfluid phase transition in a strongly interacting Fermi gas by high-precision measurements of the local compressibility, density, and pressure. Our data completely determine the universal thermodynamics of these gases without any fit or external thermometer. The onset of superfluidity is observed in the compressibility, the chemical potential, the entropy, and the heat capacity, which displays a characteristic lambda-like feature at the critical temperature $T_c/T_F = 0.167(13)$. The ground-state energy is $\frac{3}{5}\xi N E_F$ with $\xi = 0.376(4)$. Our measurements provide a benchmark for many-body theories of strongly interacting fermions.

Phase transitions are ubiquitous in nature: Water freezes into ice, electron spins suddenly align as materials turn into magnets, and metals become superconducting. Near the transitions, many systems exhibit critical behavior, reflected by singularities in thermodynamic quantities: The magnetic susceptibility diverges at a ferromagnetic transition, and the specific heat

Downloaded from www.sciencemag.org on February 6, 2012

shows a jump at superconducting and superfluid transitions (*1*, *2*), resolved as the famous lambda peak in ^{4}He (*3*). A novel form of superfluidity has been realized in trapped, ultracold atomic gases of strongly interacting fermions, particles with half-integer spin (*4*–*7*). Thanks to an exquisite control over relevant system parameters, these gases have recently emerged as a versatile system well suited to solve open problems in many-body physics (*7*).

Initial measurements on the thermodynamics of strongly interacting Fermi gases have focused on trap-averaged quantities (*8*–*10*) in which the superfluid transition is inherently difficult to observe. The emergence of the condensate of fermion pairs in a spin-balanced Fermi gas is accompanied by only minute changes in the gas density (*5*). Quantities that involve integration of the density over the local potential, such as the energy E (*11*) and the pressure P (*12*), are only weakly sensitive to the sudden variations in the thermodynamics of the gas expected near the superfluid phase transition (*13*).

For a neutral gas, thermodynamic quantities involving the second derivative of the pressure P are expected to become singular at the second-order phase transition into the superfluid state. An example is the isothermal compressibility $\kappa = \frac{1}{n}\frac{\partial n}{\partial P}|_T$, the relative change of the gas density n due to a change in the pressure P. Because the change in pressure is related to the change in chemical potential μ of the gas via $dP = n\,d\mu$ at constant temperature, $\kappa = \frac{1}{n^2}\frac{\partial^2 P}{\partial \mu^2}|_T$ is a second derivative of the pressure, and thus should reveal a clear signature of the transition.

The general strategy to determine the thermodynamic properties of a given substance is to measure an equation of state (EoS), such as the pressure $P(\mu,T)$ as a function of the chemical potential μ and the temperature T. Equivalently, replacing the pressure by the density $n = \frac{\partial P}{\partial \mu}|_T$, one can determine the density EoS $n(\mu,T)$. We directly measure the local gas density $n(V)$ as a function of the local potential V from in situ absorption images of a trapped, strongly interacting Fermi gas of ^{6}Li atoms at a Feshbach resonance (*5*). The trapping potential is cylindrically symmetric, with harmonic confinement along the axial direction; this symmetry allows us to find the three-dimensional (3D) density through the inverse Abel transform of the measured column density (*14*, *15*). The local potential is directly determined from the atomic density distribution and the accurately known harmonic potential along the axial direction.

The compressibility κ follows as the change of the density n with respect to the local potential V experienced by the trapped gas. The change in the local chemical potential is given by the negative change in the local potential, $d\mu = -dV$, and hence the local compressibility is $\kappa = -\frac{1}{n^2}\frac{dn}{dV}|_T$. We can then replace the unknown chemical potential μ in the density EoS $n(\mu,T)$ by the known variation of n with μ in the atom trap, given by κ. Instead of the a priori unknown temperature T, we determine the pressure $P(V) = \int_{-\infty}^{\mu} d\mu' n(\mu') = \int_V^{\infty} dV' n(V')$ given by the integral of the density over the potential (*16*). The resulting equation of state $n(\kappa,P)$ contains only quantities that can be directly obtained from the density distribution. This represents a crucial advance over previous methods that require the input of additional thermodynamic quantities, such as the temperature T and the chemical potential μ, whose determination requires the use of a fitting procedure or an external thermometer, as in (*11*, *12*).

We normalize the compressibility and the pressure by the respective quantities at the same local density for a noninteracting Fermi gas at $T = 0$, $\kappa_0 = \frac{3}{2}\frac{1}{nE_F}$, and $P_0 = \frac{2}{5}nE_F$, where $E_F = \frac{\hbar^2(3\pi^2 n)^{2/3}}{2m}$ is the local Fermi energy and m is the particle mass, yielding $\tilde{\kappa} \equiv \kappa/\kappa_0$ and $\tilde{p} \equiv P/P_0$. For dilute gases at the Feshbach resonance, the scattering length diverges and is no longer a relevant length scale. In the absence of an interaction-dependent length scale, the thermodynamics of such resonant gases are universal (*17*), and $\tilde{\kappa}$ is a universal function of $\tilde{p}$ only. Every experimental profile $n(V)$, irrespective of the trapping potential, the total number of atoms, or the temperature, must produce the same universal curve $\tilde{\kappa}$ versus $\tilde{p}$. By averaging many profiles, one obtains a low-noise determination of $\tilde{\kappa}(\tilde{p})$.

Our method has been tested on the noninteracting Fermi gas that can be studied in two independent ways: in spin-balanced gases near the zero-crossing of the scattering length and in the wings of highly imbalanced clouds at unitarity, where only one spin state is present locally. Both determinations yield the same noninteracting compressibility EoS (Fig. 1).

Figure 1 also shows the compressibility equation of state $\tilde{\kappa}(\tilde{p})$ for the unitary Fermi gas. In the high-temperature ($\tilde{p} >> 1$) regime, the pressure, and hence all other thermodynamic quantities, allow for a Virial expansion in terms of the fugacity $e^{\beta\mu}$ (*18*): $P\,\beta\lambda^3 = 2\sum_j b_j\, e^{j\beta\mu}$, with the nth-order Virial coefficients b_n. It is known that $b_1 = 1$, $b_2 = 3\sqrt{2}/8$, and $b_3 = -0.29095295$ (*18*); our data show good agreement with the third-order Virial expansion. Fixing b_2 and b_3, our measurement yields a prediction for $b_4 = +0.065(10)$, in agreement with (*12*), but contradicting a recent four-body calculation that gives a negative sign (*19*).

At degenerate temperatures ($\tilde{p} \lesssim 1$), the normalized compressibility rises beyond that of a noninteracting Fermi gas, as expected for an attractively interacting gas. A sudden rise of the compressibility at around $\tilde{p} = 0.55$, followed by a decrease at lower temperatures marks the superfluid transition. The expected singularity of the compressibility at the transition is rounded off by the finite resolution of our imaging system. Below the transition point, the decrease of the compressibility is consistent with the expectation from Bardeen-Cooper-Schrieffer (BCS) theory, in which

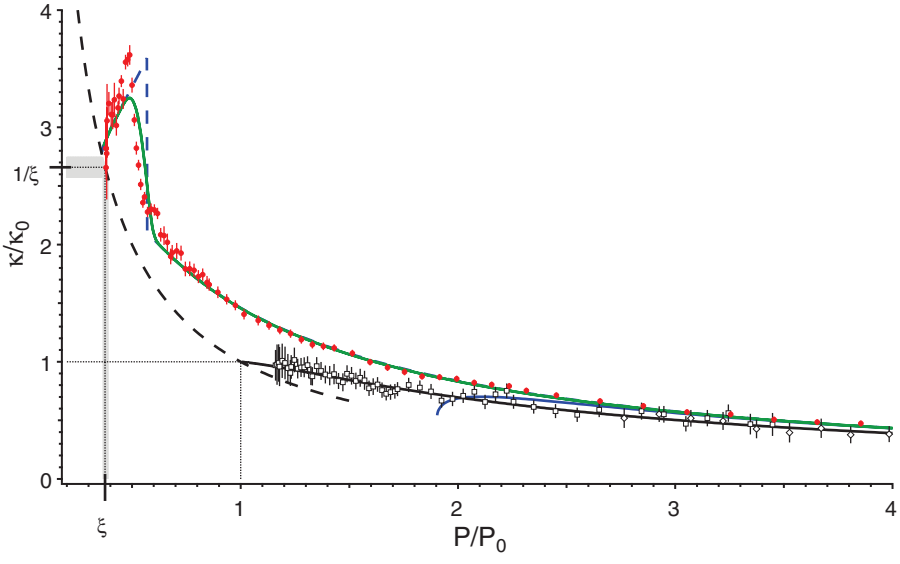

Fig. 1. Normalized compressibility κ/κ_0 versus normalized pressure P/P_0 of the unitary Fermi gas (red solid circles). Each data point is the average of between 30 and 150 profiles. The error bars show mean ± SD, including systematic errors from image calibration (*13*). Blue solid line: third-order Virial expansion. Black open squares (black open diamonds): data for a noninteracting Fermi gas obtained with a highly spin-imbalanced mixture at the Feshbach resonance (spin-balanced gas near zero-crossing of the scattering length). Black solid curve: theory for a noninteracting Fermi gas. Black dashed curve: the relation $\tilde{\kappa} = 1/\tilde{p}$ that must be obeyed at zero temperature both for the noninteracting gas ($\tilde{\kappa} = 1/\tilde{p} = 1$) and the unitary gas ($\tilde{\kappa} = 1/\tilde{p} = 1/\xi$) (dotted lines). Gray band: the uncertainty region for the $T = 0$ value of $\tilde{\kappa} = 1/\xi$ and $\tilde{p} = \xi$. Blue dashed curve: model for the EoS of the unitary Fermi gas [above T_c: interpolation from the Monte Carlo calculation (*34*); below T_c: BCS theory, including phonon and pair-breaking excitations]. Green solid curve: effect of 2 μm optical resolution on the model EoS.

Department of Physics, Massachusetts Institute of Technology (MIT), MIT Harvard Center for Ultracold Atoms, and Research Laboratory of Electronics, MIT, Cambridge, MA 02139, USA.

*To whom correspondence should be addressed. E-mail: zwierlein@mit.edu

Downloaded from www.sciencemag.org on February 6, 2012

single-particle excitations freeze out and pairs form (see model in Fig. 1).

As $T \to 0$, the Fermi energy E_F is the only intensive energy scale, so the chemical potential must be related to E_F by a universal number, $\mu = \xi E_F$, where ξ is known as the Bertsch parameter (*6*, *7*). It follows that at $T = 0$, $\tilde{\kappa} = 1/\tilde{p} = 1/\xi$ (*13*). The extrapolation of the low-temperature experimental data for $\tilde{\kappa}(\tilde{p})$ toward the curve $\tilde{\kappa} = 1/\tilde{p}$ gives $\xi = 0.37(1)$, a value that we find consistently for the normalized chemical potential, energy, and free energy at our lowest temperatures.

From the universal function $\tilde{\kappa}(\tilde{p})$, we obtain all other thermodynamic quantities of the unitary gas. First, to find the normalized temperature T/T_F (where $k_B T_F = E_F$), note that the change in pressure with T/T_F at constant temperature is related to the compressibility. One finds $\frac{d\tilde{p}}{d(T/T_F)} = \frac{5}{2}\frac{T_F}{T}\left(\tilde{p} - \frac{1}{\tilde{\kappa}}\right)$, so by integration (*13*)

$$\frac{T}{T_F} = \left(\frac{T}{T_F}\right)_i exp\left\{\frac{2}{5}\int_{\tilde{p}_i}^{\tilde{p}} d\tilde{p}\,\frac{1}{\tilde{p} - \frac{1}{\tilde{\kappa}}}\right\} \qquad (1)$$

where $(T/T_F)_i$ is the normalized temperature at an initial normalized pressure $\tilde{p}_i$ that can be chosen to lie in the Virial regime validated above.

Thanks to the relation $E = \frac{3}{2}PV$, valid at unitarity (*17*), we can also directly obtain the heat capacity per particle at constant volume V (*13*),

$$\frac{C_V}{k_B N} \equiv \frac{1}{k_B N}\frac{\partial E}{\partial T}\Big|_{N,V} = \frac{3}{5}\frac{d\tilde{p}}{d(T/T_F)} = \frac{3}{2}\frac{T_F}{T}\left(\tilde{p} - \frac{1}{\tilde{\kappa}}\right) \qquad (2)$$

Figure 2 shows the normalized compressibility and the specific heat as a function of T/T_F. At high temperatures, the specific heat approaches that of a noninteracting Fermi gas and eventually $C_V = \frac{3}{2} N k_B$, the value for a Boltzmann gas. A dramatic rise is observed for T/T_F at around 0.16, followed by a steep drop at lower temperatures. Such a λ-shaped feature in the specific heat is characteristic of second-order phase transitions, as in the famous λ transition in ^{4}He (*3*). Jumps in the specific heat are well known from superconductors (*1*) and ^{3}He (*2*). In experiments on atomic gases, such jumps had only been inferred from derivatives to fit functions that implied a jump (*20*, *21*). We do not expect to resolve the critical behavior very close to T_c. Because of the spatially varying chemical potential in our trapped sample, the critical region is confined to a narrow shell.

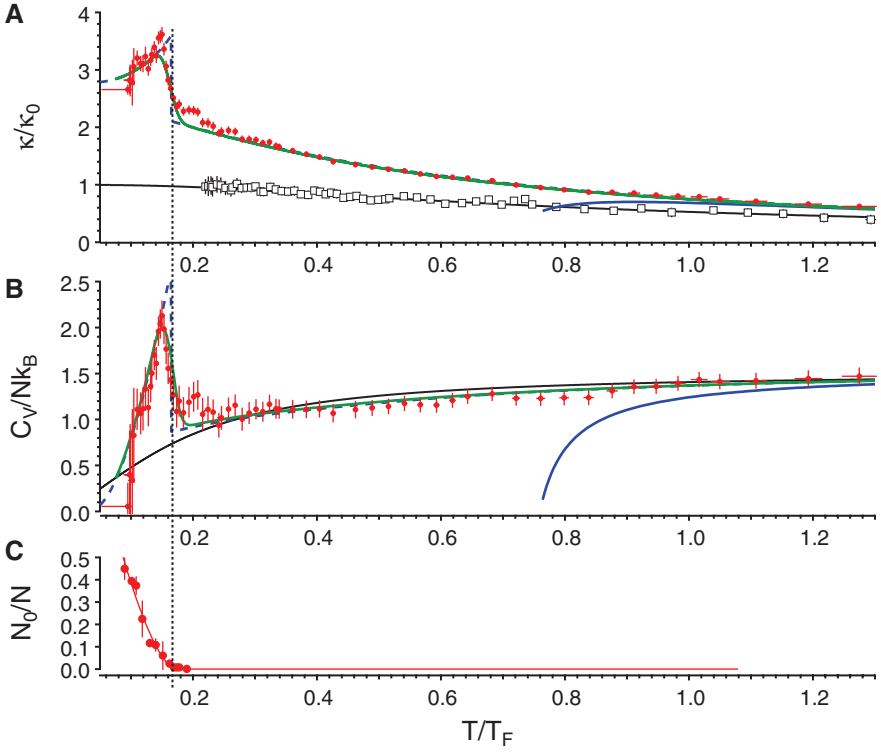

Fig. 2. (**A**) Normalized compressibility $\tilde{\kappa} = [2/3]\kappa\, n\, E_F$ and (**B**) specific heat per particle C_V/Nk_B of a unitary Fermi gas as a function of reduced temperature T/T_F (solid red circles). Black solid curve: theory for a noninteracting Fermi gas. Blue solid curve: third-order Virial expansion for the unitary gas. Black open squares: data for the normalized compressibility as a function of T/T_F of a noninteracting Fermi gas (combining data from both highly imbalanced gases at unitarity and balanced gases near zero-crossing). Blue dashed (green solid) curve: model from Fig. 1, excluding (including) the effect of finite imaging resolution. (**C**) Global condensate fraction at unitarity as determined from a rapid ramp to the molecular side of the Feshbach resonance, plotted as a function of local T/T_F at the trap center. The onset of condensation coincides with the sudden rise of the specific heat. Error bars, mean ± SD.

Based on the estimate in (*22*), the thickness of the critical shell is 1% of the cloud size. The finite resolution of our imaging system (2 μm or about 5% of the cloud size in the radial direction) suffices to explain the rounding of the singularity expected from criticality. The rounding also reduces the observed jump in the heat capacity at the transition. We obtain a lower bound $\Delta C/C_n \equiv (C_s - C_n)/C_n \geq 1.0^{+4}_{-1}$, where C_s/N (C_n/N) is the specific heat per particle at the peak (the onset of the sudden rise). Considering the strong interactions, this is surprisingly close to the BCS value of 1.43 (*1*). Below T_c, the specific heat is expected to decrease as $\sim \exp(-\Delta_0/k_B T)$ due to the pairing gap Δ_0. At low temperatures, $T << T_c$, the phonon contribution $\propto T^3$ dominates (*23*). This behavior is consistent with our data, but the phonon regime is not resolved.

To validate our in situ measurements of the superfluid phase transition, we have employed the rapid ramp method to detect fermion pair condensation (*24*, *25*). The results (Fig. 2C) show that the onset of condensation and the sudden rise in specific heat and compressibility all occur at the same critical temperature, within the error bars. Unlike previous experimental determinations of T_c/T_F for the homogeneous unitary Fermi gas (*11*, *12*), we determine T_c/T_F directly from the density profiles, finding a sudden rise in the specific heat and the onset of condensation at $T_c/T_F = 0.167(13)$. This value is determined as the midpoint of the sudden rise, and the error is assessed as the shift due to the uncertainty of the Feshbach resonance (*13*). This is in very good agreement with theoretical determinations, such as the self-consistent T-matrix approach that gives $T_c/T_F \approx 0.16$ (*23*), and Monte Carlo calculations that give $T_c/T_F = 0.171(5)$ (*26*) and 0.152(7) (*27*). There is a current debate on the possibility of a pseudogap phase of preformed pairs above T_c (*12*, *28*). A pairing gap for single-particle excitations above the transition should be signaled by a downturn of the specific heat above T_c, which is not observed in our measurements.

From the definition of the compressibility $\kappa = \frac{1}{n^2}\frac{\partial n}{\partial \mu}\big|_T$, we can obtain the reduced chemical potential μ/E_F as a function of the T/T_F (Fig. 3A) (*13*). This function is here obtained from measured quantities, rather than from numerical derivatives of data that involved uncontrolled thermometry (*11*). In the interval of T/T_F from around 0.25 to 1, the chemical potential is close to that of a noninteracting Fermi gas, shifted by $(\xi_n - 1)E_F$ because of interactions present in the normal state, with $\xi_n \approx 0.45$. Unlike a normal Fermi gas, the chemical potential attains a maximum of $\mu/E_F = 0.42(1)$ at $T/T_F = 0.171(10)$, and then decreases at lower temperatures, as expected for a superfluid of paired fermions (*23*). As the temperature is increased from zero in a superfluid, first the emergence of phonons (sound excitations) and then the breaking of fermion pairs contribute to increasing the chemical potential. At T_c, the singular compressibility implies a sharp change in slope for μ/E_F, in agreement with our observa-

Downloaded from www.sciencemag.org on February 6, 2012

tion and theory (*23*). At low temperatures, the reduced chemical potential μ/E_F saturates to the universal value ξ. As the internal energy E and the free energy F satisfy $E(T) > E(0) = \frac{3}{5}N\xi E_F = F(0) > F(T)$ for all T, the reduced quantities $f_E \equiv \frac{5}{3}\frac{E}{NE_F} = \tilde{p}$ and $f_F \equiv \frac{5}{3}\frac{F}{NE_F} = \frac{5}{3}\frac{\mu}{E_F} - \frac{2}{3}\tilde{p}$ (Fig. 3A) provide upper and lower bounds for ξ (*29*). Taking the coldest points of these three curves and including the systematic error due to the effective interaction range, we find $\xi = 0.376(4)$. The uncertainty in the Feshbach resonance is expected to shift ξ by at most 2% (*13*). This value is consistent with a recent upper bound $\xi < 0.383(1)$ from (*30*), is close to $\xi = 0.36(1)$ from a self-consistent T-matrix calculation (*23*), and agrees with $\xi = 0.367(9)$ from an epsilon expansion (*31*). It lies below earlier estimates $\xi = 0.44(2)$ (*32*) and $\xi = 0.42(1)$ (*33*) from fixed-node quantum Monte Carlo calculation that provides upper bounds on ξ. Our measurement agrees with several less accurate experimental determinations (*6*) but disagrees with the most recent experimental value 0.415(10) that was used to calibrate the pressure in (*12*).

From the energy, pressure, and chemical potential, we can obtain the entropy $S = \frac{1}{T}(E + PV - \mu N)$, and hence the entropy per particle $S/Nk_B = \frac{T_F}{T}\left(\tilde{p} - \frac{\mu}{E_F}\right)$ as a function of T/T_F (Fig. 3B). At high temperatures, S is close to the entropy of an ideal Fermi gas at the same T/T_F. Above T_c, the entropy per particle is nowhere small compared with k_B. Also, the specific heat C_V is not linear in T in the normal phase. This shows that the normal regime above T_c cannot be described in terms of a Landau Fermi Liquid picture, although some thermodynamic quantities agree surprisingly well with the expectation for a Fermi liquid [see (*12*) and (*13*)]. Below about $T/T_F = 0.17$, the entropy starts to strongly fall off compared with that of a noninteracting Fermi gas, which we again interpret as the freezing out of single-particle excitations as a result of the formation of fermion pairs. Far below T_c, phonons dominate. They only have a minute contribution to the entropy (*23*), less than 0.02 k_B at $T/T_F = 0.1$, consistent with our measurements. At the critical point, we obtain $S_c = 0.73(13)$ Nk_B, in agreement with theory (*23*). It is encouraging for future experiments with fermions in optical lattices that we obtain entropies less than 0.04 N k_B, far below critical entropies required to reach magnetically ordered phases.

From the chemical potential μ/E_F and $T/T_F = \frac{4\pi}{(3\pi^2)^{2/3}}\frac{1}{(n\lambda^3)^{2/3}}$, we finally obtain the density EoS $n(\mu,T) \equiv \frac{1}{\lambda^3}f_n(\beta\mu)$, with the de Broglie wavelength $\lambda = \sqrt{\frac{2\pi\hbar^2}{mk_BT}}$. The pressure EoS follows as $P(\mu,T) \equiv \frac{k_BT}{\lambda^3}f_P(\beta\mu)$, with $f_P = \frac{2}{5}\frac{T_F}{T}\tilde{p}f_n(\beta\mu)$. Figure 4 shows the density and pressure normalized by their noninteracting counterparts at the same chemical potential and temperature. For the normal state, a concurrent theoretical calculation employing a new Monte Carlo method agrees excellently with our data (*34*). Our data deviate from a previous experimental determination of the pressure EoS (*12*) that was calibrated with an independently measured value of $\xi = 0.415(10)$ (*35*) and disagree with the energy measurement in (*11*) that used a thermometry inconsistent with the Virial expansion (*10*). Around

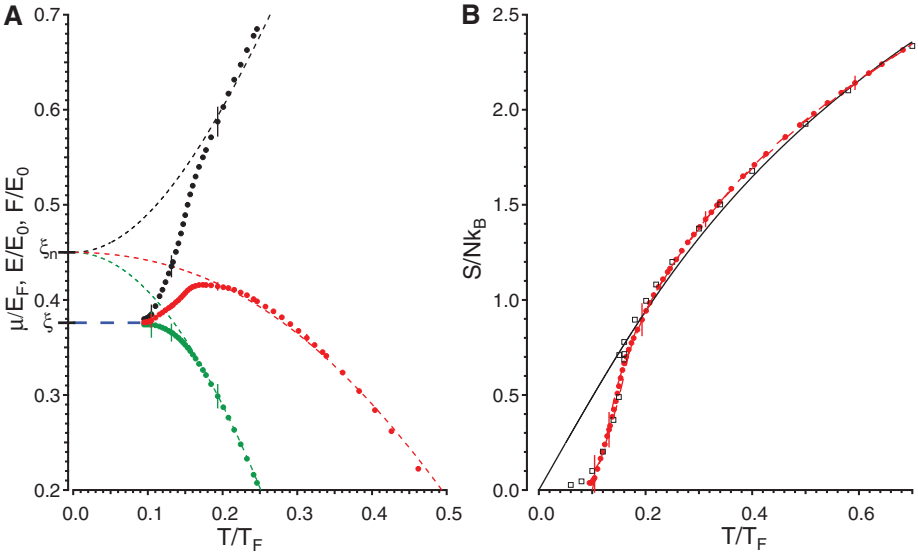

Fig. 3. (**A**) Chemical potential μ, energy E, and free energy F of the unitary Fermi gas versus T/T_F. μ (red solid circles) is normalized by the Fermi energy E_F, and E (black solid circle) and F (green solid circle) are normalized by $E_0 = \frac{3}{5}N\,E_F$. At high temperatures, all quantities approximately track those for a noninteracting Fermi gas, shifted by $\xi_n - 1$ (dashed curves). The peak in the chemical potential signals the onset of superfluidity. In the deeply superfluid regime at low temperatures, μ/E_F, E/E_0, and F/F_0 all approach ξ (blue dashed line). (**B**) Entropy per particle. At high temperatures, the entropy closely tracks that of a noninteracting Fermi gas (black solid curve). The open squares are from the self-consistent T-matrix calculation (*23*). A few representative error bars are shown, representing mean ± SD.

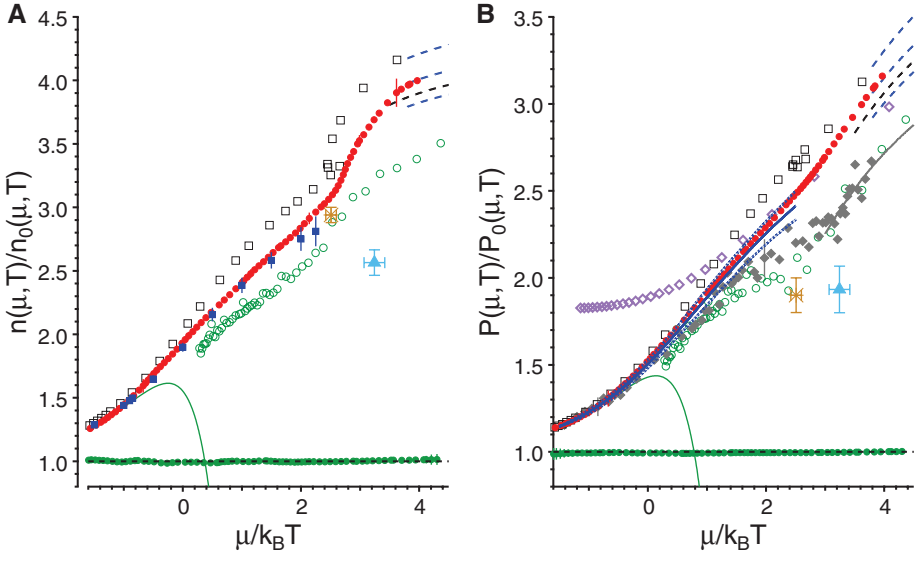

Fig. 4. (**A**) Density and (**B**) pressure of a unitary Fermi gas versus μ/k_BT, normalized by the density and pressure of a noninteracting Fermi gas at the same chemical potential μ and temperature T. Red solid circles: experimental EoS. Blue dashed curves: low-temperature behavior with $\xi = 0.364$ (upper), 0.376 (middle), and 0.388 (lower). Black dashed curve: low-temperature behavior with ξ at upper bound of 0.383 from (*30*). Green solid circles (black fine dashed line): MIT experimental data (theory) for the ideal Fermi gas. Blue solid squares (blue curve): diagrammatic Monte Carlo calculation (*34*) for density (pressure, with blue dashed curves denoting the uncertainty bands). Solid green line: third-order Virial expansion. Open black squares: self-consistent T-matrix calculation (*23*). Open green circles: lattice calculation (*36*). Orange star and blue triangle: critical point from the Monte Carlo calculations (*26*) and (*27*), respectively. Solid diamonds: Ecole Normale Supérieure experiment (*12*). Purple open diamonds: Tokyo experiment (*11*).

Downloaded from www.sciencemag.org on February 6, 2012

the critical point, the density shows a strong variation, whereas the pressure, the integral of the density over μ at constant T, is naturally less sensitive to the superfluid transition.

In conclusion, we have performed thermodynamic measurements of the unitary Fermi gas across the superfluid phase transition at the level of uncertainty of a few percent, without any fits or input from theory, enabling validation of theories for strongly interacting matter. Similar unbiased methods can be applied to other systems, for example, two-dimensional Bose and Fermi gases or fermions in optical lattices.

References and Notes

1. M. Tinkham, *Introduction to Superconductivity* (Dover, Mineola, New York, ed. 2, 2004).
2. D. Vollhardt, P. Wölfle, *The Superfluid Phases of Helium 3* (Taylor & Francis, London, 1990).
3. J. A. Lipa, J. A. Nissen, D. A. Stricker, D. R. Swanson, T. C. P. Chui, *Phys. Rev. B* **68**, 174518 (2003).
4. M. W. Zwierlein, J. R. Abo-Shaeer, A. Schirotzek, C. H. Schunck, W. Ketterle, *Nature* **435**, 1047 (2005).
5. W. Ketterle, M. Zwierlein, *Riv. Nuovo Cim.* **31**, 247 (2008).
6. S. Giorgini, L. P. Pitaevskii, S. Stringari, *Rev. Mod. Phys.* **80**, 1215 (2008).
7. I. Bloch, J. Dalibard, W. Zwerger, *Rev. Mod. Phys.* **80**, 885 (2008).
8. J. Kinast *et al*., *Science* **307**, 1296 (2005).
9. J. T. Stewart, J. P. Gaebler, C. A. Regal, D. S. Jin, *Phys. Rev. Lett.* **97**, 220406 (2006).
10. L. Luo, B. Clancy, J. Joseph, J. Kinast, J. E. Thomas, *Phys. Rev. Lett.* **98**, 080402 (2007).
11. M. Horikoshi, S. Nakajima, M. Ueda, T. Mukaiyama, *Science* **327**, 442 (2010).
12. S. Nascimbène, N. Navon, K. J. Jiang, F. Chevy, C. Salomon, *Nature* **463**, 1057 (2010).
13. Materials and methods are available as supporting material on *Science* Online.
14. Y. Shin, M. W. Zwierlein, C. H. Schunck, A. Schirotzek, W. Ketterle, *Phys. Rev. Lett.* **97**, 030401 (2006).
15. G. B. Partridge *et al*., *Phys. Rev. Lett.* **97**, 190407 (2006).
16. C.-H. Cheng, S.-K. Yip, *Phys. Rev. B* **75**, 014526 (2007).
17. T.-L. Ho, *Phys. Rev. Lett.* **92**, 090402 (2004).
18. X.-J. Liu, H. Hu, P. D. Drummond, *Phys. Rev. Lett.* **102**, 160401 (2009).
19. D. Rakshit, K. M. Daily, D. Blume, Thermodynamics of two-component Fermi gas with large scattering length: Fourth- and higher-order virial coefficients, preprint arXiv:1106.5958; available at http://arxiv.org/abs/1106.5958.
20. J. R. Ensher, D. S. Jin, M. R. Matthews, C. E. Wieman, E. A. Cornell, *Phys. Rev. Lett.* **77**, 4984 (1996).
21. L. Luo, J. Thomas, *J. Low Temp. Phys.* **154**, 1 (2009).
22. L. Pollet, N. V. Prokof'ev, B. V. Svistunov, *Phys. Rev. Lett.* **104**, 245705 (2010).
23. R. Haussmann, W. Rantner, S. Cerrito, W. Zwerger, *Phys. Rev. A* **75**, 023610 (2007).
24. C. A. Regal, M. Greiner, D. S. Jin, *Phys. Rev. Lett.* **92**, 040403 (2004).
25. M. W. Zwierlein *et al*., *Phys. Rev. Lett.* **92**, 120403 (2004).
26. O. Goulko, M. Wingate, *Phys. Rev. A* **82**, 053621 (2010).
27. E. Burovski, N. Prokof'ev, B. Svistunov, M. Troyer, *Phys. Rev. Lett.* **96**, 160402 (2006).
28. J. P. Gaebler *et al*., *Nat. Phys.* **6**, 569 (2010).
29. Y. Castin, F. Werner, *The BCS-BEC Crossover and the Unitary Fermi Gas*, W. Zwerger, ed. (Springer-Verlag, Berlin, 2012), chap. 5.
30. M. M. Forbes, S. Gandolfi, A. Gezerlis, *Phys. Rev. Lett.* **106**, 235303 (2011).
31. P. Arnold, J. E. Drut, D. T. Son, *Phys. Rev. A* **75**, 043605 (2007).
32. J. Carlson, S.-Y. Chang, V. R. Pandharipande, K. E. Schmidt, *Phys. Rev. Lett.* **91**, 050401 (2003).
33. G. E. Astrakharchik, J. Boronat, J. Casulleras, A. S. Giorgini, *Phys. Rev. Lett.* **93**, 200404 (2004).
34. K. Van Houcke *et al*., Feynman diagrams versus Fermi-gas Feynman quantum emulator, preprint arXiv:1110.3747 (2011); available at http://arxiv.org/abs/1110.3747.
35. S. Nascimbène, Thermodynamics of ultracold Fermi gases, thesis, Ecole Normale Supérieure, Paris (2010).
36. A. Bulgac, J. E. Drut, P. Magierski, *Phys. Rev. Lett.* **96**, 090404 (2006).

Acknowledgments: We thank B. Svistunov, N. Prokof'ev, and F. Werner for fruitful discussions; Z. Hadzibabic for a critical reading of the manuscript; the authors of (*11*, *12*, *23*, *26*, *27*, *36*) for kindly providing us with their data; and André Schirotzek for help during the early stages of the experiment. M.J.H.K. acknowledges financial support from NSERC. This work was supported by the NSF, Air Force Office of Scientific Research (AFOSR) - Multidisciplinary Research Program of the University Research Initiative (MURI), Army Research Office (ARO) - MURI, Office of Naval Research, Defense Advanced Research Projects Agency (DARPA) Young Faculty Award, a grant from the ARO with funding from the DARPA Optical Lattice Emulator program, an AFOSR Presidential Early Career Award in Science and Engineering, the David and Lucile Packard Foundation, and the Alfred P. Sloan Foundation.

Supporting Online Material

www.sciencemag.org/cgi/content/full/science.1214987/DC1
Materials and Methods
Figs. S1 to S4
References (*37*–*45*)

7 October 2011; accepted 3 January 2012
Published online 12 January 2012;
10.1126/science.1214987

Iron Catalysts for Selective Anti-Markovnikov Alkene Hydrosilylation Using Tertiary Silanes

Aaron M. Tondreau,[1] Crisita Carmen Hojilla Atienza,[1] Keith J. Weller,[2] Susan A. Nye,[2] Kenrick M. Lewis,[3] Johannes G. P. Delis,[4] Paul J. Chirik[1]*

Alkene hydrosilylation, the addition of a silicon hydride (Si-H) across a carbon-carbon double bond, is one of the largest-scale industrial applications of homogeneous catalysis and is used in the commercial production of numerous consumer goods. For decades, precious metals, principally compounds of platinum and rhodium, have been used as catalysts for this reaction class. Despite their widespread application, limitations such as high and volatile catalyst costs and competing side reactions have persisted. Here, we report that well-characterized molecular iron coordination compounds promote the selective anti-Markovnikov addition of sterically hindered, tertiary silanes to alkenes under mild conditions. These Earth-abundant base-metal catalysts, coordinated by optimized bis(imino)pyridine ligands, show promise for industrial application.

Metal-catalyzed olefin hydrosilylation, which forms alkylsilanes by cleaving a silicon-hydrogen bond and adding the fragments across a carbon-carbon double bond (*1*, *2*), finds widespread application in the commercial manufacture of silicone-based surfactants, fluids, molding products, release coatings, and pressure-sensitive adhesives (*3*, *4*). Consequently, hydrosilylation has emerged as one of the largest-scale applications of homogeneous catalysis (*5*–*9*). For more than three decades, precious metal compounds with Pt, Pd, Ru, and Rh have been used almost exclusively as catalysts. Platinum compounds such as Karstedt's and Speier's catalysts, $Pt_2\{[(CH_2{=}CH)SiMe_2]_2O\}_3$ (Me, methyl) and $H_2PtCl_6{\cdot}6H_2O/^{i}PrOH$(^{i}Pr, isopropyl), respectively, are the most widely used industrial catalysts (*1*, *10*–*12*), though they suffer from chemical limitations such as intolerance to amino-substituted olefins and a tendency to catalyze competing isomerization of the terminal alkenes to internal isomers. Undesired isomerization often necessitates subsequent purification steps that are both energy and cost intensive. Furthermore, decomposition of the catalyst to colloidal platinum contributes to unwanted side reactions and also causes discoloration of the final products.

It has been estimated that the worldwide silicone industry consumed ~180,000 troy ounces (5.6 metric tons) of platinum in 2007 and most is not recovered (*13*). The high cost, coupled with the increasing demands on precious metals due to fuel-cell and other emerging technologies, has increased the volatility of the platinum market (*14*). The combination of chemical, economic, and political challenges inspires the exploration of inexpensive and Earth-abundant catalysts using iron, manganese, and cobalt (*15*). At the core of this challenge is suppressing tendencies of first-row transition metals toward one-electron redox processes in favor of the two-electron chemistry associated with the heavier metals that probably make up the fundamental steps in a catalytic cycle for alkene hydrosilylation.

[1]Department of Chemistry, Princeton University, Princeton, NJ 08544, USA. [2]Momentive Performance Materials, 260 Hudson River Road, Waterford, NY 12188, USA. [3]Momentive Performance Materials, 769 Old Saw Mill River Road, Tarrytown, NY 10591, USA. [4]Momentive Performance Materials bv, Plasticslaan 1, 4612PX Bergen op Zoom, Netherlands.

*To whom correspondence should be addressed. E-mail: pchirik@princeton.edu

Downloaded from www.sciencemag.org on February 6, 2012

PHYSICAL REVIEW A **85**, 051602(R) (2012)

Quantum degenerate Bose-Fermi mixture of chemically different atomic species with widely tunable interactions

Jee Woo Park,[1,2] Cheng-Hsun Wu,[1,2] Ibon Santiago,[1,2] Tobias G. Tiecke,[1,3] Sebastian Will,[1,2] Peyman Ahmadi,[1,2] and Martin W. Zwierlein[1,2]

[1]*MIT-Harvard Center for Ultracold Atoms, and Research Laboratory of Electronics, Massachusetts Institute of Technology, Cambridge, Massachusetts 02139, USA*

[2]*Department of Physics, Massachusetts Institute of Technology, Cambridge, Massachusetts 02139, USA*

[3]*Department of Physics, Harvard University, Cambridge, Massachusetts 02138, USA*

(Received 20 October 2011; published 9 May 2012)

We have created a quantum degenerate Bose-Fermi mixture of ^{23}Na and ^{40}K with widely tunable interactions via broad interspecies Feshbach resonances. Over 30 Feshbach resonances between ^{23}Na and ^{40}K were identified, including p-wave multiplet resonances. The large and negative triplet background scattering length between ^{23}Na and ^{40}K causes a sharp enhancement of the fermion density in the presence of a Bose condensate. As explained via the asymptotic bound-state model, this strong background scattering leads to wide Feshbach resonances observed at low magnetic fields. Our work opens up the prospect to create chemically stable, fermionic ground-state molecules of ^{23}Na-^{40}K, where strong, long-range dipolar interactions would set the dominant energy scale.

DOI: 10.1103/PhysRevA.85.051602 PACS number(s): 67.85.−d, 03.75.Ss, 34.50.−s, 37.10.De

Ultracold quantum gases realize paradigms of condensed-matter physics in pristine fashion, such as the superfluid to Mott insulator transition [1], the BEC-BCS crossover in fermionic superfluids [2,3], and the Berezinskii-Kosterlitz-Thouless transition in two-dimensional Bose gases [4]. A plethora of novel many-body systems may become accessible through the advent of quantum mixtures of different atomic species. In particular, Bose-Fermi mixtures with widely tunable interactions should reveal boson-mediated interactions between fermions and possibly boson-induced p-wave superfluidity [5,6]. The fate of impurities in a Fermi sea [7] or a Bose condensate [8–10] can be studied, and new quantum phases of matter are predicted in optical lattices [11]. Furthermore, the creation of fermionic ground-state molecules starting from a degenerate Bose-Fermi mixture opens up an intriguing avenue of research, as this results in a Fermi gas with long-range, anisotropic dipole-dipole interactions [12]. Since the first degenerate Bose-Fermi mixture of different atomic species, ^{23}Na and ^{6}Li [13], a variety of such systems has been realized [8,14–23]. However, so far only one mixture, ^{87}Rb-^{40}K, has allowed tunability of interspecies interactions with relative ease by means of a moderately wide ($\Delta B \approx 3$ G) Feshbach resonance [24], and only in this case fermionic Feshbach molecules have successfully been produced [25,26].

In this Rapid Communication, we report on the experimental realization of a unique Bose-Fermi mixture of ^{23}Na and ^{40}K and the observation of over 30 s- and p-wave Feshbach resonances at low magnetic fields. We demonstrate that ^{23}Na is an efficient coolant for sympathetic cooling of ^{40}K. A pattern of wide s-wave resonances exists for most of the energetically stable hyperfine combinations, the widest being located at 138 G with a width of about 30 G in the $^{23}\mathrm{Na}|F=1, m_F=1\rangle + {}^{40}\mathrm{K}|F=9/2, m_F=-5/2\rangle$ hyperfine configuration. We also observe p-wave multiplet resonances that are resolved thanks to their location at low magnetic fields.

In the singlet rovibrational ground state, the NaK molecule is known to have a large permanent electric dipole moment of 2.72(6) D [27,28], five times larger than that of KRb [12], and is predicted to be chemically stable against atom-atom exchange reactions [29], in contrast to KRb [30]. An ultracold gas of fermionic ground-state molecules of NaK will thus be an ideal system for the study of Fermi gases with strong, long-range dipolar interactions. Indeed, the interaction energy here can be expected to be on the order of the Fermi energy.

The experimental setup is based on the apparatus presented in Ref. [8], which employs two independent Zeeman slowers capable of simultaneously loading sodium and potassium atoms directly into a UHV chamber. The potassium slower

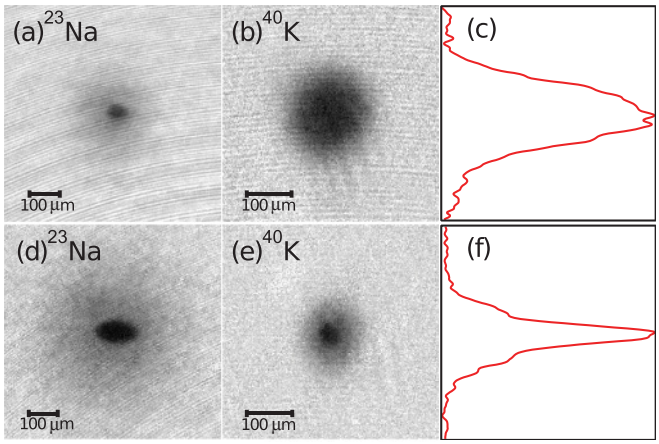

FIG. 1. (Color online) Simultaneous quantum degeneracy of ^{23}Na and ^{40}K atoms. (a) and (b), and (d) and (e) are pairs of time-of-flight (TOF) absorption images of a ^{23}Na BEC and a ^{40}K Fermi cloud with different atom number balance. A strong attractive interaction between the two species is observed in (e) as a sharp increase of the central density in the fermionic cloud in the presence of a Bose condensate. (c) and (f) are the center-sliced column density of the fermionic clouds of (b) and (e), respectively. TOF was (a) 11 ms, (b) 7 ms, (d) 17 ms, and (e) 5 ms. Atom numbers are (a) 2.4×10^5, (b) 2×10^5, (d) 8.2×10^5, and (e) 6.7×10^4.

 ©2012 American Physical Society

selectively decelerates the ^{40}K isotope, loading 10^7 atoms into a magneto-optical trap (MOT) in 10 s. For ^{23}Na, we use a dark spot MOT [31], which allows us to load approximately 10^9 atoms in 2 s.

Multispecies experiments can suffer from atom losses due to light-assisted collisions in the MOT and spin-changing collisions in the magnetic trap. In order to minimize such losses, we developed a shelving technique where ^{23}Na is first loaded into the MOT, optically pumped to the $|2,2\rangle$ stretched state, and captured in the magnetic trap. Next, the trap gradient is reduced to 7.7 G/cm to only support the stretched state of ^{23}Na against gravity. With this gradient left on, and the ^{23}Na thus "shelved in the dark" in a purely magnetic trap, finally the MOT and slower beams for ^{40}K are switched on to load the ^{40}K MOT. This scheme guarantees that only ^{23}Na atoms in the $|2,2\rangle$ state are present in the magnetic trap before loading ^{40}K, and it also potentially reduces light-assisted collisions that would be encountered in a double-species MOT.

Once both species are loaded into the optically plugged magnetic trap [8], the mixture is cooled for 7 s by rf-induced evaporation of ^{23}Na, where thermally excited ^{23}Na atoms in the $|2,2\rangle$ state are removed from the trap by coupling to the high-field seeking state of $|1,1\rangle$. We decompress the initial magnetic gradient of 220 G/cm to 27.5 G/cm at the end of evaporation to reduce three-body losses. The 5-μK cold mixture is then loaded into a crossed optical dipole trap (laser wavelength 1064 nm, maximum power 4.7 and 17 W, waist 73 and 135 μm).

At this stage, the $1/e$ lifetime of the mixture, with ^{23}Na and ^{40}K still in their stretched states, is about $\tau = 250$ ms, already signaling a strong attractive interaction increasing three-body losses and spin-changing dipolar losses. We thus immediately transfer ^{23}Na atoms into their hyperfine ground state $|1,1\rangle$ via a Landau-Zener sweep, and remove any remaining $|2,2\rangle$ atoms via a resonant light pulse. In the ^{23}Na$|1,1\rangle + ^{40}$K$|9/2,9/2\rangle$ state, the mixture now lives for $\tau = 20$ s. The gas is further evaporatively cooled in this spin mixture for 2 s by reducing the intensity of the dipole trap beams.

At the end of evaporation, a degenerate Fermi gas of ^{40}K with 2×10^5 atoms and $T/T_F = 0.6$ coexists with a Bose-Einstein condensate of ^{23}Na. Two sets of absorption images of the mixture for different values of ^{23}Na and ^{40}K atom numbers are shown in Fig. 1, where atom numbers are varied by changing the MOT loading times of the two species. The strong attractive interaction between ^{23}Na and ^{40}K in the ^{23}Na$|1,1\rangle + ^{40}$K$|9/2,9/2\rangle$ state is apparent. As the condensate grows, the fermionic cloud acquires a bimodal density distribution as it experiences the strong mean-field potential of the bosons [25]—see Fig. 1(e).

The evolution of the phase space densities (PSDs) and atom numbers N of both species during evaporation is shown in Fig. 2 . Temperature is determined by fitting a thermal profile to the wings of the ^{23}Na cloud. The cooling efficiency $\Gamma = -d\ln(\mathrm{PSD})/d\ln(N)$ for sodium in the magnetic trap is $\Gamma_{\mathrm{Na}} = 2.7$, a rather high value thanks to the steep confinement in the plugged trap. This efficiency is not affected by the presence of the relatively small admixture of ^{40}K. Sympathetic cooling is less efficient than in other mixtures [8,32] as ^{40}K is seen to be lost due to three-body collisions in the magnetic trap. We

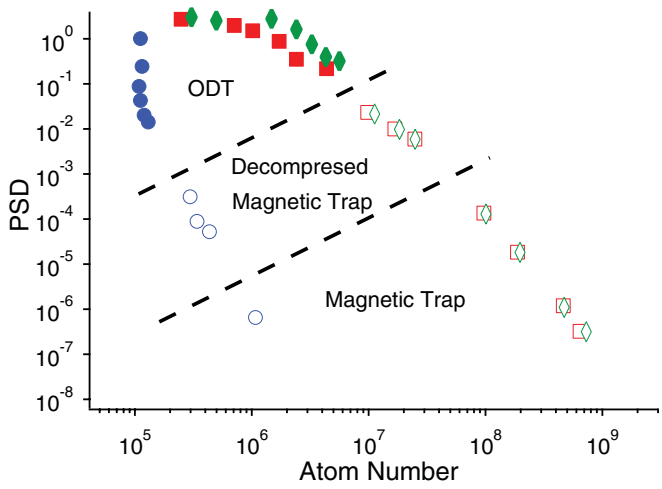

FIG. 2. (Color online) Evolution of the phase space density (PSD) with atom number (N). Blue circles: ^{40}K; red squares: ^{23}Na with ^{40}K; green diamonds: ^{23}Na alone. Open and solid symbols represent the PSD in the magnetic trap and optical trap, respectively.

find $\Gamma_{\mathrm{K}} = 4.6$ for ^{40}K. In the crossed optical dipole trap, with sodium in $|1,1\rangle$, the sodium cooling becomes less efficient due to the weaker confinement, $\Gamma_{\mathrm{Na}} = 0.9$, but the ^{40}K number is essentially conserved in this mixture so that sympathetic cooling is highly efficient, with $\Gamma_{\mathrm{K}} = 15.3$. The lowest T/T_F achieved for ^{40}K after evaporating all of ^{23}Na is $T/T_F = 0.35$ with 3×10^5 atoms.

With this degenerate Bose-Fermi mixture at our disposal, the natural next step is to search for interspecies Feshbach resonances between ^{23}Na and ^{40}K. There have been theoretical indications for resonances below 100 G [34]. In addition, a large and negative triplet scattering length was predicted in Ref. [35], a value that has recently been refined to $a_t = -575^{+191}_{-532}$ [34], indicating that the triplet potential has an almost bound, virtual state right above threshold. A large background scattering length is often a catalyst for wide Feshbach resonances [36], caused by strong coupling of molecular states to the almost resonant open channel. A famous example is the 300-G-wide Feshbach resonance in ^{6}Li [37].

We performed Feshbach loss spectroscopy, mapping out atom losses of both species as a function of magnetic field. Over 30 Feshbach resonances were observed in four different spin state combinations of ^{23}Na$|1,1\rangle + ^{40}$K$|9/2,m_F\rangle$, from the ground spin state $m_F = -9/2$ up to $m_F = -3/2$. Spin states of ^{40}K are prepared starting from $m_F = +9/2$ by a single Landau-Zener sweep through the intermediate m_F states at 15 G. The experimentally observed resonance positions and widths are reported in Table I. Many wide s-wave Feshbach resonances at low magnetic fields are identified, the widest one at 138 G for collisions between ^{23}Na$|1,1\rangle + ^{40}$K$|9/2,-5/2\rangle$, with a width of 30 G—see Fig. 3.

p-wave Feshbach resonances are known to split into a doublet structure due to different projections of the orbital angular momentum onto the magnetic field axis [38]. In the NaK system, however, we observe triplet features for many p-wave resonances—see Fig. 4. These originate from the magnetic dipole-dipole interaction of constituent atoms,

TABLE I. Data summary on the Feshbach resonances between ^{23}Na in $|1,1\rangle$ and ^{40}K in $|9/2,m_F\rangle$. The positions and widths of the resonances, $B_0^{\rm expt}$ and $\Delta B_{\rm expt}$, are determined by phenomenological Gaussian fits ($\propto e^{-(B-B_0^{\rm expt})^2/\Delta B_{\rm expt}^2}$) to the observed loss features. For p-wave resonances, we report the positions and widths of the resolved features, i.e., doublets and multiplets. $B_0^{\rm th}$ and $\Delta B_{\rm th}$ give the theoretical positions and widths from the ABM model.

Collision channel	$B_0^{\rm expt}$ (G)	$\Delta B_{\rm expt}$ (G)	$B_0^{\rm th}$ (G)	$\Delta B_{\rm th}$ (G)	Resonance type
^{23}Na$\|1,1\rangle + {}^{40}$K$\|9/2,-9/2\rangle$	6.35, 6.41, 6.47, 6.68	0.02	7.2		p
	19.12, 19.18, 19.27	0.02	18.3		p
	78.3	1.1	75.5	1.1	s
	88.2	4.3	84.5	5.4	s
^{23}Na$\|1,1\rangle + {}^{40}$K$\|9/2,-7/2\rangle$	7.32, 7.54	0.2, 0.03	8.7		p
	23.19, 23.29	0.05, 0.05	22.1		p
	81.6	0.2	82.1	0.04	s
	89.8	1.1	87.3	0.6	s
	108.6	6.6	105.7	13.1	s
^{23}Na$\|1,1\rangle + {}^{40}$K$\|9/2,-5/2\rangle$	9.23, 9.60	0.14, 0.11	11.0		p
	29.19, 29.45, 29.52	0.04	27.8		p
	96.5	0.5	97.2	0.04	s
	106.9	1.8	103.8	0.45	s
	148 (138[a])	37 (30[a])	137.1	26	s
^{23}Na$\|1,1\rangle + {}^{40}$K$\|9/2,-3/2\rangle$	12.51, 12.68	0.16, 0.06	14.8		p
	39.39, 39.86	0.15, 0.14	37.2		p
	116.9	0.5	118.3	0.07	s
	129.5	4.6	127.2	0.39	s
	175	20	187.8	50.5	s

[a]The resonance position and width have been refined by measuring the molecular binding energies via rf spectroscopy [33].

which couple molecular states with different total internal spin. The diagonal terms of the magnetic dipole-dipole interaction induce an energy shift that differs for the $m_l = 0$ and $|m_l| = 1$ quantum numbers, giving rise to the well-known doublet structures. The off-diagonal terms in the dipole-dipole interaction couple different values of m_l while conserving the total angular momentum $m_l + M_F$, where $M_F = m_{F,\rm K} + m_{F,\rm Na}$. These terms are in most mixtures negligible since molecular states with different values of M_F have to be nearly degenerate to result in a significant energy shift. However, due to the low-field nature of the NaK p-wave resonances, multiple molecular states are nearly degenerate with the open-channel spin state, allowing for the triplet structure to be resolved.

The assignment of s- and p-wave characters of the resonances follows from a simple, but powerful model of the molecular states involved. The singlet and triplet potentials of the interatomic potential allow for a variety of bound states. From the known scattering length [34] and the van der Waals coefficient C_6 [39], the weakest s-wave bound states are expected at about $E_s^s = -150(10)$ MHz and $E_t^s = -1625(50)$ MHz for the singlet and triplet s-wave potentials, where the errors reflect uncertainties of the scattering lengths from Ref. [34]. The p-wave bound states follow from the s-wave bound states as in Ref. [40] and are slightly adjusted to fit the observed resonance positions. As described in Refs. [41,42], as a first guess for locations of Feshbach resonances one can neglect the part of the hyperfine interaction that couples singlet and triplet bound states. This already provides the pattern of Feshbach resonances as positions where these (uncoupled) molecular states cross the atomic (open-channel) threshold. The analysis shows that the observed resonances are caused by the triplet bound states. Next, we use the asymptotic bound-state model (ABM) to include the singlet-triplet coupling of molecular states [43]. To couple the molecular states to the open channel, we follow Marcelis *et al.* [36] and only include the effect of the virtual state causing the large and negative triplet scattering length. The spin part of the coupling matrix element is obtained from the ABM Hamiltonian and the spatial part, i.e., the wave-function overlap between the respective bound state and the virtual state, is taken as one free fit parameter. For the background scattering length of the low-field resonances the effect of broad resonances is included. The virtual state causes strong coupling of several s-wave molecular states to the open channel, leading to wide, open-channel-dominated resonances as known from the case of ^{6}Li. The theoretical values obtained with this model are shown in Table I. An exceptionally broad resonance for $m_F = -3/2$ is predicted to be even wider and to be shifted further, possibly hinting at a shift between the loss maximum and the actual Feshbach resonance position. Our approach leads to a refined triplet bound-state energy of $E_t^s = -1654(3)$ MHz and $E_t^p = -1478(7)$ MHz, and using the long-range potential from Ref. [34], we obtain a refined value of the triplet scattering length of $a_t = -830(70)a_0$. The errors correspond to one standard deviation of a least-squares fit to the eight narrowest s-wave resonances that are least sensitive to the coupling to the scattering states and hence the error induced by the ABM is expected to be small [43].

In conclusion, we have produced a degenerate Bose-Fermi mixture of ^{23}Na and ^{40}K, and identified over 30 s- and

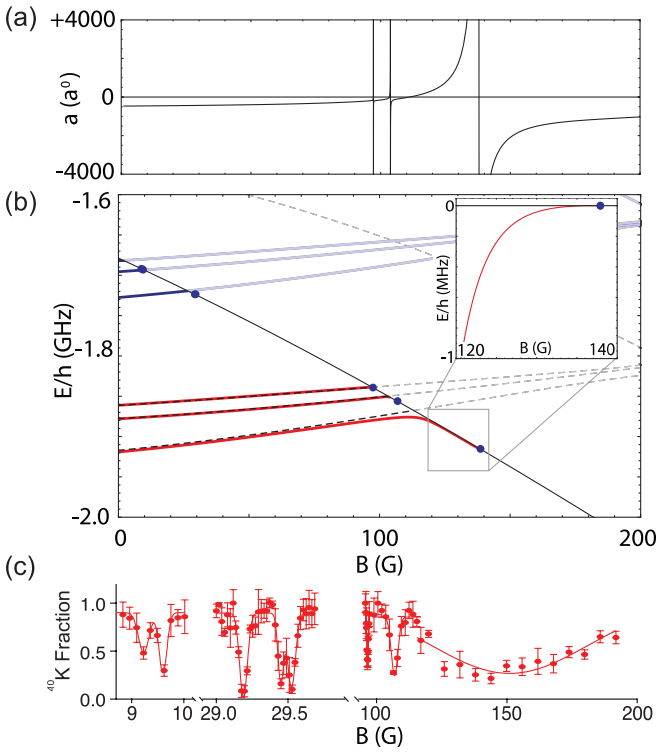

FIG. 3. (Color online) Feshbach resonances in ^{23}Na-^{40}K, here for $^{23}\mathrm{Na}|1,1\rangle + {}^{40}\mathrm{K}|9/2,-5/2\rangle$ collisions. (a) Scattering length from the ABM model. (b) Open-channel threshold energy (black solid line), uncoupled (s-wave: dashed lines; p-wave: light blue/light gray lines) and coupled molecular states (s-wave: red/gray solid lines; p-wave: blue/dark gray solid lines). The blue dots denote experimentally measured resonances. The inset shows the energy, relative to threshold, of the molecular state at the wide s-wave resonance at 138 G [33]. (c) Experimental loss spectra of ^{40}K in the presence of ^{23}Na. Three s-wave resonances and two p-wave manifolds are found, the latter resolved in one doublet and one triplet.

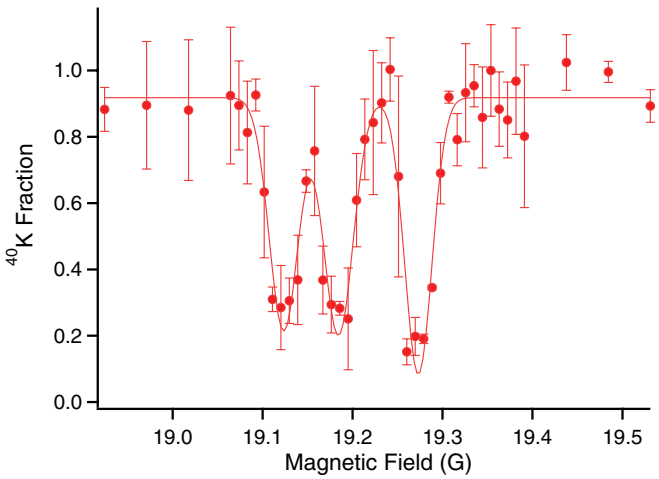

FIG. 4. (Color online) Triplet structure of the p-wave resonance at 19.1 G for the $^{23}\mathrm{Na}|1,1\rangle + {}^{40}\mathrm{K}|9/2,-9/2\rangle$ spin configuration. A phenomenological triple Gaussian fit is applied as a guide to the eyes.

p-wave interspecies Feshbach resonances, including several exceptionally broad resonances. Remarkably, many p-wave Feshbach resonances are observed to be triplets or even multiplets. Our strongly interacting ^{23}Na-^{40}K mixture near these Feshbach resonances should allow the study of Bose or Fermi polarons [7], of boson-mediated interactions between fermions, and possibly of unique states of matter in optical lattices. The formation of fermionic Feshbach molecules is within reach. In the rovibrational ground state, NaK molecules possess a large induced electric dipole moment and are stable against exchange reactions. One can thus hope to create a Fermi gas of polar molecules with strong dipole-dipole interactions that dominate the many-body physics of the gas, rather than being a small perturbative effect.

We thank Eberhard Tiemann for performing a coupled-channel calculation based on our results which stimulated us to further investigate the p-wave multiplet structures. We also thank Tout Wang for stimulating discussions. This work was supported by the NSF, AFOSR-MURI and -PECASE, ARO-MURI, ONR YIP, DARPA YFA, a grant from the Army Research Office with funding from the DARPA OLE program and the David and Lucille Packard Foundation.

[1] I. Bloch, J. Dalibard, and W. Zwerger, Rev. Mod. Phys. **80**, 885 (2008).

[2] *Ultracold Fermi Gases*, Proceedings of the International School of Physics "Enrico Fermi," Course CLXIV, Varenna, 2006, edited by M. Inguscio, W. Ketterle, and C. Salomon (IOS, Amsterdam, 2008).

[3] W. Ketterle and M. Zwierlein, Riv. Nuovo Cimento **31**, 247 (2008).

[4] Z. Hadzibabic and J. Dalibard, Riv. Nuovo Cimento **34**, 389 (2011).

[5] M. J. Bijlsma, B. A. Heringa, and H. T. C. Stoof, Phys. Rev. A **61**, 053601 (2000).

[6] H. Heiselberg, C. J. Pethick, H. Smith, and L. Viverit, Phys. Rev. Lett. **85**, 2418 (2000).

[7] A. Schirotzek, C.-H. Wu, A. Sommer, and M. W. Zwierlein, Phys. Rev. Lett. **102**, 230402 (2009).

[8] C.-H. Wu, I. Santiago, J. W. Park, P. Ahmadi, and M. W. Zwierlein, Phys. Rev. A **84**, 011601 (2011).

[9] E. Fratini and P. Pieri, Phys. Rev. A **81**, 051605 (2010).

[10] Z.-Q. Yu, S. Zhang, and H. Zhai, Phys. Rev. A **83**, 041603 (2011).

[11] M. Lewenstein, L. Santos, M. A. Baranov, and H. Fehrmann, Phys. Rev. Lett. **92**, 050401 (2004).

[12] K. K. Ni, S. Ospelkaus, M. H. G. de Miranda, A. Pe'er, B. Neyenhuis, J. J. Zirbel, S. Kotochigova, P. S. Julienne, D. S. Jin, and J. Ye, Science **322**, 231 (2008).

[13] Z. Hadzibabic, C. A. Stan, K. Dieckmann, S. Gupta, M. W. Zwierlein, A. Görlitz, and W. Ketterle, Phys. Rev. Lett. **88**, 160401 (2002).
[14] G. Roati, F. Riboli, G. Modugno, and M. Inguscio, Phys. Rev. Lett. **89**, 150403 (2002).
[15] J. Goldwin, S. Inouye, M. L. Olsen, B. Newman, B. D. DePaola, and D. S. Jin, Phys. Rev. A **70**, 021601 (2004).
[16] C. Ospelkaus, S. Ospelkaus, K. Sengstock, and K. Bongs, Phys. Rev. Lett. **96**, 020401 (2006).
[17] S. Aubin, M. H. T. Extavour, S. Myrskog, L. J. Leblanc, J. Estève, S. Singh, P. Scrutton, D. McKay, R. McKenzie, I. D. Leroux *et al.*, J. Low Temp. Phys. **140**, 377 (2005).
[18] K. Günter, T. Stöferle, H. Moritz, M. Köhl, and T. Esslinger, Phys. Rev. Lett. **96**, 180402 (2006).
[19] T. Best, S. Will, U. Schneider, L. Hackermüller, D. van Oosten, I. Bloch, and D. S. Lühmann, Phys. Rev. Lett. **102**, 030408 (2009).
[20] C. Silber, S. Günther, C. Marzok, B. Deh, P. W. Courteille, and C. Zimmermann, Phys. Rev. Lett. **95**, 170408 (2005).
[21] M. Taglieber, A. C. Voigt, T. Aoki, T. W. Hänsch, and K. Dieckmann, Phys. Rev. Lett. **100**, 010401 (2008).
[22] H. Hara, Y. Takasu, Y. Yamaoka, J. M. Doyle, and Y. Takahashi, Phys. Rev. Lett. **106**, 205304 (2011).
[23] A. H. Hansen, A. Khramov, W. H. Dowd, A. O. Jamison, V. V. Ivanov, and S. Gupta, Phys. Rev. A **84**, 011606 (2011).
[24] F. Ferlaino, C. D'Errico, G. Roati, M. Zaccanti, M. Inguscio, G. Modugno, and A. Simoni, Phys. Rev. A **73**, 040702 (2006).
[25] C. Ospelkaus, S. Ospelkaus, L. Humbert, P. Ernst, K. Sengstock, and K. Bongs, Phys. Rev. Lett. **97**, 120402 (2006).
[26] J. J. Zirbel, K. K. Ni, S. Ospelkaus, J. P. D'Incao, C. E. Wieman, J. Ye, and D. S. Jin, Phys. Rev. Lett. **100**, 143201 (2008).
[27] R. F. Wormsbecher, M. M. Hessel, and F. J. Lovas, J. Chem. Phys. **74**, 6983 (1981).
[28] A. Gerdes, O. Dulieu, H. Knöckel, and E. Tiemann, Eur. Phys. J. D **65**, 105 (2011).
[29] P. S. Zuchowski and J. M. Hutson, Phys. Rev. A **81**, 060703 (2010).
[30] S. Ospelkaus, K.-K. Ni, D. Wang, M. H. G. de Miranda, B. Neyenhuis, G. Qumner, P. S. Julienne, J. L. Bohn, D. S. Jin, and J. Ye, Science **327**, 853 (2006).
[31] W. Ketterle, K. B. Davis, M. A. Joffe, A. Martin, and D. E. Pritchard, Phys. Rev. Lett. **70**, 2253 (1993).
[32] Z. Hadzibabic, S. Gupta, C. A. Stan, C. H. Schunck, M. W. Zwierlein, K. Dieckmann, and W. Ketterle, Phys. Rev. Lett. **91**, 160401 (2003).
[33] C.-H. Wu *et al.* (unpublished).
[34] A. Gerdes, M. Hobein, H. Knöckel, and E. Tiemann, Eur. Phys. J. D **49**, 67 (2008).
[35] V. Venturi, M. Jamieson, and R. Côté, J. Phys. B **34**, 4339 (2001).
[36] B. Marcelis, E. G. M. van Kempen, B. J. Verhaar, and S. J. J. M. F. Kokkelmans, Phys. Rev. A **70**, 012701 (2004).
[37] K. Dieckmann, C. A. Stan, S. Gupta, Z. Hadzibabic, C. H. Schunck, and W. Ketterle, Phys. Rev. Lett. **89**, 203201 (2002).
[38] C. Ticknor, C. A. Regal, D. S. Jin, and J. L. Bohn, Phys. Rev. A **69**, 042712 (2004).
[39] A. Derevianko, J. F. Babb, and A. Dalgarno, Phys. Rev. A **63**, 052704 (2001).
[40] T. G. Tiecke, M. R. Goosen, J. T. M. Walraven, and S. J. J. M. F. Kokkelmans, Phys. Rev. A **82**, 042712 (2010).
[41] A. J. Moerdijk, B. J. Verhaar, and A. Axelsson, Phys. Rev. A **51**, 4852 (1995).
[42] C. A. Stan, M. W. Zwierlein, C. H. Schunck, S. M. F. Raupach, and W. Ketterle, Phys. Rev. Lett. **93**, 143001 (2004).
[43] E. Wille, F. M. Spiegelhalder, G. Kerner, D. Naik, A. Trenkwalder, G. Hendl, F. Schreck, R. Grimm, T. G. Tiecke, J. T. M. Walraven, S. J. J. M. F. Kokkelmans, E. Tiesinga, and P. S. Julienne, Phys. Rev. Lett. **100**, 053201 (2008).

Evolution of Fermion Pairing from Three to Two Dimensions

Ariel T. Sommer, Lawrence W. Cheuk, Mark J. H. Ku, Waseem S. Bakr, and Martin W. Zwierlein

Department of Physics, MIT-Harvard Center for Ultracold Atoms, and Research Laboratory of Electronics, MIT, Cambridge, Massachusetts 02139, USA

(Received 13 October 2011; published 23 January 2012)

We follow the evolution of fermion pairing in the dimensional crossover from three-dimensional to two-dimensional as a strongly interacting Fermi gas of ^{6}Li atoms becomes confined to a stack of two-dimensional layers formed by a one-dimensional optical lattice. Decreasing the dimensionality leads to the opening of a gap in radio-frequency spectra, even on the Bardeen-Cooper-Schrieffer side of a Feshbach resonance. The measured binding energy of fermion pairs closely follows the theoretical two-body binding energy and, in the two-dimensional limit, the zero-temperature mean-field Bose-Einstein-condensation to Bardeen-Cooper-Schrieffer crossover theory.

DOI: 10.1103/PhysRevLett.108.045302 PACS numbers: 67.85.−d, 03.75.Lm, 05.30.Fk, 32.30.Bv

Interacting fermions in coupled two-dimensional (2D) layers present unique physical phenomena and are central to the description of unconventional superconductivity in high-transition-temperature cuprates [1] and layered organic conductors [2]. Experiments on ultracold gases of fermionic atoms have allowed access to the crossover from Bose-Einstein condensation (BEC) of tightly bound fermion pairs to Bardeen-Cooper-Schrieffer (BCS) superfluidity of long-range Cooper pairs in three spatial dimensions [3,4] and, more recently, the confinement of interacting Fermi gases to two spatial dimensions [5–9]. A fermionic superfluid loaded into a periodic potential should form stacks of two-dimensional superfluids with tunable interlayer coupling [10–13], an ideal model for Josephson-coupled quasi-2D superconductors [1,14]. For deep potentials in the regime of uncoupled 2D layers, increasing the temperature of the gas is expected to destroy superfluidity through the Berezinskii-Kosterlitz-Thouless mechanism [15–17], while more exotic multiplane vortex loop excitations are predicted for a three-dimensional (3D) anisotropic BCS superfluid near the critical point [18].

In this Letter, we study fermion pairing across the crossover from 3D to 2D in a periodic potential of increasing depth. To form a bound state in 3D, the attraction between two particles in a vacuum must exceed a certain threshold. However, if the two particles interact in the presence of a Fermi sea, the Cooper mechanism allows pairing for arbitrarily weak interactions [19]. In 2D, even two particles in a vacuum can bind for arbitrarily weak interactions. Surprisingly, the mean-field theory of the BEC-BCS crossover in 2D predicts that the binding energy of fermion pairs in the many-body system is identical to the two-body binding energy E_b [20]. Indeed, to break a pair and remove one pairing partner from the system costs an energy [21] $E_{b,\mathrm{MF}} = \sqrt{\mu^2 + \Delta^2} - \mu$ within mean-field theory, where μ is the chemical potential and Δ is the pairing gap. In 2D, one finds [20] $\mu = E_F - E_b/2$ and $\Delta^2 = 2E_F E_b$, where E_F is the Fermi energy, and thus $E_{b,\mathrm{MF}} = E_b$; i.e., the many-body and two-body binding energies are predicted to be identical throughout the BEC-BCS crossover.

We realize a system that is tunable from 3D to 2D with a gas of ultracold fermionic ^{6}Li atoms trapped in an optical trap and a standing-wave optical lattice. The lattice produces a periodic potential along the z direction,

$$V(z) = V_0 \sin^2(\pi z/d), \tag{1}$$

with depth V_0 and lattice spacing $d = 532$ nm. Together with the optical trap, the lattice interpolates between the 3D and 2D limits. It gradually freezes out motion along one dimension and confines particles in increasingly uncoupled layers. Features characteristic of the 2D system appear as the strength of the periodic potential is increased. The threshold for pairing is reduced, allowing pairs to form for weaker attractive interactions than in the 3D system. The effective mass of particles increases along the confined direction, and the center of mass and relative degrees of freedom of an atom pair become coupled [11]. For a deep potential that suppresses interlayer tunneling, the system is an array of uncoupled two-dimensional layers. Here, the center of mass and relative motion decouple and fermion pairs form for the weakest interatomic attraction [11,22,23].

In the experiment, the appearance of bound fermion pairs is revealed using radio-frequency (rf) spectroscopy. The atomic gas consists of an equal mixture of ^{6}Li atoms in the first and third hyperfine states (denoted as $|1\rangle$ and $|3\rangle$), chosen to minimize final-state interaction effects in the rf spectra [24]. Interactions between atoms in states $|1\rangle$ and $|3\rangle$ are greatly enhanced by a broad Feshbach resonance at 690.4(5) G [25]. An rf pulse is applied to transfer atoms from one of the initial hyperfine states to the unoccupied second hyperfine state (denoted as $|2\rangle$). In previous work on rf spectroscopy of ^{40}K fermions in a deep one-dimensional (1D) lattice [8], an rf pulse transferred atoms from an initially weakly interacting state into a strongly interacting spin state, likely producing polarons [26]. In

 © 2012 American Physical Society

our Letter, the initial state is the strongly interacting, largely paired Fermi gas in equilibrium, and the final state is weakly interacting.

An asymmetric dissociation peak (the bound-to-free transition) in the rf spectrum indicates the presence of fermion pairs. For two-particle binding, the pair dissociation line shape in the 3D and 2D limits is proportional to $\rho(h\nu - E_b)/\nu^2$, with ρ the free-particle density of states and $\nu = \pm(\nu_{\rm rf} - \nu_{\rm hf})$ the offset of the rf frequency $\nu_{\rm rf}$ from the hyperfine splitting $\nu_{\rm hf}$ (plus symbol: $|1\rangle \rightarrow |2\rangle$ transition; minus symbol: $|3\rangle \rightarrow |2\rangle$ transition). This form can be obtained from Fermi's golden rule and the bound-state wave function in momentum space; see also Refs. [21,27]. In 2D, the expected dissociation line shape is then proportional to

$$I(\nu) \propto \frac{\theta(h\nu - E_b)}{\nu^2}. \quad (2)$$

In addition to the pairing peak, at finite temperature one expects a peak in the rf spectrum due to unbound atoms (the free-to-free transition). A narrow bound-to-bound transition can also be driven at an offset frequency $\nu_{bb} = (E_b - E_b')/h$ that transfers one spin state of the initial bound pair with binding energy E_b into a bound state of $|2\rangle$ with $|1\rangle$ or $|3\rangle$, of binding energy E_b'. For a $|1\rangle - |3\rangle$ mixture near the Feshbach resonance, $E_b \ll E_b'$ [24], so the bound-to-bound peak is well-separated from the bound-to-free and free-to-free peaks. As very recently calculated [28], final-state interactions and the anomalous nature of scattering in 2D introduce an additional factor of $\frac{\ln^2(E_b/E_b')}{\ln^2[(h\nu - E_b)/E_b'] + \pi^2}$ into Eq. (2), causing a rounding off of the sharp peak expected from the step function.

In a 1D lattice, the binding energy for two-body pairs is determined by the lattice spacing d, the depth V_0, and the 3D scattering length a. In the 2D limit $V_0 \gg E_R$, with recoil energy $E_R = \frac{\hbar^2\pi^2}{2md^2}$, the scattering properties of the gas are completely determined by E_b [22,23]. In that limit, the lattice wells can be approximated as harmonic traps with level spacing $\hbar\omega_z = 2\sqrt{V_0 E_R}$ and harmonic oscillator length $l_z = \sqrt{\frac{\hbar}{m\omega_z}}$. In a many-particle system in 2D, the ratio of the binding energy to the Fermi energy determines the strength of interactions. The 2D scattering amplitude $f(E_F) = \frac{2\pi}{-\ln(k_F a_{\rm 2D}) + i\pi/2}$ for collisions with energy E_F is parametrized by $\ln(k_F a_{\rm 2D})$, where $k_F = \sqrt{2mE_F}/\hbar$ and $a_{\rm 2D} = \hbar/\sqrt{mE_b}$. It is large when $|\ln(k_F a_{\rm 2D})| \lesssim 1$ [22,23], corresponding to the strong-coupling regime [28,29]. The BEC side of the BEC-BCS crossover corresponds to negative values of $\ln(k_F a_{\rm 2D})$, while the BCS side corresponds to positive values [20].

The experimental sequence proceeds as follows. An ultracold gas of ^{6}Li is produced by sympathetic cooling with ^{23}Na as described previously [21]. The ^{6}Li atoms are transferred from a magnetic trap to an optical dipole trap (wavelength 1064 nm, waist 120 μm), with axial harmonic confinement (frequency 22.8 Hz) provided by magnetic field curvature. With ^{6}Li polarized in state $|1\rangle$, the magnetic bias field is raised to 568 G, and an equal mixture of hyperfine states $|1\rangle$ and $|3\rangle$ is created using a 50% rf transfer from $|1\rangle$ to $|2\rangle$ followed by a full transfer from $|2\rangle$ to $|3\rangle$. The field is then raised to the final value, and evaporative cooling is applied by lowering the depth of the optical dipole trap, resulting in a fermion pair condensate with typically 5×10^5 atoms per spin state. The lattice is then ramped up over 100 ms. The retro-reflected lattice beam (wavelength 1064 nm) is at an angle of 0.5 degrees from the optical dipole trap beam, enough to selectively reflect only the lattice beam. The depth of the lattice is calibrated using Kapitza-Dirac diffraction of a ^{23}Na BEC and a ^{6}Li$_2$ molecular BEC and by lattice modulation spectroscopy on the ^{6}Li cloud. The magnetic field and hyperfine splitting are calibrated using rf spectroscopy on spin-polarized clouds. After loading the lattice, the rf pulse is applied for a duration of typically 1 ms. Images of state $|2\rangle$ and either $|1\rangle$ or $|3\rangle$ are recorded in each run of the experiment.

To ensure loading into the first Bloch band, the Fermi energy and temperature of the cloud are kept below the second band. The 2D Fermi energy $E_F^{\rm 2D} = \frac{2\pi\hbar^2 n}{m}$, with n the 2D density per spin state, is typically $h \times 10$ kHz. The bottom of the second band is at least one recoil energy $E_R = h \times 29.3$ kHz above the bottom of the first band in shallow lattices and up to about $h \times 300$ kHz for the deepest lattices. The temperature is estimated to be on the order of the Fermi energy.

rf spectra are recorded for various lattice depths and interaction strengths. Figure 1 shows examples of spectra over a range of lattice depths at the 3D Feshbach resonance and on the BCS side of the resonance at 721 G, where fermion pairing in 3D is a purely many-body effect. At the lowest lattice depths, the spectra show only a single peak, shifted to positive offset frequencies due to many-body interactions. This is similar to the case without a lattice [24,30]; to discern a peak due to fermion pairs from a peak due to unbound atoms would require locally resolved rf spectroscopy of imbalanced Fermi gases [30]. However, as the lattice depth is raised, the single peak splits into two and a clear pairing gap emerges. The narrow peak at zero offset is the free-to-free transition, and the asymmetric peak at positive offset is the pair dissociation spectrum. The pair spectrum, especially on resonance, shows a sharp threshold and a long tail corresponding to dissociation of fermion pairs into free atoms with nonzero kinetic energy.

Binding energies are determined from the offset frequency of the pairing threshold. Although the line shape in Eq. (2) jumps discontinuously from zero to its maximum value, the spectra are observed to be broadened. This is to a large part due to the logarithmic corrections [28] noted above, which predict a gradual rise at the threshold $h\nu = E_b$, and a spectral peak that is slightly shifted from

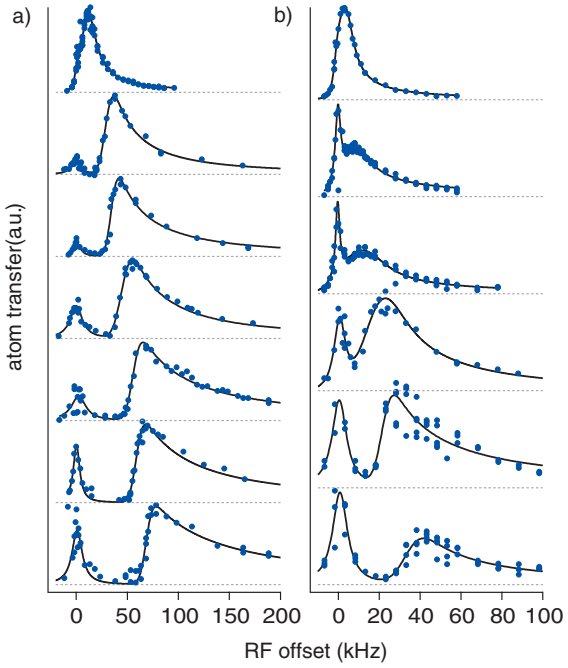

FIG. 1 (color online). Evolution of fermion pairing in the 3D-to-2D crossover in a one-dimensional optical lattice, observed via rf spectroscopy. Shown is the transferred atom number versus rf offset frequency relative to the atomic hyperfine splitting. (a) Spectra at the Feshbach resonance at 690.7(1) G with $d/a = -0.01(4)$. Lattice depths from top to bottom in units of E_R: 1.84(3), 4.8(2), 6.1(2), 9.9(4), 12.2(4), 18.6(7), and 19.5 (7). (b) Spectra on the BCS side at 720.7(1) G, $d/a = -1.15(2)$. Lattice depths in units of E_R: 2.75(5), 4.13(7), 4.8(1), 6.0(2), 10.3 (2), and 18.1(4).

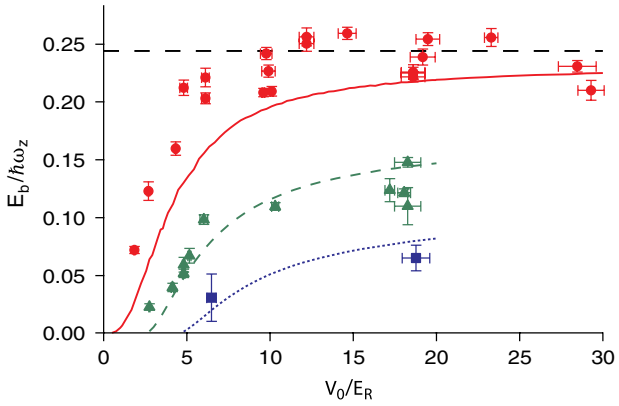

FIG. 2 (color online). Binding energy E_b versus lattice depth V_0 at several values of the 3D scattering length a. E_b is normalized via the lattice frequency ω_z. Red circles: results from spectra at 690.7(1) G and $d/a = -0.01(4)$. Green triangles: 720.7(1) G, $d/a = -1.15(2)$. Blue squares: 800.1(1) G, $d/a = -2.69(1)$. Curves show predictions from Orso *et al.* [11]. Horizontal black dashed line: harmonic approximation result for $1/a = 0$.

E_b. We include possible additional broadening by convolving the theoretical line shape, including the logarithmic correction, with a Gaussian function of width w_m. The parameters E_b and w_m are determined by a least-squares fit to the measured spectrum. Typical spectra have w_m of 5 kHz, consistent with our estimates of broadening based on collisions and three-body losses. The Fourier broadening is 1 kHz. Power broadening is about 5 kHz on the free-to-free transition and less than 1 kHz on the bound-to-free transition due to the reduced wave function overlap. Inclusion of the logarithmic correction is found to be necessary in order for the fit function to reproduce the observed behavior of the high-frequency tail. The final-state binding energy used in the logarithmic correction for fitting is obtained from spectra where both a bound-to-bound and a bound-to-free peak were measured. At low lattice depths, the 2D form for the paired spectrum should differ from the exact shape that interpolates between the 3D and 2D limits. In the case where the shape of the spectrum is given by the 3D limit, fitting to the 2D form overestimates the binding energy by 8%.

Figure 2 shows the measured binding energies as function of V_0/E_R for several interaction strengths. The binding energies are normalized by $\hbar\omega_z \equiv 2\sqrt{V_0 E_R}$, which equals the level spacing in the harmonic approximation to the lattice potential. The measured binding energies grow with increasing lattice depth and agree reasonably well with theoretical predictions for two-body bound pairs in a 1D lattice [11]. The binding energy at the 3D resonance approaches a constant multiple of $\hbar\omega_z$ as the lattice depth increases, as expected from the 2D limit [22,23]. Figure 3(a) compares the binding energies measured in lattices deeper than $17E_R$ to predictions in the harmonic quasi-2D limit [22,23]. At the 3D Feshbach resonance, we find $E_b = 0.232(16)\hbar\omega_z$ for deep lattices. The error bar refers to the standard error on the mean. This value is close to the harmonic confinement result of $0.244\hbar\omega_z$ [23]. The exact calculation [11] predicts a constant downward shift of the binding energy by $0.2E_R$ for deep lattices due to the anharmonicity of the sinusoidal potential. For V_0 of about $20E_R$, this gives a prediction of $0.22\hbar\omega_z$, also close to the measured value.

Figure 3(b) shows the binding energy measured in deep lattices normalized by the exact two-body result [11] versus the many-body interaction parameter $\ln(k_F a_{2D})$. Overall, the binding energies are close to the two-body value, even in the strong-coupling regime for $|\ln(k_F a_{2D})| < 1$, as predicted by zero-temperature mean-field theory [20]. The data show a slight downward deviation for the strongest coupling. At fixed reduced temperature T/T_F, the relationship should be universal. It will thus be interesting to see in future work whether the binding energy depends significantly on temperature.

The bound-to-bound transition is seen in Fig. 4 as a narrow peak at negative offset frequencies. In the regime where E_b can be found from the pair dissociation spectrum,

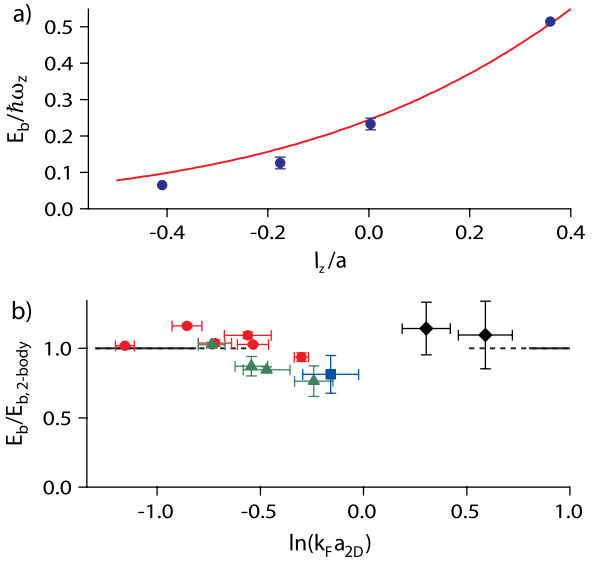

FIG. 3 (color online). (a) Binding energy of fermion pairs versus interaction strength l_z/a for deep lattices ($V_0 > 17E_R$). Solid curve: theoretical prediction in the 2D harmonic limit [22,23]. (b) Ratio of the measured binding energy to the two-body result [11] versus $\ln(k_F a_{2D})$ for $V_0 > 17E_R$. Black diamonds: binding energy determined from the bound-to-bound transition with resonant final-state interactions. Other data symbols: see Fig. 2. Horizontal line: zero-temperature mean-field theory [20].

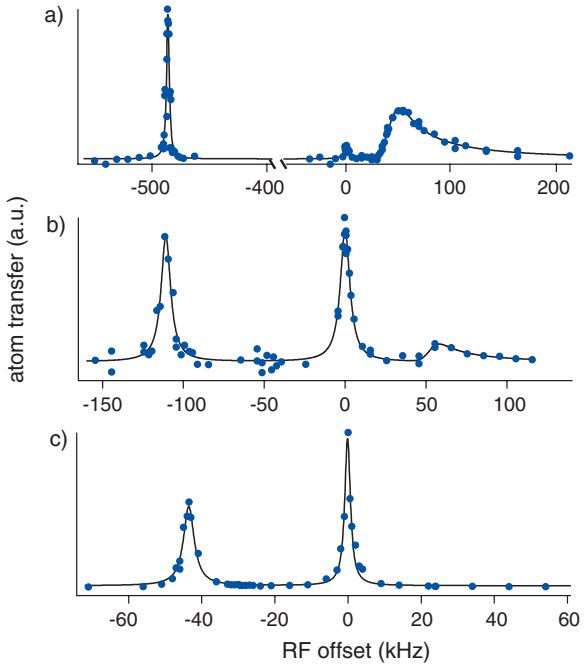

FIG. 4 (color online). Spectra including the bound-to-bound transition, a narrow peak at negative rf offset. Shown are spectra at magnetic fields of (a) 690.7(1) G, (b) 751.1(1) G, and (c) 834.4(1). The interaction parameters d/a are (a) $-0.01(4)$, (b) $-1.91(1)$, and (c) $-3.06(1)$. Lattice depths in units of E_R are (a) 9.59(7), (b) 26.1(4), and (c) 26.4(3). The bound-to-free transition is not visible in (c). The transfer is from $|1\rangle$ to $|2\rangle$ in (a) and (b) and from $|3\rangle$ to $|2\rangle$ in (c).

the bound-to-bound peak position directly yields the binding energy in the final state E_b'. For example, the spectrum in Fig. 4(a), taken at the 3D $|1\rangle - |3\rangle$ resonance at 690.7(1) G and $V_0/E_R = 9.59(7)$, gives $E_b'/E_R = 18.0(1)$ at a final-state interaction of $d/a' = 8.41(2)$. Likewise, the spectrum in Fig. 4(b) at $V_0/E_R = 26.1(4)$ and a magnetic field of 751.1(1) G, where $d/a' = 2.55(1)$, gives $E_b'/E_R = 5.3(1)$. An independent measurement for $d/a = 2.55(2)$ using the bound-to-free spectrum at 653.55 G yields $E_b/E_R = 5.25(2)$, showing that bound-to-bound transitions correctly indicate binding energies.

The BCS side of the 2D BEC-BCS crossover is reached in Fig. 4(c) by increasing the number of atoms to increase E_F and increasing the magnetic field to reach a lower binding energy. In Fig. 4(c), the central Fermi energy is $h \times 43(6)$ kHz and $T/T_F = 0.5(2)$. The magnetic field is set to 834.4(1) G, where $d/a = -3.06(1)$, and the final-state interactions between $|1\rangle$ and $|2\rangle$ are resonant, with $d/a' = -0.01(3)$. The lattice depth is $V_0/E_R = 26.4(3)$. Thus, we know that $E_b' = 0.232(16)\hbar\omega_z = 2.4(2)E_R$ at this lattice depth. From the bound-to-bound transition in Fig. 4(c), we can then directly determine the binding energy of $|1\rangle - |3\rangle$ fermion pairs to be $E_b/E_R = 0.9(2)$. The theoretical prediction [11] for two-body binding gives $E_b/E_R = 0.82(1)$. The measured binding energy gives a many-body interaction parameter of $\ln(k_F a_{2D}) = 0.6(1)$, on the BCS side but within the strongly interacting regime, where one expects many-body effects beyond mean-field BEC-BCS theory [26,29]. It is therefore interesting that the measured binding energy is close to the expected two-body binding energy to much better than the Fermi energy, as predicted by mean-field theory [20].

In conclusion, we have measured the binding energy of fermion pairs along the crossover from 3D to 2D in a one-dimensional optical lattice. Measurements were performed at several lattice depths and scattering lengths, allowing quantitative comparison with theoretical predictions. Considering the fact that the gas is a strongly interacting many-body system, the close agreement with two-body theory is surprising, especially in the strong-coupling regime. While mean-field BEC-BCS theory in 2D predicts this behavior [20], it misses other important features of the many-body system, most strikingly the interaction between fermion pairs [13]. Superfluidity in a one-dimensional lattice will be an exciting topic for future studies. Stacks of weakly coupled, superfluid 2D layers would constitute a basic model of the geometry found in high-temperature superconductors.

The authors would like to thank G. Orso for providing his code to calculate binding energies and M. Köhl and W. Zwerger for stimulating discussions. This work was supported by the NSF, AFOSR-MURI, ARO-MURI, ONR, DARPA YFA, a grant from the Army Research Office with

funding from the DARPA OLE program, the David and Lucile Packard Foundation, and the Alfred P. Sloan Foundation.

[1] M. Tinkham, *Introduction to Superconductivity* (Dover, Mineola, NY, 2004), 2nd ed., p. 318.
[2] J. Singleton and C. Mielke, Contemp. Phys. **43**, 63 (2002).
[3] *Ultracold Fermi Gases*, Proceedings of the International School of Physics "Enrico Fermi," Course CLXIV, edited by M. Inguscio, W. Ketterle, and C. Salomon (Elsevier, Amsterdam, 2008).
[4] S. Giorgini, L. P. Pitaevskii, and S. Stringari, Rev. Mod. Phys. **80**, 1215 (2008).
[5] K. Günter, T. Stöferle, H. Moritz, M. Köhl, and T. Esslinger, Phys. Rev. Lett. **95**, 230401 (2005).
[6] X. Du, Y. Zhang, and J. E. Thomas, Phys. Rev. Lett. **102**, 250402 (2009).
[7] K. Martiyanov, V. Makhalov, and A. Turlapov, Phys. Rev. Lett. **105**, 030404 (2010).
[8] B. Fröhlich, M. Feld, E. Vogt, M. Koschorreck, W. Zwerger, and M. Köhl, Phys. Rev. Lett. **106**, 105301 (2011).
[9] P. Dyke, E. D. Kuhnle, S. Whitlock, H. Hu, M. Mark, S. Hoinka, M. Lingham, P. Hannaford, and C. J. Vale, Phys. Rev. Lett. **106**, 105304 (2011).
[10] G. Orso and G. V. Shlyapnikov, Phys. Rev. Lett. **95**, 260402 (2005).
[11] G. Orso, L. P. Pitaevskii, S. Stringari, and M. Wouters, Phys. Rev. Lett. **95**, 060402 (2005).
[12] L. Salasnich, Phys. Rev. A **76**, 015601 (2007).
[13] W. Zhang, G.-D. Lin, and L.-M. Duan, Phys. Rev. A **77**, 063613 (2008).
[14] S. T. Ruggiero, T. W. Barbee, and M. R. Beasley, Phys. Rev. Lett. **45**, 1299 (1980).
[15] J. M. Kosterlitz and D. Thouless, J. Phys. C **5**, L124 (1972).
[16] D. S. Petrov, M. A. Baranov, and G. V. Shlyapnikov, Phys. Rev. A **67**, 031601 (2003).
[17] W. Zhang, G.-D. Lin, and L.-M. Duan, Phys. Rev. A **78**, 043617 (2008).
[18] M. Iskin and C. A. R. Sá de Melo, Phys. Rev. Lett. **103**, 165301 (2009).
[19] L. N. Cooper, Phys. Rev. **104**, 1189 (1956).
[20] M. Randeria, J.-M. Duan, and L. Y. Shieh, Phys. Rev. Lett. **62**, 981 (1989).
[21] W. Ketterle and M. Zwierlein, Riv. Nuovo Cimento Soc. Ital. Fis. **31**, 247 (2008).
[22] D. S. Petrov and G. V. Shlyapnikov, Phys. Rev. A **64**, 012706 (2001).
[23] I. Bloch, J. Dalibard, and W. Zwerger, Rev. Mod. Phys. **80**, 885 (2008).
[24] C. Schunck, Y. Shin, A. Schirotzek, and W. Ketterle, Nature (London) **454**, 739 (2008).
[25] M. Bartenstein, A. Altmeyer, S. Riedl, R. Geursen, S. Jochim, C. Chin, J. H. Denschlag, R. Grimm, A. Simoni, E. Tiesinga, C. J. Williams, and P. S. Julienne, Phys. Rev. Lett. **94**, 103201 (2005).
[26] V. Pietila, D. Pekker, Y. Nishida, and E. Demler, arXiv:1110.0494.
[27] C. Chin and P. S. Julienne, Phys. Rev. A **71**, 012713 (2005).
[28] C. Langmack, M. Barth, W. Zwerger, and E. Braaten, arXiv:1111.0999.
[29] G. Bertaina and S. Giorgini, Phys. Rev. Lett. **106**, 110403 (2011).
[30] A. Schirotzek, Y.-i. Shin, C. H. Schunck, and W. Ketterle, Phys. Rev. Lett. **101**, 140403 (2008).

LETTERS
PUBLISHED ONLINE: 18 MARCH 2012 | DOI: 10.1038/NPHYS2273
nature physics

Feynman diagrams versus Fermi-gas Feynman emulator

K. Van Houcke[1,2]*, F. Werner[1,3], E. Kozik[4,5], N. Prokof'ev[1,6], B. Svistunov[1,6], M. J. H. Ku[7], A. T. Sommer[7], L. W. Cheuk[7], A. Schirotzek[8] and M. W. Zwierlein[7]

Precise understanding of strongly interacting fermions, from electrons in modern materials to nuclear matter, presents a major goal in modern physics. However, the theoretical description of interacting Fermi systems is usually plagued by the intricate quantum statistics at play. Here we present a cross-validation between a new theoretical approach, bold diagrammatic Monte Carlo[1–3], and precision experiments on ultracold atoms. Specifically, we compute and measure, with unprecedented precision, the normal-state equation of state of the unitary gas, a prototypical example of a strongly correlated fermionic system[4–6]. Excellent agreement demonstrates that a series of Feynman diagrams can be controllably resummed in a non-perturbative regime using bold diagrammatic Monte Carlo.

In his seminal 1981 lecture[7], Richard Feynman argued that an arbitrary quantum system cannot be efficiently simulated with a classical universal computer, because generally, quantum statistics can only be imitated with a classical theory if probabilities are replaced with negative (or complex) weighting factors. For the majority of many-particle models this indeed leads to the so-called sign problem, which has remained an insurmountable obstacle. According to Feynman, the only way out is to employ computers made out of quantum-mechanical elements[7]. The recent experimental breakthroughs in cooling, probing and controlling strongly interacting quantum gases prompted a challenging effort to use this new form of quantum matter to realize Feynman's emulators of fundamental microscopic models[7,8]. Somewhat ironically, Feynman's arguments, which led him to the idea of emulators, may be defied by a theoretical method that he himself devised, namely Feynman diagrams. This technique organizes the calculation of a given physical quantity as a series of diagrams representing all the possible ways particles can propagate and interact (for example, ref. 9). For the many-body problem, this diagrammatic expansion is commonly used either in perturbative regimes or within uncontrolled approximations. However, the introduction of diagrammatic Monte Carlo recently allowed one to go well beyond the first few diagrams, and even reach convergence of the series in a moderately correlated regime[1,10].

In this Letter we show that for a strongly correlated system and down to a phase transition, the diagrammatic series can still be given a mathematical meaning and leads to controllable results within bold diagrammatic Monte Carlo (BDMC). This approach, proposed in refs 1–3, is first implemented here for the many-body problem. We focus on the unitary gas, that is, spin-1/2 fermions with zero-range interactions at infinite scattering length[4–6]. This system offers the unique possibility to stringently test our theory against a quantum emulator realized here with trapped ultracold ^{6}Li atoms at a broad Feshbach resonance[4–6]. This experimental validation is indispensable for our theory, based on resummation of a possibly divergent series: although the physical answer is shown to be independent of the applied resummation technique—suggesting that the procedure is adequate—its mathematical validity remains to be proven. In essence, nature provides the 'proof'. This presents the first—although long-anticipated—compelling example of how ultracold atoms can guide new microscopic theories for strongly interacting quantum matter.

At unitarity, the disappearance of an interaction-imposed length scale leads to scale invariance. This property renders the model relevant for other physical systems such as neutron matter. It also makes the balanced (that is, spin-unpolarized) unitary gas ideally suited for the experimental high-precision determination of the equation of state (EOS) described below. Finally, it implies the absence of a small parameter, making the problem notoriously difficult to solve.

In traditional Monte Carlo approaches, which simulate a finite piece of matter, the sign problem causes an exponential increase of the computing time with system size and inverse temperature. In contrast, BDMC simulates a mathematical answer in the thermodynamic limit. This radically changes the role of the fermionic sign. Diagrammatic contributions are sign-alternating with order, topology and values of internal variables. Because the number of graphs grows factorially with diagram order, a near-cancellation between these contributions is actually necessary for the series to be resummable by techniques requiring a finite radius of convergence. We find that this 'sign blessing' indeed takes place.

In essence, BDMC solves the full quantum many-body problem by stochastically summing all the skeleton diagrams for irreducible single-particle self-energy Σ and pair self-energy Π, expressed in terms of bold (that is, fully dressed) single-particle and pair propagators G and Γ which are determined self-consistently (Fig. 1). The density EOS (that is, the relation between total density n, chemical potential μ and temperature T) is given by G at zero distance and imaginary time, $n(\mu, T) = 2\,G(r = 0, \tau = 0^-)$. The thermodynamic limit can be taken analytically. The sum of ladder diagrams built on the bare single-particle propagator defines a partially dressed pair propagator Γ^0. As Γ^0 is well defined

[1]Department of Physics, University of Massachusetts, Amherst, Massachusetts 01003, USA, [2]Department of Physics and Astronomy, Ghent University, Proeftuinstraat 86, B-9000 Ghent, Belgium, [3]Laboratoire Kastler Brossel, Ecole Normale Supérieure, UPMC-Paris 6, CNRS, 24 rue Lhomond, 75005 Paris, France, [4]Theoretische Physik, ETH Zürich, CH-8093, Zürich, [5]Centre de Physique Théorique, Ecole Polytechnique, 91128 Palaiseau Cedex, France, [6]Russian Research Center "Kurchatov Institute", 123182 Moscow, Russia, [7]Department of Physics, MIT-Harvard Center for Ultracold Atoms, and Research Laboratory of Electronics, MIT, Cambridge, Massachusetts 02139, USA, [8]Advanced Light Source, Lawrence Berkeley National Laboratory, Berkeley, California 94720, USA. *e-mail: kris.vanhoucke@ugent.be.

© 2012 Macmillan Publishers Limited. All rights reserved.

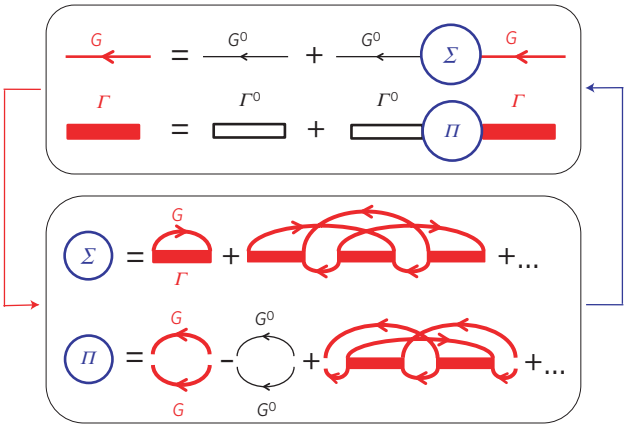

Figure 1 | Bold diagrammatic Monte Carlo The skeleton diagrammatic series for the self-energy Σ and the pair self-energy Π is evaluated stochastically (lower box). The diagrams are built on dressed one-body propagators G and pair propagators Γ, which themselves are the solution of the Dyson and Bethe-Salpeter equations (upper box). This cycle is repeated until convergence is reached. G^0 is the non-interacting propagator and Γ^0 is the partially dressed pair propagator obtained by summing the bare ladder diagrams.

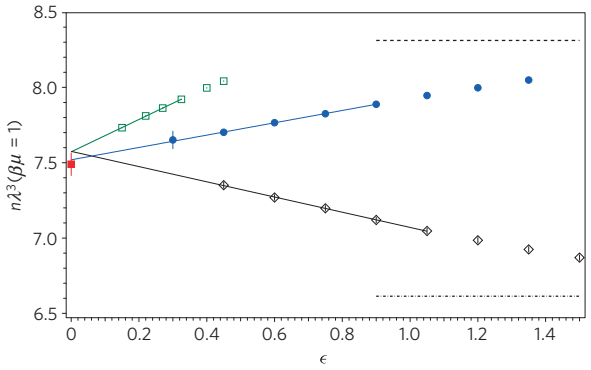

Figure 2 | Cross-validation between resummation procedure and experiment at $\beta\mu = +1$. Bold diagrammatic Monte Carlo data for the dimensionless density $n\lambda^3$, as a function of the parameter ϵ controlling the resummation procedure, for three different resummation methods: Lindelöf (blue circles), shifted Lindelöf (black diamonds), and Gauss (open green squares). The solid lines are linear fits to the Monte Carlo data, their $\epsilon \to 0$ extrapolation agrees within error bars with the experimental data point (filled red square). (In the opposite limit $\epsilon \to \infty$, the Lindelöf (resp. shifted Lindelöf) curves will asymptote to the first[15,21] (resp. third) order results, shown by the dashed (resp. dash-dotted) line.) Error bars for each ϵ represent the statistical error, together with the estimated systematic error coming from not sampling diagrams of order >9.

for the zero-range continuous-space interaction, the zero-range limit can also be taken analytically. This is in sharp contrast with other numerical methods[11–13], where taking the thermodynamic and zero-range limits is computationally very expensive. BDMC performs a random walk in the space of irreducible diagrams using local updates. The simulation is run in a self-consistent cycle (along the lines of ref. 2) until convergence is reached. Full details will be presented elsewhere. In essence, our approach upgrades the standard many-body theories based on one lowest-order diagram (for example, refs 14,15) to millions of graphs.

In the quantum degenerate regime, we do not observe convergence of the diagrammatic series for Σ and Π evaluated up to order 9. Here, order N means Σ-diagrams with N vertices (that is, N Γ-lines) and Π-diagrams with $N-1$ vertices. To extract the infinite-order result, we apply the following Abelian resummation methods[16]. The contribution of all diagrams of order N is multiplied by $e^{-\epsilon\lambda_{N-1}}$, where λ_n depends on the resummation method: (1) $\lambda_n = n\log n$ (with $\lambda_0 = 0$) for Lindelöf[16], (2) $\lambda_n = (n-1)\log(n-1)$ (with $\lambda_0 = \lambda_1 = 0$) for 'shifted Lindelöf', or (3) $\lambda_n = n^2$ for Gaussian[17]. A full simulation is performed for each ϵ, and the final result is obtained by extrapolating to $\epsilon = 0$ (Fig. 2).

This protocol relies on the following crucial mathematical assumptions: (1) the Nth order contribution of the diagrammatic expansion for Σ (for fixed external variables) is the Nth coefficient of the Taylor series at $z = 0$ of a function $g(z)$ which has a non-zero convergence radius, (2) the analytic continuation $g(1)$, performed by the above resummation methods[16,17], is the physically correct value of Σ. The same assumptions should hold for Π.

Proving these assumptions is an open mathematical challenge. Note that Dyson's collapse argument[18] is not applicable to immediately disprove the assumption (1) of a non-zero convergence radius: indeed, unlike QED, our skeleton series is not an expansion in powers of a coupling constant whose sign change would lead to an instability. The first important evidence for the validity of our mathematical assumptions is that the three different resummation methods yield consistent results. For an independent test, we turn to experiments.

The present experiment furnishes high-precision data for the density n as a function of the local value V of the trapping potential (Fig. 3 and Methods). We start the process by obtaining the EOS at high temperatures in the non-degenerate wings of the atom cloud, where the virial expansion is applicable. Once the temperature and the chemical potential have been determined from fits to the wings of the cloud, the data closer to the cloud centre provides a new prediction of the EOS. The process is iterated to access lower temperatures.

Scale invariance allows one to write the density EOS as $n(\mu,T)\lambda^3 = f(\beta\mu)$, with $\lambda = \sqrt{2\pi\hbar^2/(mk_BT)}$ the thermal de Broglie wavelength, $\beta = 1/(k_BT)$ the inverse temperature and f a universal function. A convenient normalization of the data is provided by the EOS of a non-interacting Fermi gas, $n_0\lambda^3 = f_0(\beta\mu)$. In Fig. 4a, we thus report the ratio $n(\mu,T)/n_0(\mu,T) = f(\beta\mu)/f_0(\beta\mu)$, bringing out the difference between the ideal and the strongly interacting Fermi gas. The Gibbs–Duhem relation allows us to also calculate the pressure at a given chemical potential, $P(\mu_0,T) = \int_{-\infty}^{\mu_0} d\mu\, n(\mu,T) = 1/(\beta\lambda^3)F(\beta\mu_0)$, where $F(x) = \int_{-\infty}^{x} dx' f(x')$. We normalize it by the pressure of the ideal Fermi gas and show $F(\beta\mu)/F_0(\beta\mu)$ (Fig. 4b). The agreement between BDMC and experiment is excellent. The comparison is sufficiently sensitive to validate the procedure of resumming and extrapolating (Fig. 2). The result was checked to be independent of the maximal sampled diagram order $N_{max} \in \{7;8;9\}$ within the error bars shown in Fig. 2 for each ϵ. The BDMC final error bar in Fig. 4 is the sum of the conservatively estimated systematic errors from the uncertainty of the $\epsilon \to 0$ extrapolation and from the dependence on numerical grids and cutoffs, the latter being reduced by analytically treating high-momentum short-time singular parts. The systematic error in the experiment is determined to be about 1% by the independent determination of the EOS of the non-interacting Fermi gas. The experimental error bars of Fig. 4 also include the statistical error, which is <0.5%, thanks to the scale invariance of the balanced unitary gas: irrespective of shot-to-shot fluctuations of atom number and temperature, all experimental profiles contribute to the same scaled EOS-function f. The dominant uncertainty on the experimental EOS stems from the uncertainty in the position of the ^{6}Li Feshbach resonance, known to be at 834.15 ± 1.5 G from spectroscopic measurements[19]. The change in energy, pressure and density with respect to the interaction strength is controlled by the so-called contact[20] that is obtained from Γ in the BDMC calculation.

© 2012 Macmillan Publishers Limited. All rights reserved.

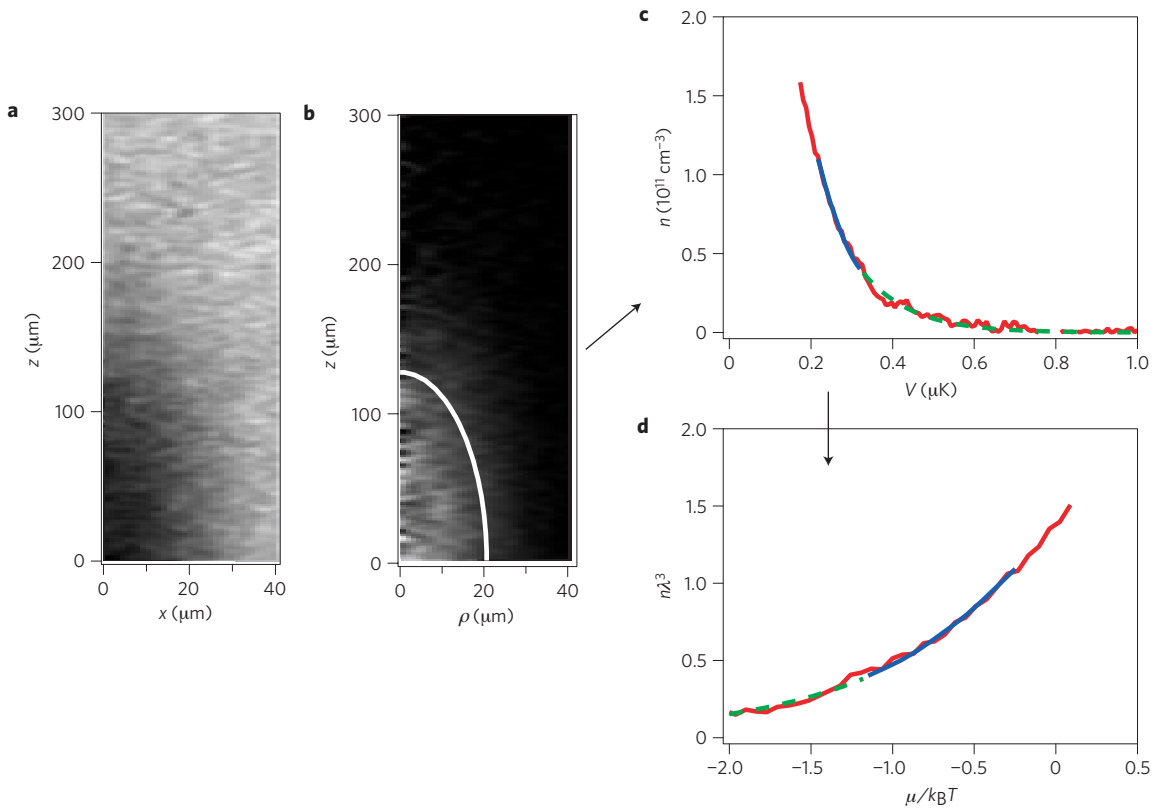

Figure 3 | Constructing the EOS from *in situ* imaging. The atom cloud shown contains $N = 8 \times 10^4$ atoms for each spin state, with a local Fermi energy of $E_F = 370$ nK at the centre. **a**, Absorption image of the atomic cloud after quadrant averaging. **b**, Reconstructed local density $n(\rho, z)$. **c**, Equipotential averaging produces a low-noise density profile, n versus V. Thermometry is performed by fitting the experimental data (red) to the known portion of the EOS (solid blue line), starting with the virial expansion for $\beta\mu < -1.25$ (green dashed line). In this example, the EOS is known for $\beta\mu \leq -0.25$, and the fit to the density profile yields $T = 113$ nK, and $\beta\mu = 1.63$. **d**, Given μ and T, the density profile can be rescaled to produce the EOS $n\lambda^3$ versus $\beta\mu$.

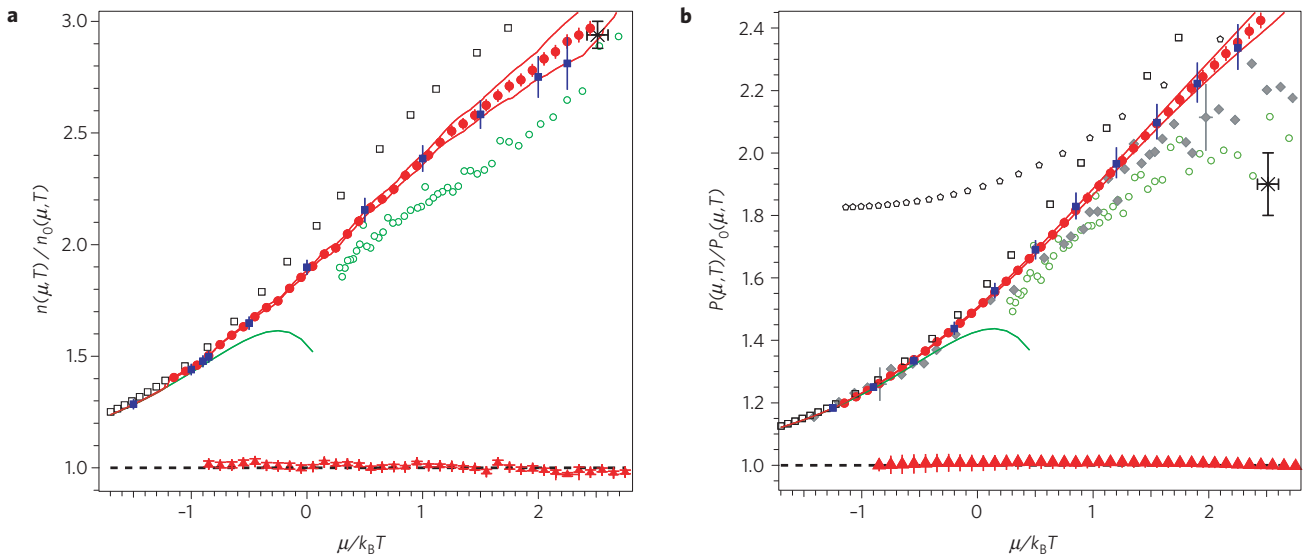

Figure 4 | Equation of state of the unitary Fermi gas in the normal phase. Density n (**a**) and pressure P (**b**) of a unitary Fermi gas, normalized by the density n_0 and the pressure P_0 of a non-interacting Fermi gas, versus the ratio of chemical potential μ to temperature T. Blue filled squares: BDMC (this work), red filled circles: experiment (this work). The BDMC error bars are estimated upper bounds on systematic errors. The error bars are one standard deviation systematic plus statistical errors, with the additional uncertainty from the Feshbach resonance position shown by the upper and lower margins as red solid lines. Black dashed line and red triangles: Theory and experiment (this work) for the ideal Fermi gas, used to assess the experimental systematic error. Green solid line: third order virial expansion. Open squares: first order bold diagram[15,21]. Green open circles: Auxiliary Field QMC (ref. 11). Star: superfluid transition point from Determinental Diagrammatic Monte Carlo[13]. Filled diamonds: experimental pressure EOS (ref. 22). Open pentagons: pressure EOS (ref. 23).

© 2012 Macmillan Publishers Limited. All rights reserved.

This allows us to define the uncertainty margins above and below the experimental data (Fig. 4) that give the prediction for the unitary EOS if the true Feshbach resonance lies 1.5 G below or above 834.15 G, respectively.

Our results clearly differ from previous theoretical and experimental results. Deviations from the theory based on the first-order Feynman diagrams[15,21] are expected, and rather remarkably moderate. Differences with lattice Monte Carlo data[11,13] may seem more surprising, as in the particular case of the balanced system these algorithms are free of the sign problem, allowing one in principle to approach the balanced unitary gas model in an unbiased way. However, eliminating systematic errors from lattice-discretization and finite volume requires extrapolations which are either not done[11] or difficult to control[12,13]. The ENS experimental pressure EOS (ref. 22) lies systematically below ours, slightly outside the reported error bar. The experimental results from Tokyo[23] do not agree with the virial expansion at high temperature. The BDMC results agree well with the present experimental data all the way down to the critical temperature for superfluidity (Fig. 4). On approaching $(\beta\mu)_c$, we observe the growth of the correlation length in the BDMC pair correlation function Γ. A protocol for extracting the critical temperature itself from the BDMC simulation will be presented elsewhere.

We are not aware of any system of strongly correlated fermions in nature where experimental and unbiased theoretical results were compared at the same level of accuracy. Even for bosons, the only analogue is liquid ^{4}He. This promotes the unitary gas to the major testing ground for unbiased theoretical treatments. The present BDMC implementation should remain applicable at finite polarization and/or finite scattering length, opening the way to rich physics which was already addressed by cold atoms experiments[6,24–27]. We also plan to extend BDMC to superfluid phases by introducing anomalous propagators. Moreover, as the method is generic, we expect numerous other important applications to long-standing problems across many fields.

Note added in proof: After a preprint of this work became available, new auxiliary-field quantum Monte Carlo data were presented[28], with undetermined systematic errors whose evaluation in future work is called for by the authors of ref. 28.

Methods

The experimental set-up has been described previously[24]. In short, ultracold fermionic ^{6}Li is brought to degeneracy by sympathetic cooling with ^{23}Na. A two-state mixture of the two lowest hyperfine states of ^{6}Li is further cooled in a hybrid magnetic and optical trap at the broad Feshbach resonance at 834 G. We employ high-resolution *in situ* absorption imaging to obtain the column density of the gas, that is converted into the full 3D density using the inverse Abel transform[29]. Equidensity lines provide equipotential lines that are precisely calibrated using the known axial, harmonic potential (axial frequency $\nu_z = 22.83 \pm 0.05$ Hz). Equipotential averaging yields low-noise profiles of density n versus potential V. Density is absolutely calibrated by imaging a highly degenerate, highly imbalanced Fermi mixture, and fitting the majority density profile to the ideal Fermi gas EOS (ref. 24). In contrast to previous studies[22,23], our analysis does not rely on the assumption of harmonic trapping.

Thermometry is performed by fitting the density profile to the EOS constructed thus far, restricting the fit to the portion of the density profile where the EOS is valid. In the high-temperature regime, the EOS is given by the virial expansion

$$n\lambda^3 = e^{\beta\mu} + 2b_2 e^{2\beta\mu} + 3b_3 e^{3\beta\mu} + \cdots \quad (1)$$

where the virial coefficients are $b_2 = 3\sqrt{2}/8$ (ref. 30), and $b_3 = -0.29095295$ (ref. 31). Fitting a high-temperature cloud to the virial expansion gives the temperature T and the chemical potential μ of the cloud, and the EOS $n\lambda^3 = f(\beta\mu)$ can be constructed. We have used equation (1) for $\beta\mu < (\beta\mu)_{max} = -1.25$ and we checked that our EOS did not change within statistical noise if we instead used $(\beta\mu)_{max} = -0.85$. Once a new patch of EOS has been produced, it can then in turn be used to fit colder clouds. Iteration of this method allows us to construct the EOS to arbitrarily low temperature. A total of ~1,000 profiles were used, with 10–100 profiles (50 on average) contributing at any given $\beta\mu$.

Received 14 October 2011; accepted 17 February 2012; published online 18 March 2012

References

1. Van Houcke, K., Kozik, E., Prokof'ev, N. & Svistunov, B. in *Computer Simulation Studies in Condensed Matter Physics XXI* (eds Landau, D. P., Lewis, S. P. & Schuttler, H. B.) (Springer, 2008).
2. Prokof'ev, N. & Svistunov, B. Bold diagrammatic Monte Carlo technique: When the sign problem is welcome. *Phys. Rev. Lett.* **99,** 250201 (2007).
3. Prokof'ev, N. V. & Svistunov, B. V. Bold diagrammatic Monte Carlo: A generic sign-problem tolerant technique for polaron models and possibly interacting many-body problems. *Phys. Rev. B* **77,** 125101 (2008).
4. Inguscio M., Ketterle, W. & Salomon, C. (eds) *Proc. Int. School of Physics Enrico Fermi*, Course CLXIV, Varenna, 20–30 June 2006 (IOS Press, 2008).
5. Giorgini, S., Pitaevskii, L. P. & Stringari, S. Theory of ultracold atomic Fermi gases. *Rev. Mod. Phys.* **80,** 1215–1274 (2008).
6. Zwerger, W. (ed.) in *BCS–BEC Crossover and the Unitary Fermi Gas* (Lecture Notes in Physics, Springer, 2012).
7. Feynman, R. Simulating physics with computers. *Int. J. Theoret. Phys.* **21,** 467–488 (1982).
8. Bloch, I., Dalibard, J. & Zwerger, W. Many-body physics with ultracold gases. *Rev. Mod. Phys.* **80,** 885–964 (2008).
9. Fetter, A. & Walecka, J. *Quantum Theory of Many-Particle Systems* (McGraw-Hill, 1971).
10. Kozik, E. *et al.* Diagrammatic Monte Carlo for correlated fermions. *Europhys. Lett.* **90,** 10004 (2010).
11. Bulgac, A., Drut, J. E. & Magierski, P. Spin 1/2 fermions in the unitary regime at finite temperature. *Phys. Rev. Lett.* **96,** 090404 (2006).
12. Burovski, E., Prokof'ev, N., Svistunov, B. & Troyer, M. Critical temperature and thermodynamics of attractive fermions at unitarity. *Phys. Rev. Lett.* **96,** 160402 (2006).
13. Goulko, O. & Wingate, M. Thermodynamics of balanced and slightly spin-imbalanced Fermi gases at unitarity. *Phys. Rev. A* **82,** 053621 (2010).
14. Strinati, G. C. in *BCS–BEC Crossover and the Unitary Fermi Gas* (ed. Zwerger, W.) (Lecture Notes in Physics, Springer, 2012).
15. Haussmann, R. Properties of a Fermi liquid at the superfluid transition in the crossover region between BCS superconductivity and Bose–Einstein condensation. *Phys. Rev. B* **49,** 12975–12983 (1994).
16. Hardy, G. *Divergent Series* (Oxford Univ. Press, 1949).
17. Fruchard, A. Prolongement analytique et systèmes dynamiques discrets. *Collect. Math.* **43,** 71–82 (1992).
18. Dyson, F. J. Divergence of perturbation theory in quantum electrodynamics. *Phys. Rev.* **85,** 631–632 (1952).
19. Bartenstein, M. *et al.* Precise determination of ^{6}Li cold collision parameters by radio-frequency spectroscopy on weakly bound molecules. *Phys. Rev. Lett.* **94,** 103201 (2004).
20. Braaten, E. in *BCS–BEC Crossover and the Unitary Fermi Gas* (ed. Zwerger, W.) (Lecture Notes in Physics, Springer, 2012).
21. Haussmann, R., Rantner, W., Cerrito, S. & Zwerger, W. Thermodynamics of the BCS–BEC crossover. *Phys. Rev. A* **75,** 023610 (2007).
22. Nascimbène, S., Navon, N., Jiang, K. J., Chevy, F. & Salomon, C. Exploring the thermodynamics of a universal Fermi gas. *Nature* **463,** 1057–1060 (2010).
23. Horikoshi, M., Nakajima, S., Ueda, M. & Mukaiyama, T. Measurement of universal thermodynamic functions for a unitary Fermi gas. *Science* **327,** 442–445 (2010).
24. Ketterle, W. & Zwierlein, M. Making, probing and understanding ultracold Fermi gases. *Rivista del Nuovo Cimento* **31,** 247–422 (2008).
25. Shin, Y., Schunck, C., Schirotzek, A. & Ketterle, W. Phase diagram of a two-component Fermi gas with resonant interactions. *Nature* **451,** 689–693 (2007).
26. Shin, Y. Determination of the equation of state of a polarized Fermi gas at unitarity. *Phys. Rev. A* **77,** 041603(R) (2008).
27. Navon, N., Nascimbène, S., Chevy, F. & Salomon, C. The equation of state of a low-temperature Fermi gas with tunable interactions. *Science* **328,** 729–732 (2010).
28. Drut, J. E., Lähde, T. A., Wlazłowski, G. & Magierski, P. The equation of state of the unitary Fermi gas: An update on lattice calculations. Preprint at http://arxiv.org/abs/1111.5079v1 (2011).
29. Shin, Y., Zwierlein, M., Schunck, C., Schirotzek, A. & Ketterle, W. Observation of phase separation in a strongly interacting imbalanced Fermi gas. *Phys. Rev. Lett.* **97,** 030401 (2006).
30. Ho, T-L. & Mueller, E. J. High temperature expansion applied to fermions near Feshbach resonance. *Phys. Rev. Lett.* **92,** 160404 (2004).
31. Liu, X-J., Hu, H. & Drummond, P. D. Virial expansion for a strongly correlated Fermi gas. *Phys. Rev. Lett.* **102,** 160401 (2009).

© 2012 Macmillan Publishers Limited. All rights reserved.

Acknowledgements

We thank R. Haussmann for providing propagator data from refs 15,21 for comparison, and the authors of refs 11,13,22,23 for sending us their data. This collaboration was supported by a grant from the Army Research Office with funding from the Defense Advanced Research Projects Agency (DARPA) Optical Lattice Emulator program. Theorists acknowledge the financial support of the Research Foundation Flanders (FWO) (K.V.H.), National Science Foundation (NSF) grant PHY-1005543 (University of Massachusetts group), Swiss National Science Foundation (SNF) Fellowship for Advanced Researchers (E.K.), and l'Institut Francilien de Recherche sur les Atomes Froids (IFRAF) (F.W.). Simulations ran on the clusters CM at UMass and Brutus at ETH. The MIT work was supported by the NSF, AFOSR-MURI, ARO-MURI, Office of Naval Research (ONR), DARPA Young Faculty Award, an AFOSR Presidential Early Career Award for Scientists and Engineers (PECASE), the David and Lucile Packard Foundation, and the Alfred P. Sloan Foundation.

Author contributions

K.V.H. (theory) and M.J.H.K. (experiment) contributed equally to this work. K.V.H., F.W., E.K., N.P. and B.S. developed the BDMC approach for unitary fermions; the computer code was written by K.V.H. assisted by F.W.; simulation data were produced by F.W., E.K. and K.V.H.; M.J.H.K., A.T.S., L.W.C., A.S. and M.W.Z. all contributed to the experimental work and the analysis. All authors participated in the manuscript preparation.

Additional information

The authors declare no competing financial interests. Reprints and permissions information is available online at www.nature.com/reprints. Correspondence and requests for materials should be addressed to K.V.H.

© 2012 Macmillan Publishers Limited. All rights reserved.